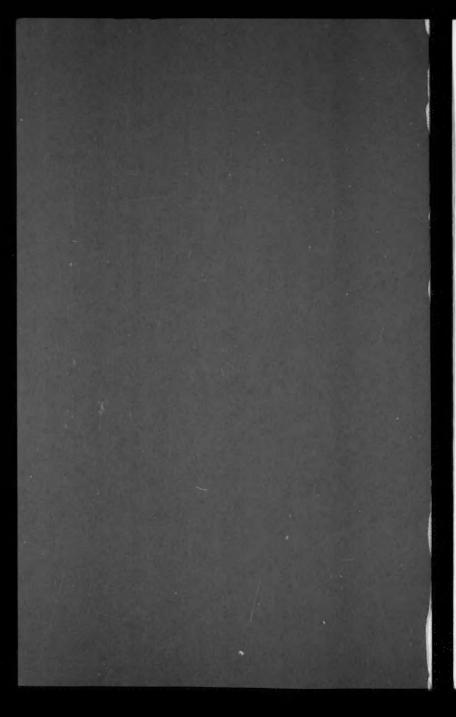
VOL.107 NO.HY5. MAY 1981

JOURNAL OF THE HYDRAULICS DIVISION

PROCEEDINGS OF THE AMERICAN SOCIETY OF CIVIL ENGINEERS





VOL.107 NO.HY5. MAY 1981

JOURNAL OF THE HYDRAULICS DIVISION

PROCEEDINGS OF THE AMERICAN SOCIETY OF CIVIL ENGINEERS



Copyright© 1981 by American Society of Civil Engineers All Rights Reserved ISSN 0044-796X

AMERICAN SOCIETY OF CIVIL ENGINEERS

BOARD OF DIRECTION

President Irvan F. Mendenhall

Past President Joseph S. Ward

President Elect James R. Sims Vice Presidents

Robert D. Bay Francis J. Connell

Directors
Martin G. Abegg
Floyd A. Bishop
L. Gary Byrd
Larry J. Feeser
John A. Focht, Jr.
Sergio Gonzalez-Karg
James E. Humphrey, Jr.
Richard W. Karn
Leon D. Luck
Arthur R. McDaniel

Lyman R. Gillis Albert A. Grant

egg Paul R. Munger
William R. Neuman
Leonard S. Oberman
er
It, Jr.
Islez-Karg
mphrey, Jr.
S. Russell Stearns
William H. Taylor
Stafford E. Thornton
Robert E. Whiteside
Richard S. Woodruff

EXECUTIVE OFFICERS

Eugene Zwoyer, Executive Director Julie E. Gibouleau, Assistant to the Executive Director Louis L. Meier, Washington Counsel/Assistant

Secretary
William H. Wisely, Executive Director Emeritus
Michael N. Salgo, Treasurer
Elmer B. Isaak, Assistant Treasurer

STAFF DIRECTORS

Donald A. Buzzell, Managing Director for Education and Professional Affairs Robert A. Crist, Jr., Managing Director for Publications and Technical Affairs Alexander Korwek, Managing Director for Finance and Administrative Services Alexandra Ballow, Director, Human Resources David Dresia, Director, Publications Production and Marketing Barker D. Herr, Director, Membership Richard A. Jeffers, Controller Carl E. Nelson, Director, Field Services Don P. Reynolds, Director, Policy, Planning and Public Affairs Bruce Rickerson, Director, Legislative Services James M. Shea, Director, Public

Communications
Albert W. Turchick, Director, Technical
Services

George K. Wadlin, Director, Education Services

R. Lawrence Whipple, Director, Engineering Management Services

COMMITTEE ON PUBLICATIONS

Stafford E. Thornton, *Chairman*Martin G. Abegg Richard W. Karn
John A. Focht, Jr. Paul R. Munger
William R. Neuman

HYDRAULICS DIVISION

Executive Committee
Ronald E. Nece, Chairman
Rudolph P. Savage, Vice Chairman
George E. Hecker
Charles S. Mifkovic, Secretary
John J. Cassidy, Management Group D Contact
Member

Publications Committee
Melvin W. Anderson, Chairman
John A. Hoopes, Vice Chairman
Philip H. Burgi, Hydraulic Structures
Richard H. (Pete) Hawkins, Surface Water
Hydrology

John A. Hoopes, Hydromechanics, General Gerhard H. Jirka, Hydraulic Transport and Dispersion

Chintu Lai, Hydromechanics, Open Channels Frederick A. Locher, Hydromechanics, Open Channels Donn G. DeCoursey, Sedimentation

Donn G. DeCoursey, Sedimentation Bryan R. Pearce, Tidal Hydraulics John A. Roberson, Hydromechanics, Closed Conduits

John L. Wilson, Groundwater Hydrology George E. Hecker, Exec. Comm. Contact Member

PUBLICATION SERVICES DEPARTMENT

David Dresia, Director, Publications Production and Marketing

Technical and Professional Publications

Richard R. Torrens, Manager Linda Ellington, Copy Editor Thea C. Feldman, Copy Editor Meryl Mandle, Copy Editor Joshua R. Spieler, Copy Editor Shiela Menaker, Production Co-ordinator Richard C. Scheblein, Draftsman

Information Services

Elan Garonzik, Editor

PERMISSION TO PHOTOCOPY JOURNAL PAPERS

Permission to photocopy for personal or internal reference beyond the limits in Sections 107 and 108 of the U.S. Copyright Law is granted by the American Society of Civil Engineers for libraries and other users registered with the Copyright Clearance Center, 21 Congress Street, Salem, Mass. 01970, provided the appropriate fee is paid to the CCC for all articles bearing the CCC code. Requests for special permission or bulk copying should be addressed to the Manager of Technical and Professional Publications, American Society of Civil Engineers.

CONTENTS

Design Curves for Hinged Wavemakers: Theory by Robert T. Hudspeth and Min-Chu Chen							533
Design Curves for Hinged Wavemakers: Experiments by Robert T. Hudspeth, John W. Leonard, and Min-Chu Chen							553
Numerical Analysis of Flow in Sedimentation Basins by David R. Schamber and Bruce E. Larock							575
Uncertainties Resulting from Changes in River Form by Durl E. Burkham							593
Maximum Clear-Water Scour around Circular Piers by Subhash C. Jain							611

This Journal is published monthly by the American Society of Civil Engineers. Publications office is at 345 East 47th Street, New York, N.Y. 10017. Address all ASCE correspondence to the Editorial and General Offices at 345 East 47th Street, New York, N.Y. 10017. Allow six weeks for change of address to become effective. Subscription price to members is \$16.50. Nonmember subscriptions available; prices obtainable on request. Second-class postage paid at New York, N.Y. and at additional mailing offices. HY.

The Society is not responsible for any statement made or opinion expressed in its publications.

TECHNICAL NOTES

Proc. Paper 16222

Biofilm Growth and Hydraulic Performance by Brian Butterworth	629
Wind-Induced Mixing in Stratified Fluid	
by C. Kranenburg	631
DISCUSSION	
Proc. Paper 16217	
Secondary Flow and Shear Stress at River Bends, by James C. Bathurst, Colin R. Thorne, and Richard D. Hey (Oct., 1979. Prior Discussion: Oct., 1980).	
closure	641
Uncertainty in Step-Backwater Profiles, by Asok Motayed and David R. Dawdy (May, 1979. Prior Discussion: Apr., 1980).	642
Open Channel Flow with Varying Bed Roughness, by Donald W.	
Knight and J. Alasdair Macdonald (Sept., 1979. Prior Discussions: Sept., Oct., 1980).	
closure	644
Inception of Sediment Transport, by M. Selim Yalin and Emin Karahan (Nov., 1979. Prior Discussions: Aug., Oct., 1980).	
closure	647
Staged Multiport Diffusers, by Charles W. Almquist and Keith D. Stolzenbach (Feb., 1980. Prior Discussion: Oct., 1980).	
closure	648
Time-Dependent Stochastic Model of Floods, by Michel North (May, 1980).	
errata	650
Log Pearson Type 3 Distribution: Method of Mixed Moments, by Donthamsetti Veerabhadra Rao (June, 1980).	
errata	650

Empirical Investigation of Curve Number Technique," by Allen T.	
Hjelmfelt, Jr. (Sept., 1980).	
by Michael Daly	551
by Kenneth G. Renard	551
Calibration of Bed-Load Samplers, by Peter Engel and Y. Lam Lau (Oct., 1980).	
by Glendon T. Stevens, Jr	554
Sedimentation in Iron Gates Reservoir on the Danube, by Vlad Focsa (Oct., 1980).	
by Nani G. Bhowmik	556

INFORMATION RETRIEVAL

The key words, abstract, and reference "cards" for each article in this Journal represent part of the ASCE participation in the EJC information retrieval plan. The retrieval data are placed herein so that each can be cut out, placed on a 3×5 card and given an accession number for the user's file. The accession number is then entered on key word cards so that the user can subsequently match key words to choose the articles he wishes. Details of this program were given in an August, 1962 article in CIVIL ENGINEERING, reprints of which are available on request to ASCE headquarters.

^aDiscussion period closed for this paper. Any other discussion received during this discussion period will be published in subsequent Journals.

16236 DESIGN CURVES FOR HINGED WAVEMAKERS: THEORY

KEY WORDS: Curves (geometry); Numerical analysis; Ocean engineering; Ocean waves; Theoretical analysis; Theory; Wave measurement; Wave propagation; Wave tanks

ABSTRACT: Dimensionless theoretical design curves for hinged wavemakers of variable draft are extended, within the limits of linearized potential wave theory, to wave flume geometries consisting of two constant depth domains separated by a gradually sloping transition region. These design curves are examined for the following: hydrodynamic pressure moment, moment arm, relative moment phase angle, and the ratio of the wavemaker stroke to the propagating wave height. The dimensionless design curves are shown to demonstrate the effects of wave flume and wavemaker geometry on the minimum inertial wave pressure moment on the wavemaker flap better than tabular lookup methods. The effects of nondimensional wavemaker parameters on the dimensionless wavemaker power curves are explored, and they are compared to the energy flux in a propagating periodic wave. Convergence of the eigenfunction expansion for the wavemaker velocity for hinged wavemakers of variable depth is examined numerically.

REFERENCE: Hudspeth, Robert T., and Chen, Min-Chu, "Design Curves for Hinged Wavemakers: Theory," *Journal of the Hydraulics Division*, ASCE, Vol. 107, No. HY5, Proc. Paper 16236, May, 1981, pp. 533-552

16237 DESIGN CURVES & HINGED WAVEMAKERS: EXPERIMENTS

KEY WORDS: Curves (geometry); Experimental data; Numerical analysis; Ocean engineering; Ocean waves; Theoretical analysis; Time factors; Water depth; Wave propagation; Wave tanks

ABSTRACT: Experimental data measured in large-scale wave flume (for the dimensionless wavemaker gain function and for the magnitude and phase angle for the dimensionless wavemaker hydrodynamic pressure moment on a hinged wavemaker) are compared with theoretical values computed from dimensionless design curves which are derived from linear wave theory. Dimensionless relative errors between experimental and theoretical values are tabulated for 21 discrete wave frequencies in each of two water depths. These dimensionless relative errors provide comparisons for over one decade of dimensionless relative water depth which cover both intermediate- and deep-water wave conditions for wave heights which are approx. 25% of the theoretical breaking limit. While measured data from smaller scale wave flumes have been previously published for the dimensionless wavemaker gain function, S/H, the measured hydrodynamic pressure moment data appear to be unique.

REFERENCE: Hudspeth, Robert T., Leonard, John W., and Chen, Min-Chu, "Design Curves for Hinged Wavemakers: Experiments," *Journal of the Hydraulics Division*, ASCE, Vol. 107, No. HY5, **Proc. Paper 16237**, May, 1981, pp. 553-574

16227 ANALYSIS OF FLOW IN SEDIMENTATION BASINS

KEY WORDS: Basins (containers); Continuity equation; Finite element method; Flow measurement; Flow profiles; Mathematical models; Momentum equation; Numerical analysis; Particle distribution; Sedimentation; Sedimentation rates; Sedimentation tanks; Turbulent flow; Velocity field

ABSTRACT: The equations governing two-dimensional, steady flow in circular and rectangular primary settling basins are formulated. Mean-flow equations expressing conservation of mass and momentum are combined with a two-equation turbulence model (k-\(\phi\) model) to compute velocity fields in sedimentation basins. The turbulence is characterized by a turbulent kinematic eddy viscosity which is computed directly as part of the solution. A numerical solution to the mathematical model is formulated by application of the Galerkin finite element method to the equation residuals. The resulting non-linear system of equations is solved by a variation of Newton's method. The model is applied to predict the flow pattern in a rectangular settling basin. A vector plot of the basin velocity field and contour plot of the turbulent kinematic eddy viscosity are presented.

REFERENCE: Schamber, David R., and Larock, Bruce E., "Numerical Analysis of Flow in Sedimentation Basins," *Journal of the Hydraulics Division*, ASCE, Vol. 107, No. HY5, Proc. Paper 16227, May, 1981, pp. 575-591

16245 RESULTS FROM CHANGES IN RIVER FORM

KEY WORDS: Channel erosion; Drainage basins; Erosion; Flood hydrology; Flood plains; Floods; Land use; River flow; Rivers; Sedimentation

ABSTRACT: Uncertainties resulting from flood-induced major changes in river form in some drainage basins are of such magnitude that many problems pertaining to the management of water and debris, the management of flood plains, and the effects of man's activities in the basins cannot be resolved except in a probabilistic or general way. For affected basins, major changes in channel form can cause significant differences in the hydraulics of floods, the surface runoff, recharge to aquifers, erosion rates, and sediment yields. Uncertainties develop for several related reasons. The capability does not exist to determine adequately whether a river is susceptible to a major change in form and to predict when a major river-form change will occur. The effects of a local change in river form in a drainage basin usually propagates along alluvium-filled valleys to other parts of the basin, but the propagation process is not understood.

REFERENCE: Burkham, Durl E., "Uncertainties Resulting from Changes in River Form," Journal of the Hydraulics Division, ASCE, Vol. 107, No. HY5, Proc. Paper 16245, May, 1981, pp. 593-610

16260 CLEAR-WATER SCOUR AND CIRCULAR PIERS

KEY WORDS: Bridges (piers); Flow profiles; Formulas; Piers (supports); Scour; Scouring; Sediment analysis; Streambeds

ABSTRACT: The potential predictors of the maximum clear-water scour are compared with the available experimental data. The range of flow parameters, for which these formulas either overpredicted or underpredicted, are delineated. Comparison indicates that the scour formula by Laurson and Toch is the best predictor among those examined, for it encompasses all data and overpredicts less than the other formulas. However, the Laursen and Toch formula predicts that the scour depth is independent of sediment size. A new formula for the maximum clear-water scour is proposed; it is very similar to that of Laursen and Touch but includes the effect of sediment size on scour depth.

REFERENCE: Jain, Subhash C., "Maximum Clear-Water Scour Around Circular Piers," Journal of the Hydraulics Division, ASCE, Vol. 107, No. HY5, Proc. Paper 16260, May, 1981, pp. 611-626

DESIGN CURVES FOR HINGED WAVEMAKERS: THEORY

By Robert T. Hudspeth, M. ASCE and Min-Chu Chen²

INTRODUCTION

The basic wavemaker theory for forced harmonic surface gravity waves derived by Havelock (5) has been elaborately extended to design curves by Gilbert, et. al (3) for both periodic and random waves for three types of wavemaker geometries which are commonly encountered in many modern wave flumes. Limited experimental verifications of these design curves were covered by Krishnamacker (10) and by Gilbert, et. al (4). Hyun (7) later extended the basic theoretical solution for the case of periodic waves only which are generated by a hinged-type of wavemaker with a hinge of variable draft. Hyun concluded from his theoretical results in the case of deep water waves that the inertial component of the hydrodynamic wave pressure force on the wavemaker dominates the total pressure force if the hinged wavemaker flap extends over the entire fluid depth. Hyun did not present experimental verification of this theoretical result; but his conclusion clearly agrees with the design curves previously presented by Gilbert, et. al (Ref. 3, Fig. 2, p. 165) for the values of h/gT^2 greater than 0.2. Experimental verifications of these wavemaker solutions for various types of wavemaker geometries have been restricted primarily to the analytical relationships for the wavemaker gain function which relates wave height, H, to the wavemaker stroke, S, which is measured at a particular vertical elevation above the bottom [compare to Biesel and Suguet (1) and Ursell, et. al (13) for the case of monochromatic linear waves forced by both piston and hinged-types of wavemakers; and Madsen (11) and Multer (12) for the nonlinear, initial value wavemaker problem formulated by Kennard (8)]. Experimental verifications of the theoretical forces, moments, and power requirements for wavemakers of any type appear to be relatively scarce.

The solution presented by Hyun (7) for a hinged-type wavemaker of variable 'Assoc. Prof., Dept. of Civ. Engrg. and Ocean Engrg. Programs, Oregon State Univ.,

Corvallis, Oreg. 97331.

²Sr. Research Engr., Offshore System Div., Exxon Production Research Co., Houston, Tex. 77001; formerly, Grad. Research Asst., Dept. of Civ. Engrg., Oregon State Univ.,

Corvallis, Oreg. 97331.

Note.—Discussion open until October 1, 1981. Separate discussions should be submitted for the individual papers in this symposium. To extend the closing date one month, a written request must be filed with the Manager of Technical and Professional Publications, ASCE. Manuscript was submitted for review for possible publication on March 11, 1980. This paper is part of the Journal of the Hydraulics Division, Proceedings of the American Society of Civil Engineers, ©ASCE, Vol. 107, No. HY5, May, 1981. ISSN 0044-796X/81/0005-0533/\$01.00.

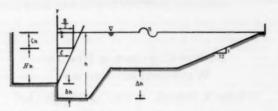


FIG. 1.—Definition Sketch for Wave Flume Geometry

draft is extended in a minor way within the limits of linearized potential wave theory to wave flumes which consist of two constant depth regions separated by a gradually sloping transition region (Fig. 1). Design curves for the wavemaker gain function, S/H, the dimensionless hydrodynamic pressure moment, M', moment arm, I/H, and wavemaker power, W', for this type of wave flume geometry are developed which follow the more desirable format presented by Gilbert, et. al (3). Experimental verifications of these design curve values were measured in a large-scale wave flume at the Oregon State University Wave Research Facility (OSU-WRF) and are presented in the companion paper (6).

WAVEMAKER THEORY

For convenience in developing universal design curves, all variables will be made dimensionless at the outset by the usual physical variables; viz., a length scale = g/ω^2 ; a time scale = ω^{-1} , and a mass density scale = ρ , in which g = gravitational constant; ω = radian frequency; and ρ = mass density of fluid in the wave flume. The relationships between physical variables (denoted by *) and dimensionless variables are given by the following:

$$p = (p^*) \frac{\omega^2}{\rho g^2}; \quad \mathbf{F} = (\mathbf{F}^*) \frac{\omega^6}{\rho g^4}; \quad \mathbf{M} = (\mathbf{M}^*) \frac{\omega^8}{\rho g^5}; \quad \langle \dot{W} \rangle = \langle (\dot{W}^*) \rangle \frac{\omega^7}{\rho g^5} \quad (1e)$$

The two-dimensional, irrotational motion of an incompressible, inviscid fluid in the wave flume geometry shown in Fig. 1 for a right-handed Cartesian coordinate system may be obtained from the directional derivatives of a dimensionless scalar velocity potential, $\Phi(x, y, t)$, according to

$$u(x,y,t) = -\Phi_x \quad ... \quad ...$$

$$v(x,y,t) = -\Phi_{y} \quad \dots \quad \dots \quad \dots \quad \dots \quad \dots \quad (2b)$$

in which the subscripts denote partial differentiation with respect to the independent spatial variables denoted by the subscript. The total pressure may be determined from the linearized Bernoulli equation given by

For simple harmonic wavemaker motions which are strictly periodic in period $T = 2\pi$, a dimensionless *spatial* velocity potential, $\phi(x, y)$, may be defined by the real part of

which must be a solution to the dimensionless equation of continuity given by

$$\phi_{xx} + \phi_{yy} = 0; \quad 0 \le x < +\infty, \quad -h \le y \le 0 \quad ... \quad ..$$

Considering first the constant depth region immediately adjacent to the wavemaker in Fig. 1, the linearized homogeneous boundary conditions for the constant horizontal boundaries are given by

$$\phi_y - \phi = 0; \quad y = 0, x > 0 \dots (6a)$$

$$\phi_y = 0; \quad y = -h, x > 0 \quad \dots \quad \dots \quad \dots \quad \dots \quad \dots \quad (6b)$$

Eqs. 5 and 6 form a well-posed Sturm-Liouville problem for ϕ by the method of separation of variables. The multiplicative coefficients in the solution for this type of eigenvalue problem must be quantified by an inhomogeneous boundary condition which is given by the prescribed motion of the wavemaker. Expressing the wavemaker surface by the following Stokes' material coordinate:

the inhomogeneous boundary condition for the fluid motion may be obtained from the Stokes' material derivative of Eq. 7 according to

Expanding Eq. 8 in a Maclaurin series about x = 0 and retaining only the linear terms yields the following linearized inhomogeneous boundary condition for small oscillations of the wavemaker:

$$\phi_x = -\chi_t, x = 0; -h \le y \le 0 \dots (9)$$

A radiation condition that requires only outgoing, right-progressing waves in Fig. 1 completes the linearized boundary value problem. If the reflections from both the gradually sloping transition region between the two constant depth domains and from the sloping terminal beach are neglected, the conservation of energy flux [compare to Eagleson and Dean (2)] may be used to compute the fluid motion in the second constant depth domain of depth, $h(1 - \Delta)$.

Specifically, the simple harmonic displacement of the hinged wavemaker in Fig. 1 may be given by the real part of

in which α = an arbitrary initial phase angle; and

$$\xi(y) = \frac{S}{2H} \left(1 - \delta + \frac{y}{h} \right); \quad h(\delta - 1) \le y \le 0 \quad$$
 (11a)

The arbitrary initial phase angle, α , has been introduced in anticipation of data analyses by a finite Fourier transform (FFT) algorithm in order to more efficiently determine the phase and magnitude of the measured simple harmonic physical variables. Restricting the phase angle, α , to integer multiples of $n\pi/2$ radians as in the problem formulations in other references is too restrictive and unnecessarily complicates data analyses by FFT methods.

The well-known (1) velocity potential solution to Eq. 5 which satisfies Eq. 6 is given by the real part of

in which the unknown multiplicative coefficients A_n are either pure real or pure imaginary. The orthonormal eigenfunctions $f_n(y)$ are given by the following set [Kreisel (9)]:

$$f_n(y) = \frac{\cos K_n(y+h)}{N_n}; \quad n = 1, 2, \dots$$
 (14)

in which the normalizing constants, N_n , are determined from

$$N_n^2 = \int_{-h}^0 \cos^2 K_n(y+h) \, dy = \frac{2 K_n h + \sin 2 K_n h}{4 K_n}; \quad n = 1, 2, \dots \dots (15)$$

provided that the eigenvalues $K_n h$ are computed from

$$h = -K_n h \tan K_n h; \quad n = 1, 2, ...$$
 (16a)

$$(2n-3)\frac{\pi}{2} < K_n h < (n-1)\pi; \quad n \ge 2 \quad ... \quad (16c)$$

The orthogonality of the orthonormal eigenfunctions f_n in the interval of orthogonality $-h \le y \le 0$ allows the multiplicative unknown coefficients A_n to be computed in a best least-square sense from the following integral:

$$A_{n} = \frac{i}{K_{n}} \int_{-h}^{0} \xi(y) f_{n}(y) dy; \quad n \ge 1 \quad ... \quad (17)$$

which yields for the geometry given in Fig. 1

$$A_{n} = \frac{S}{K_{n}hH} \frac{[K_{n}h(1-\delta)\sin K_{n}h + \cos K_{n}h - \cos K_{n}h\delta]}{(K_{n})^{3/2}(2K_{n}h + \sin 2K_{n}h)^{1/2}} \exp\left(i\frac{\pi}{2}\right);$$

$$n \ge 1.$$
 (18)

Again, the phase shift $\pi/2$ has been introduced in order to reference the velocity potential to the displacement of the wavemaker in anticipation of data analyses by an FFT algorithm which is referenced to the displacement of the wavemaker instead of to the velocity of the wavemaker as prescribed by the boundary value problem in Eq. 9.

The simple harmonic linear free surface profile, $\eta(x,t)$, of amplitude H/2, may be determined from the linearized Bernoulli equation given by Eq. 3 within the first constant depth region, h, immediately adjacent to, but sufficiently far away from, the wavemaker in order for the evanescent modes (i.e., $n \ge 2$) to have decayed to less than 1% of their values at the wavemaker, (x > 3h, say); i.e.:

$$\eta = i\Phi; \quad y = 0 \quad ... \quad (19)$$

Substitution of Eq. 18 into Eq. 20 may be shown to reduce to the gain function ratio H/S, obtained by Hyun (Ref. 7, Eq. 15, p. 3) for the special case that the stroke of the hinged wavemaker, S, is measured at $\zeta=0$, as well as to the ratio obtained by Ursell, et. al (Ref. 13, Eq. 3.10, p. 37) for the special case that $\delta=\zeta=0$. However, many wave flume experiments are designed to be conducted in the second domain of constant depth $h(1-\Delta)$ in Fig. 1. Invoking the conservation of energy flux from linear wave theory (2) yields for the wavemaker gain function

$$\frac{S}{H} = \frac{KhH}{4\sinh Kh} \left[\frac{K}{\kappa} \right]^{1/2} \left[\frac{1 + \frac{2\kappa h(1 - \Delta)}{\sinh 2\kappa h(1 - \Delta)}}{1 + \frac{2Kh}{\sinh 2Kh}} \right]^{1/2}$$

$$\left[\frac{2Kh + \sinh 2Kh}{Kh(1 - S)\sinh Kh - \cosh Kh - \cosh KhS} \right]$$
(21)

 $Kh(1-\delta)\sinh Kh - \cosh Kh + \cosh Kh\delta$ in which the propagating wave number, κ , in the constant depth region $h(1-\delta)$

 $-\Delta$) is determined from

Fig. 2 demonstrates this design wavemaker gain function for various wave flume geometries; and demonstrates that the effect of reducing the wavemaker draft (i.e., increasing δ) results in increasing the magnitude of the wavemaker gain function. This increase is less for the deep water case and supports a similar conclusion reached by Hyun (7).

The moment about the wavemaker hinge which is induced on the wavemaker of width B shown in Fig. 1 by the fluid side of the wave flume only is simply obtained from the hydrodynamic pressure moment computed from the linearized Bernoulli equation. For a positive moment vector defined by $\mathbf{M} = \mathbf{r} \times \mathbf{F}$, the component of torque induced on the wavemaker by the fluid will yield a positive moment defined by the real part of

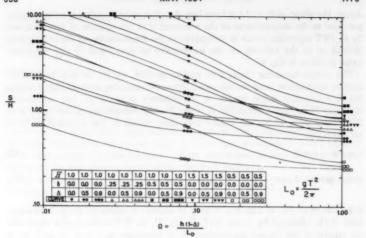


FIG. 2.—Dimensionless Wavemaker Gain Function, \mathbf{S}/H , as Function of Wave Flume Geometry

$$M = i B \exp i(t + \alpha) \int_{h(\delta - 1)}^{0} [y + h(1 - \delta)] \phi(0, y) dy \qquad (23a)$$

$$M = -M_p \sin(t + \alpha) - M_e \cos(t + \alpha) \qquad (23b)$$

$$M = |M| \cos(t + \alpha_M) \quad ... \quad (23c)$$

in which $\alpha_M = measured$ phase angle for the moment. The amplitude of the moment due to the propagating mode is given by

$$M_{p} = \frac{HB}{2 K^{3} \sinh Kh} \left[\frac{K}{\kappa} \right]^{1/2} \left[\frac{1 + \frac{2 \kappa h (1 - \Delta)}{\sinh 2 \kappa h (1 - \Delta)}}{1 + \frac{2 Kh}{\sinh 2 Kh}} \right]^{1/2}$$

$$[Kh(1-\delta)\sinh Kh - \cosh Kh + \cosh Kh\delta] \dots \dots \dots \dots \dots \dots (24a)$$

and the amplitude of the moment due to the evanescent modes is given by

$$M_{e} = \frac{HBK}{2 \sinh Kh} \left[\frac{K}{\kappa} \right]^{1/2} \left[\frac{1 + \frac{2\kappa h(1 - \Delta)}{\sinh 2\kappa h(1 - \Delta)}}{1 + \frac{2Kh}{\sinh 2Kh}} \right]^{1/2}$$

$$\left\{ (2Kh + \sinh 2Kh) \right\}$$

$$\left\{\frac{(2Kh + \sinh 2Kh)}{[Kh(1-\delta)\sinh Kh - \cosh Kh + \cosh Kh\delta]}\right\}$$

$$\sum_{n=2}^{\infty} \frac{\left[K_n h (1-\delta) \sin K_n h + \cos K_n h - \cos K_n h \delta\right]^2}{K_n^4 (2K_n h + \sin 2K_n h)} \dots \dots \dots (24b)$$

Eqs. 24a and 24b may be shown to reduce to Eqs. 20b and 20c, respectively, given by Hyun (Ref. 7, p. 4) for the special case that the wave flume has a constant depth, that the wavemaker stroke is measured at the still water level, and finally, that fluid exists on only one side of the wavemaker.

The relationships between the magnitude of the measured hydrodynamic pressure moment, |M|, and the magnitudes of the theoretical components of the hydrodynamic pressure moment on the wavemaker are easily shown to be the following (compare Appendix I):

$$M_e = -|M|\cos(\alpha_M - \alpha)$$
 (25b)

The theoretical relative moment phase angle, β_M , between the hydrodynamic moment and the displacement of the wavemaker is given by

$$\beta_{M} = \arctan\left(-\frac{M_{p}}{M_{e}}\right) \quad . \tag{25c}$$

which may be computed from the measured FFT coefficients which are referenced to the arbitrary initial displacement of the wavemaker by subtracting the two measured phase angles from each measured signal according to (compare to Appendix I)

$$\beta_M = \alpha_M - \alpha \quad \quad (25d)$$

The components of the rotational velocity of the wavemaker about the hinged bottom may be determined from

$$(\mathbf{r} \times \mathbf{q}) \cdot \mathbf{e}_z = -y (u_p + u_e) \quad ... \quad ...$$

By substituting for the components of the horizontal velocity from Eqs. 2a, 13, and 18 and by equating real parts, it may be shown that the propagating component of the wavemaker moment, $-M_p$ sin $(t + \alpha)$ given by Eq. 23b is in-phase with the wavemaker angular velocity; while the evanescent component of the wavemaker moment, $-M_e$ cos $(t + \alpha)$, is in-phase with the wavemaker angular acceleration.

Similarly, the total hydrodynamic pressure force in the x direction which is induced on the wavemaker by the fluid side only of the wave flume may be computed by again integrating over the wetted area of the wavemaker the dynamic component of the linearized Bernoulli equation; i.e., from the real part of

$$F = -i B \exp i(t + \alpha) \int_{h(\delta - 1)}^{0} \phi(o, y) dy \qquad (26a)$$

$$F = |F| \cos(t + \alpha_F) \quad ... \quad (26c)$$

in which the α_F = measured phase angle for the pressure force. The amplitude of the dynamic pressure force due to the propagating mode is given by

I

$$F_{\rho} = \frac{HB}{2K^2 \sinh Kh} \left[\frac{K}{\kappa} \right]^{1/2} \left[1 + \frac{2\kappa h(1-\Delta)}{\sinh 2\kappa h(1-\Delta)} \right]^{1/2} (\sinh Kh - \sinh Kh\delta)$$

$$1 + \frac{2Kh}{\sinh 2Kh}$$
(27a)

and the amplitude of the dynamic pressure force due to the evanescent modes is given by

$$F_{e} = \frac{HBK}{2\sinh Kh} \left[\frac{K}{\kappa} \right]^{1/2} \left[\frac{1 + \frac{2\kappa h(1 - \Delta)}{\sinh 2\kappa h(1 - \Delta)}}{1 + \frac{2Kh}{\sinh 2Kh}} \right]^{1/2}$$

$$(2Kh + \sinh 2Kh)$$

 $[Kh(1-\delta) \sinh Kh - \cosh Kh + \cosh Kh\delta]$

$$\sum_{n=2}^{\infty} \frac{[K_n h(1-\delta) \sin K_n h + \cos K_n h - \cos K_n h \delta]}{K_n^3 (2K_n h + \sin 2K_n h)} (\sin K_n h - \sin K_n h \delta)$$
 (27b)

Eqs. 27a and 27b may again be shown to reduce to Eqs. 21b and 21c, respectively, given by Hyun (Ref. 7, p. 4) for the previously noted special geometry. In addition, Eq. 27a may be shown to reduce to the dimensionless propagating force component (termed resistive component) for the special constant depth case treated by Gilbert, et. al (Ref. 3, Table 1, p. 184), but not to their dimensionless evanescent pressure force component (termed inertial component). The reason for this lack of equivalence for the evanescent modes is not known. Numerical values estimated from their design curve (Ref. 3, Fig. 2, p. 165) do, however, agree with numerical values computed from Eq. 27b for the equivalent special wave flume geometry.

The relationships between the magnitude of the measured hydrodynamic pressure force, |F|, and the magnitudes of the theoretical components of the total hydrodynamic pressure force are easily shown to be the following (compare to Appendix I):

$$F_p = |F| \sin(\alpha_F - \alpha) \dots (28a)$$

$$F_e = |F| \cos(\alpha_F - \alpha) \qquad (28b)$$

The theoretical relative force phase angle, β_F , between the total hydrodynamic pressure force and the displacement of the wavemaker is given by

which may be computed from the measured FFT coefficients which are referenced to the displacement of the wavemaker by subtracting the two measured phase angles according to (compare to appendix I)

$$\beta_F = \alpha_F - \alpha \qquad (28d)$$

Again, by comparing the real parts of the components of the horizontal

wavemaker velocity computed from $u=u_p+u_e$, it may be shown that the propagating component of the wavemaker force, $F_p \sin{(t+\alpha)}$, given by Eq. 26b is in-phase with the horizontal component of the wavemaker velocity; while the evanescent component of the wavemaker force, $F_e \cos{(t+\alpha)}$, is in-phase with the horizontal component of the wavemaker acceleration. Note that these are the horizontal components of the angular velocity of the wavemaker.

The amplitude values computed from the evanescent eigenmode summations in Eq. 27b become negative for summations in relative water depths less than $h(1-\Delta)/L_o < 0.4$. This indicates that for most intermediate and shallow water conditions, the hydrodynamic pressure force leads the wavemaker velocity in a phase vector diagram; while for deep water relative depth conditions, the hydrodynamic pressure force lags the wavemaker velocity phasor. These phasor relationships are shown schematically in Fig. 3. Summation values for the evanescent eigenmode component of the moment never become negative over

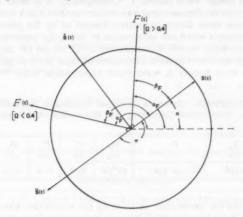


FIG. 3.—Phase Vector Diagram for Hinged Wavemaker Pressure Force for Wavemaker Displacement Phase Vector $S(t) = S/2 \exp i(\omega t + \alpha)$

the two decades of dimensionless frequency which were computed. We note that the relative phase angles computed by Eqs. 25c and 28c are referenced to the wavemaker displacement and are, therefore, complementary phase angles to those given by Hyun (Ref. 7, Table 2, p. 6) which are referenced to the wavemaker velocity.

Finally, neglecting the viscous and mechanical losses of the wavemaker system, the average rate of power required by the wavemaker to do work on a column of fluid on only one side of the wavemaker may be computed by temporally averaging the rate of work done by the hydrodynamic pressure force on a column of fluid according to

$$\langle \dot{W} \rangle = B \int_{h(\delta-1)}^{0} \langle R \left[\Phi_{x}(o,y,t) \right] R \left[-\Phi_{x}(o,y,t) \right] \rangle dy \dots \qquad (29)$$

in which the brackets, $\langle \cdot \rangle$, denote the temporal averaging operator for simple harmonic motion and R denotes the real part of a complex-valued quantity. Due to the orthogonality of the orthonormal eigenfunctions, $f_n(y)$, and to the periodicity of the averaging operator, it can be shown that the evanescent eigenmodes do not contribute to the average rate of work and that

$$\langle \dot{W} \rangle = \frac{BH^2}{16 K_K \tanh Kh} \left[1 + \frac{2\kappa h (1 - \Delta)}{\sinh 2\kappa h (1 - \Delta)} \right] \dots (30)$$

DESIGN CURVES FOR HINGED WAVEMAKERS

The dimensional design parameters which are most frequently specified for experimental work in wave flumes are the design wave height, H, design water depth, h, and design wave period, T. Consequently, it is more desirable to nondimensionalize the dimensionless wavemaker variables which were previously derived by these three design parameters instead of by the previously given universal parameters which are independent of the design parameters of wave height and wavemaker stroke. Dimensionless design curves for the wavemaker variables which have been nondimensionalized by these three design parameters may be used more directly in wave flume experimental work. Note that we

TABLE 1.—Dimensionless Parameters for Hinged Wavemaker (Repeating Variables: Fluid Density, ρ; Gravitational Constant, g; and Wavemaker Fluid Depth, h)

Π, (1)	Π ₂ (2)	П ₃ (3)	П ₄ (4)	П ₅ (5)	П ₆ (6)	Π ₇ (7)	П _в (8)
M/pgh4	F/pgh3	$\bar{W}/\rho gh^3(gh)^{1/2}$	gT^2/h	S/h	B/h	H/h	$(1-\delta)$

do not normalize the wavemaker variables by the wavemaker stroke, S, since this parameter is not known a priori but must be computed from the wavemaker gain function using the specified design wave height. The numerical computations which are needed to construct the dimensionless design curves require summing an infinite series for the evanescent eigenmodes. These series summations were truncated when the addition of a single term failed to change the sum by more than 0.1% (compare to Gilbert, et. al (3)]. We also return to dimensional variables but omit the superscript asterisk (*) for convenience.

Table I summarizes the dimensionless parameters obtained from a dimensional analysis for forced harmonic surface gravity waves generated in the wave flume shown in Fig. 1 if the repeating variables are chosen to be the fluid density, ρ , the gravitational constant, g, and the wavemaker fluid depth, h. Forming various ratios with these dimensionless parameters yields the following dimensionless wavemaker design curve variables:

$$M' = \frac{M}{\frac{1}{2} \rho gBHh^2 (1-\delta)}$$
 (31a)

$$\mathbf{F}' = \frac{\mathbf{F}}{\frac{1}{2} \rho gBHh(1-\delta)} \tag{31b}$$

$$W' = \frac{\langle \dot{W} \rangle}{\frac{1}{8} \rho g H^2 B (gh)^{1/2}}$$
 (31c)

$$\Omega = \frac{h(1-\Delta)}{L} \tag{31d}$$

in which the superscript primes denote dimensionless variables and the deep water wave length computed from linear wave theory is

$$L_o = \frac{gT^2}{2\pi} \tag{32}$$

The amplitude of the dimensionless hydrodynamic moment on the hinged wavemaker due to the propagating mode [termed resistive component by Gilbert, et. al (3)] is now given by

$$M'_{p} = 2\pi\Omega \frac{[Kh(1-\delta)\sinh Kh - \cosh Kh + \cosh Kh\delta]}{(Kh)^{3}(1-\delta)(1-\Delta)\sinh Kh} \left[\frac{K}{\kappa}\right]^{1/2} \left[\frac{1 + \frac{2\kappa h(1-\Delta)}{\sinh 2\kappa h(1-\Delta)}}{1 + \frac{2Kh}{\sinh 2\kappa h}}\right]^{1/2}$$
(33a)

and due to the evanescent modes [termed inertia component by Gilbert, et. al (3)] by

$$M'_{e} = 2\pi\Omega \frac{(Kh)(2Kh + \sinh 2Kh)}{(1 - \delta)(1 - \Delta)\sinh Kh \left[Kh(1 - \delta)\sinh Kh - \cosh Kh + \cosh Kh\delta\right]} \left[\frac{K}{\kappa}\right]^{1/2}$$

$$\left[\frac{1 + \frac{2\kappa h(1-\Delta)}{\sinh 2\kappa h(1-\Delta)}}{1 + \frac{2Kh}{\sinh 2Kh}}\right]^{1/2} \sum_{n=2}^{\infty} \frac{\left[K_n h(1-\delta)\sin K_n h + \cos K_n h - \cos K_n h\delta\right]^2}{\left(K_n h\right)^4 (2K_n h + \sin 2K_n h)}$$
(33b)

The magnitudes of the dimensionless evanescent, propagating and total hydrodynamic moments are shown in Fig. 4 for various wave flume geometries. By nondimensionalizing the hydrodynamic moment on the wavemaker by the three previously identified design wave parameters of H, T, and h, Eqs. 33a and 33b now become independent of the dimensionless height of the wavemaker stroke above the hinge, H. Note also that the minimum value of the dimensionless hydrodynamic moment is easily located graphically in this Gilbert, et. al (3) type of figure in contrast to the diagonal term look-up method presented by Hyun (Ref. 7, Table 2).

The amplitude of the dimensionless hydrodynamic pressure force due to the propagating mode [termed resistive by Gilbert, el. at (3)] is now given by

$$F'_{\rho} = 2\pi\Omega \frac{(\sinh Kh - \sinh Kh\delta)}{(Kh)^{2}(1 - \delta)(1 - \Delta)\sinh Kh} \left[\frac{K}{\kappa}\right]^{1/2} \left[\frac{1 + \frac{2\kappa h(1 - \Delta)}{\sinh 2\kappa h(1 - \Delta)}}{1 + \frac{2Kh}{\sinh 2Kh}}\right]^{1/2}$$
(34a)

and due to the evanescent eigenmodes [termed inertia by Gilbert, et. al (3)] by

$$F_{\kappa}' = \frac{2\pi\Omega \ Kh(2Kh + \sinh 2Kh)}{(1 - \delta)(1 - \Delta) \sinh Kh \left[Kh(1 - \delta) \sinh Kh - \cosh Kh + \cosh Kh\delta\right]} \left[\frac{K}{\kappa}\right]^{1/2}$$

$$\left[\frac{1 + \frac{2\kappa h(1 - \Delta)}{\sinh 2\kappa h(1 - \Delta)}}{1 + \frac{2Kh}{\sinh 2Kh}}\right]^{1/2} \sum_{n=2}^{\infty} \frac{\left[K_n h(1 - \delta) \sin K_n h + \cos K_n h - \cos K_n h\delta\right]}{(K_n h)^3 (2K_n h + \sin 2K_n h)}$$

$$(\sin K_n h - \sin K_n h\delta) \qquad (3)$$

Hyun (Ref. 7, Table 2, p. 6) tabulated the relative contributions from each of the two components of the total hydrodynamic pressure force and moment

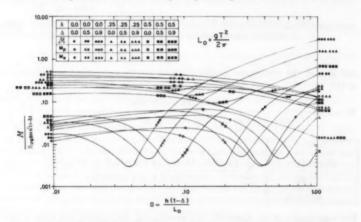


FIG. 4.—Dimensionless Hydrodynamic Moment, M^\prime , as Function of Wave Flume Geometry

as a function of the dimensionless relative water depth. These relative effects were determined from the phase angles between the hydrodynamic pressure force or moment and the velocity of the hinged wavemaker. Since the two components of pressure due to the propagating (or resistive) and evanescent (or inertia) modes are 90° out-of-phase with respect to each other, these comparisons of relative phase angles reflect the relative importance of each hydrodynamic component to the total pressure force or moment. This comparison

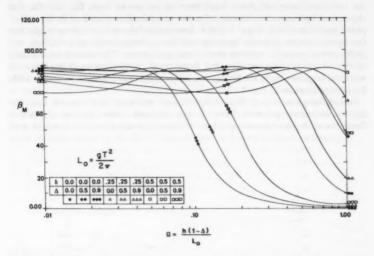


FIG. 5.—Relative Phase Angle, β_M , between Total Hydrodynamic Moment and Displacement of Wavemaker

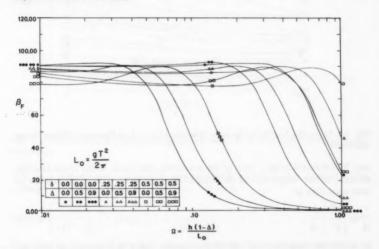


FIG. 6.—Relative Phase Angle, $\beta_{\it F}$, between Total Hydrodynamic Force and Displacement of Wavemaker

is more easily demonstrated in the Gilbert, et. al (3) type of graph in which the relative theoretical phase angle may be computed from Eq. 25c for the theoretical hydrodynamic moment for the special case of zero arbitrary initial phase angle or $\alpha=0$. Figs. 5 and 6 demonstrate the relative phase angle for the hydrodynamic pressure moment and force, respectively in a Gilbert, et. al (3) type of graph for various wave flume geometries. The relative importance of the evanescent eigenmodes for deep water conditions as a function of wavemaker geometry is readily apparent by comparing these phase angles with the phasor diagram in Fig. 3.

In the design curves presented by Gilbert, et. al (3), the moment arm for the hydrodynamic pressure force, *l*, was assumed to be equal to the wave flume water depth at the wavemaker. A theoretical dimensionless moment arm

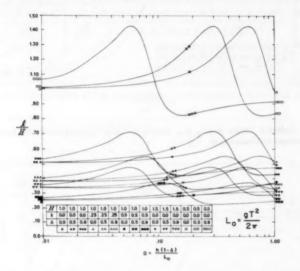


FIG. 7.—Dimensionless Hydrodynamic Moment Arm, $l/{\rm H}_{\rm r}$ as Function of Wave Flume Geometry

may be estimated from a ratio of the maximum amplitude of the hydrodynamic moment to the magnitude of the hydrodynamic force at the same instant of time according to

$$\frac{l}{H} = \left| \frac{M'}{F'} \right| \frac{h}{H} \dots \tag{35}$$

in which the magnitude of the hydrodynamic force is evaluated at $t = \alpha_M$ (see Eq. 26c).

Fig. 7 demonstrates the effects of the wavemaker and the wave flume geometries on the dimensionless theoretical moment arm. The ratio of hydrodynamic moment arm to wave flume water depth is less than unity for the wave flume geometry

analyzed by Gilbert, et. al (3) (viz, H = 1.0, $\delta = \Delta = 0.0$) which indicates that, theoretically, their values are conservative for design applications.

Hyun (Ref. 7, Fig. 3, p. 5) also presents a graph of the dimensionless average wavemaker power versus a dimensionless relative water depth and concludes that this dimensionless quantity is independent of the wavemaker geometry (viz, the height of the wavemaker hinge and the location of the measurement of the wavemaker stroke above the bottom). It is well-known that if the frictional and mechanical losses in a wavemaker are neglected, then the average rate of power required by a wavemaker is identically equal to the average rate of energy flux in the propagating wave component. If the average rate of power required by any wavemaker is nondimensionalized by the average rate of energy flux in the propagating wave, then this dimensionless quantity is a constant equal to unity which is obviously independent of the wavemaker geometry.

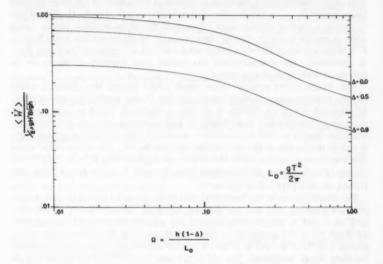


FIG. 8.—Dimensionless Average Wavemaker Power, (W^\prime), as Function of Wave Flume Geometry

From a dimensional analysis, it may be readily shown that a dimensionless average wavemaker power may be computed from

$$\langle W' \rangle = \left[\frac{\pi \Omega}{2(1-\Delta)} \right]^{1/2} (\kappa h)^{-1} \left[1 + \frac{2\kappa h(1-\Delta)}{\sinh 2\kappa h(1-\Delta)} \right] \dots \dots \dots (36)$$

Fig. 8 demonstrates the effects of the wave flume geometry on the dimensionless wavemaker power. The special case of $\Delta=0$ corresponds to the wave flume geometry treated by Hyun (7) provided his dimensionless power is divided by the square root of the gravitational constant, g. Evidently, the choice of variables used to nondimensionalize the dimensionless average wavemaker power is

responsible for the functional dependency of this design variable on the geometry of the wavemaker.

CONCLUSIONS

The design curves presented by Gilbert, et. al (3) for the generation of periodic waves by hinged wavemakers are extended to variable-draft hinged wavemakers in wave flumes consisting of two constant depth domains which are connected by a gradually sloping transition region in which wave reflections are assumed to be negligible. These types of design curves when nondimensionalized by the design parameters of H, T, and h, are found to present the important design considerations better than the tabular method presented by Hyun (7).

Specifically, the dimensionless wavemaker gain function, S/H, shown in Fig. 2 for various geometries is shown to increase with an increase in the dimensionless hinge height, δ , for a fixed value of wavemaker stroke height, H. The effect is simply a vertical displacement upward of this dimensionless design curve without change in shape. On the other hand, if the dimensionless hinge height, δ , is increased while the wavemaker stroke is held at a constant elevation (i.e., H decreased), the dimensionless wavemaker gain function design curve is

decreased without change in shape.

The dimensionless relative water depth which locates the minimum value for the dimensionless moment amplitude due to the evanescent eigenmodes, M'_{ϵ} [termed interia by Gilbert, et. al (3)], is shown in Fig. 4 to increase with increasing dimensionless hinge height, δ , and increasing constant dimensionless transition height, Δ . The dimensionless maximum total moment amplitude, M', is almost totally due to the propagating eigenmode, M'_{ρ} , for intermediate water depth and almost totally due to the evanescent eigenmodes, M'_{ϵ} , for deep water depths. The minimum dimensionless total moment is easily found from this Gilbert, et. al (3) type of design curve.

The design curves for the theoretical relative phase angles for the hydrodynamic pressure moment, β_M , and for the hydrodynamic pressure force, β_F , shown in Figs. 5 and 6, respectively, support the relative importance demonstrated by Hyun (7) of the amplitude of the propagating mode for intermediate water depths (i.e., $\Omega < 0.5$ and $\beta \sim 90^\circ$) while the evanescent eigenmodes dominate for deep water conditions {i.e., $\Omega > 0.5$ and $\beta \sim 0^\circ$ }. These phase angles are referenced to the displacement of the wavemaker and are, therefore, complementary phase-angles to those computed by Hyun (7).

The parametric dependency of the dimensionless power, W', for a hinged wavemaker on the geometry of the wave flume is shown to depend upon the variables used to nondimensionalize the wavemaker power and caution should be exercised when drawing conclusions about the power requirements for hinged wavemakers of variable draft [compare Hyun (7) p. 4 and Fig. 3, p. 5].

Experimental verifications of these theoretical dimensionless design curves were obtained in the OSU-WRF for wave heights which are approx 25% of the theoretical breaking wave height and the results are presented in the companion paper (6).

Since it is the dimensionless wavemaker moment, M', which is usually required for the design of hinged wavemakers and since experimental verifications in the OSU-WRF were obtained for the wavemaker moment in order to avoid

having to estimate the moment arm for the hydrodynamic pressure force, no design curves for wavemaker forces have been presented. The amplitudes for the evanescent eigenmode forces given by Eq. 27b become negative for relative water depths less than $h(1-\Delta)/L_o < 0.4$; while no negative summations were obtained for the evanescent component of the moment. In order to obtain an accuracy of 0.1%, 27 evanescent eigenmode terms were required for the most extreme deep water case computed by Hyun (Ref. 7, Table 2, p. 6). Most other cases in intermediate water depths required less than five evanescent terms in order to obtain 0.1% accuracy.

ACKNOWLEDGMENTS

We are grateful for the financial support provided by the National Science Foundation Grant No. ENG75-10496 and by the Oregon State University Sea Grant College Program, Department of Commerce, under Grant No. 04-6-158-44004. Numerous discussions with T. Yamamoto on forced harmonic waves have substantially improved an earlier draft; and we appreciate both his time and his incisive comments.

APPENDIX I.—RESOLUTION OF THEORETICAL PHASE ANGLES FROM FFT DATA

The theoretical relative phase angle between the displacement of the wavemaker and the hydrodynamic pressure moment may be readily computed by first expanding the hydrodynamic pressure moment given by Eq. 23c according to the following angle sum identity:

$$|M|\cos(t+\alpha_M) = |M|\cos t\cos\alpha_M - |M|\sin t\sin\alpha_M \dots (37)$$

Expanding Eq. 23b similarly and equating coefficients of $\sin t$ and $\cos t$ separately yields the following two equations:

$$-M_{\rho}\cos\alpha + M_{e}\sin\alpha = -|\mathbf{M}|\sin\alpha_{M} \quad ... \quad (38)$$

$$-M_{p} \sin \alpha - M_{e} \cos \alpha = |\mathbf{M}| \cos \alpha_{M} \dots (39)$$

which gives the following solutions for the amplitudes of the components of the hydrodynamic moment:

$$M_p = |M| \sin{(\alpha_M - \alpha)} = |M| \sin{(\beta_M)} \dots (40)$$

$$-M_e = |M|\cos(\alpha_M - \alpha) = |M|\cos(\beta_M)\dots$$
 (41)

in which the theoretical phase angle, β_M , is relative to the wavemaker displacement and Eq. 25d follows. Resolution of the theoretical relative phase angle for the hydrodynamic pressure force on the wavemaker, β_F , follows in an analogous manner.

APPENDIX II.—REFERENCES

- Biesel, F., and Suquet, F., "Laboratory Wave Generating Apparatus," Project Report 39, St. Anthony Falls Hydraulic Laboratory, Minnesota University, Minneapolis, Minn., 1953.
- 2. Eagleson, P. S., and Dean, R. G., "Small Amplitude Wave Theory," Estuary and

Coastline Hydrodynamics, A. T. Ippen, ed., McGraw-Hill, New York, N.Y., 1966, pp. 49-77.

HYS

- 3. Gilbert, G., Thompson, D. M., and Brewer, A. J., "Design Curves for Regular and Random Wave Generators," Journal of Hydraulic Research, Vol. 9, No. 2, 1971,
- 4. Gilbert, S., Thompson, D. M., and Brewer, A. J., Closure to "Design Curves for Regular and Random Wave Generators," Journal of Hydraulic Research, Vol. 10, No. 2, 1972, pp. 233-236.
- 5. Havelock, T. H., "Forced Surface-Wave on Water," Philosophical Magazine, Series F., Vol. 8, 1929, pp. 569-576.
- 6. Hudspeth, R. T., Leonard, J. W., and M.-C. Chen, "Design Curves for Hinged Wavemakers: II-Experiments," Journal of the Hydraulics Division, ASCE, Vol. 107, No. HY5, Proc. Paper 16237, May, 1981, pp. 553-574.
- 7. Hyun, J. M., "Theory for Hinged Wavemakers of Finite Draft in Water of Constant
- Depth," Journal of Hydronautics, Vol. 10, No. 1, Jan., 1976, pp. 2-7.

 8. Kennard, E. H., "Generation of Surface Waves by a Moving Partition," Quarterly of Applied Mathematics, Vol. 7, No. 3, 1949, pp. 303-312.
- 9. Kreisel, G., "Surface Waves," Quarterly of Applied Mathematics, Vol. 7, 1949, pp. 21-44.
- 10. Krishnamacker, P., discussion of "Design Curves for Regular and Random Wave Generators," by G. Gilbert, D. M. Thompson, and A. J. Brewer, Journal of Hydraulic Research, Vol. 10, No. 2, 1972, pp. 227-233.
- 11. Madsen, O. S., "Waves Generated by a Piston-Type Wavemaker," Proceedings of the Twelfth Coastal Engineering Conference, Vol. 1, Sept., 1970, pp. 589-607.
- 12. Multer, R. H., "Exact Nonlinear Model of Wave Generator," Journal of the Hydraulics Division, ASCE, Vol. 99, No. HY1, Proc. Paper 9467, Jan., 1973, pp. 31-46.
- 13. Ursell, F., Dean, R. G., and Yu, Y. S., "Forced Small Amplitude Water Waves: A Comparison of Theory and Experiment," Journal of Fluid Mechanics, Vol. 7, Part 3, 1960, pp. 33-52.

APPENDIX III.—NOTATION

The following symbols are used in this paper:

- A_n = multiplicative coefficient for nth eigenfunction of velocity potential;
 - B = total width of wavemaker;
 - unit vector in right-handed Cartesian coordinate sys-
 - = dimensionless total hydrodynamic pressure force:
 - F_{e} = hydrodynamic pressure force amplitude due to evanescent eigenmodes:
 - F_n = hydrodynamic pressure force amplitude due to propagating eigenmode;
 - f_n = orthonormal eigenfunction;
 - = gravitational constant;
 - H = deterministic wave height;
 - h = still water depth at wavemaker;
- -1 = imaginary unit;
 - = wave number for propagating eigenmode in constant depth domain adjacent to wavemaker $(= iK_1)$;
 - K_n = wave number for evanescent eigenmodes $(n \ge 2)$;
- $L_a = gT^2/2\pi$ = deep water wave length;
 - l = moment arm for total hydrodynamic pressure force

measured vertically above wave flume bottom;

M = dimensionless total hydrodynamic moment on wavemaker:

M_{*} = dimensionless hydrodynamic moment amplitude due to evanescent eigenmodes;

 M_p = dimensionless hydrodynamic moment amplitude due to propagating eigenmode;

N_n = normalizing constant for nth orthonormal eigenfunction:

n = summation index for orthonormal eigenfunctions;

p = hydrodynamic pressure;

 $\mathbf{q} = u\mathbf{e}_x + v\mathbf{e}_y + w\mathbf{e}_z = \text{velocity vector};$

 $\mathbf{r} = x\mathbf{e}_x + y\mathbf{e}_y + z\mathbf{e}_z = \text{position vector};$

S = wavemaker stroke measured at height of wavemaker piston;

S = Stokes' material coordinate for wavemaker displacement;

T = wave period;

t = time;

u = horizontal component of water particle velocity;

v = vertical component of water particle velocity;

 (\dot{W}) = average wavemaker power:

w = horizontal component of water particle velocity normal to x-y plane;

x = horizontal coordinate axis with origin located at undisturbed water level at wavemaker;

y = vertical coordinate axis with origin located at still water level at wavemaker:

z = horizontal coordinate axis which is normal to x-y plane in right-handed Cartesian coordinate system:

α = arbitrary initial phase angle for wavemaker displacement due to FFT digitizing process:

 α_F = measured relative phase angle for measured hydrodynamic pressure force;

α_M = measured relative phase angle for measured hydrodynamic pressure moment;

β_F = theoretical relative phase angle between hydrodynamic force and displacement of wavemaker;

β_M = theoretical relative phase angle between hydrodynamic pressure moment and displacement of wavemaker:

Δ = dimensionless vertical transition height between two constant depth wave flume domains;

 δ = dimensionless height of wavemaker hinge above bottom:

ζ = dimensionless depth below still water level to wavemaker piston;

 $H = (1 - \delta - \zeta)$ = dimensionless height of wavemaker piston measured above wavemaker hinge;

- η = instantaneous water surface elevation measured positive upwards from undisturbed still water level;
- κ = wave number for propagating eigenmode in constant depth test domain;
- ξ = vertical dependence of prescribed wavemaker displacement;
- ρ = fluid density;
- Φ = temporal and spatial scalar velocity potential;
- φ = spatial scalar velocity potential;
- x = prescribed wavemaker displacement;
- Ω = relative water depth;
- $\omega = 2\pi/T$ = radian frequency; $\nabla = (\partial/\partial x) e_x$
 - $+ (\partial/\partial y) e_{x}$
 - $+ (\partial/\partial z) e_z = \text{gradient operator; and}$
 - () = averaging operator.

Superscripts

- * = dimensional variable; and
- ' = dimensionless dependent variables.

Subscripts

- $e = \text{evanescent mode } (n \ge 2)$:
- F = hydrodynamic pressure force;
- M = hydrodynamic pressure moment;
- n = eigenfunction mode summation;
- o = deep water conditions;
- p = propagating eigenmode (n = 1);
- x = x coordinate axis;
- y = y coordinate axis; and
- z = z coordinate axis.

DESIGN CURVES FOR HINGED WAVEMAKERS: EXPERIMENTS

By Robert T. Hudspeth, M. ASCE, John W. Leonard, A. M. ASCE, and Min-Chu Chen³

INTRODUCTION

The theory for the elaborate design curves for hinged wavemakers presented by Gilbert, et. al (4) has been extended within the limits of linearized potential wave theory for hinged wavemakers of variable draft in the companion paper (6) for wave flume geometries which consist of two horizontal constant depth domains connected by a gradually sloping transition region (compare to Fig. 1). These Gilbert, et. al type of design curves were shown in the companion paper to demonstrate the effects of wavemaker and wave flume geometry on the design curve variables better than the tabular look-up method presented by Hyun (8) for hinged wavemakers of variable draft. However, experimental verifications of these design curve variables for variables other than the dimensionless wavemaker gain function, S/H, appear to be scarce.

The design curve variables for the wavemaker gain function, S/H, dimensionless hydrodynamic moment magnitude, M', and relative phase angle, β_M , were measured in the Oregon State University—Wave Research Facility (OSU-WRF) in two water depths for over one decade of dimensionless wave frequency. Comparisons with theoretical values for those wavemaker design variables which are presented in the companion paper indicate generally good agreement for deterministic waves which are approx 25% of the theoretical breaking wave height. These comparisons of measured data with the magnitudes and phases of the hydrodynamic moment on a hinged wavemaker are believed to be unique.

WAVE FLUME DESCRIPTION

The theoretical design curve values derived in the companion paper are compared with a unique set of data recorded in the OSU-WRF shown in Fig.

¹Assoc. Prof., Dept. of Civ. Engrg. and Ocean Engrg. Programs, Oregon State Univ., Corvallis, Oreg. 97331.

² Prof., Dept. of Civ. Engrg. and Ocean Engrg. Programs, Oregon State Univ., Corvallis, Oreg. 97331.

³Sr. Research Engr., Offshore System Div. Exxon Production Research Co., Houston, Tex. 77001; formerly, Grad. Research Asst., Dept. of Civ. Engrg., Oregon State Univ., Corvallis, Oreg. 97331.

Note.—Discussion open until October 1, 1981. Separate discussions should be submitted for the individual papers in this symposium. To extend the closing date one month, a written request must be filed with the Manager of Technical and Professional Publications, ASCE. Manuscript was submitted for review for possible publication on March 11, 1980. This paper is part of the Journal of the Hydraulics Division, Proceedings of the American Society of Civil Engineers, ©ASCE, Vol. 107, No. HY5, May, 1981. ISSN 0044-796X/81/0005-0553/\$01.00.

1. The wave flume is 89.64 m tong, 3.66 m wide, and has a relocatable bottom in the test section. Experimental data were obtained for two water depths at the wavemaker of h = 3.96 m and 4.42 m.

The hinged wavemaker in the OSU-WRF is sealed under pressure along both vertical sides and the horizontal hinged bottom so that water is not required in the dry well behind the wavemaker. This dry well reduces the power requirements for the wavemaker and also eliminates the need to place any wave dissipating material behind the wavemaker. The hinged wavemaker is controlled by a 112-kW, 20.7-MPa hydraulic pump through a hydraulic servo-mechanism mounted 3.05 m above the wavemaker hinge. The forced motion of the wavemaker may be either random or periodic and is activated by either an electronic function generator or a digital time sequence synthesized on a PDP 11 E10 digital minicomputer through digital-to-analog converters (DAC). A description of a unique inverse finite Fourier transform algorithm (FFT)

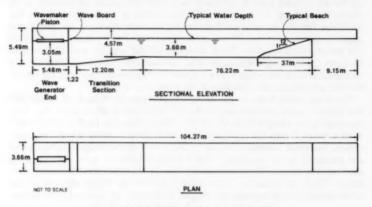


FIG. 1.—Wave Flume Geometry of OSU-WRF

developed at the OSU-WRF to generate both periodic and random waves of the periodic-random type through a minicomputer is given by the first writer and Borgman (5). The periodic motions of the hinged wavemaker which were used to verify the linear theory wavemaker design curves for periodic waves were also synthesized from a stacked FFT digital computer algorithm using the theoretical wavemaker gain function, S/H. A more detailed description of the wave generating characteristics of the OSU-WRF is given by Sollitt and Huber (9).

The wave heights and periods selected for experimental verification were determined from the dimensionless relative wave height-relative water depth dissection plane given by Dean (Ref. 3, Fig. 23, p. 39). Wave heights which were 25% of the theoretical breaking wave height were selected for verifying the linear wave theory design curves. The desired wave height, H, wave period, T, and wave flume water depth in the test section, h- Δ , were input to the minicomputer stacked FFT algorithm; and a discrete sinusoidal time sequence

for the displacement of the wavemaker was synthesized and output to the hydraulic servomechanism which activates the hinged wavemaker through the minicomputer DAC. This digital simulation procedure also permits the computation of an additional complex-valued wavemaker gain function which is the result of the servo-mechanism in the hydraulic system by correlating the measured wavemaker motion, S_m , with the minicomputer DAC signal for the theoretical wavemaker stroke, S_T . The design wave parameters specified for the experimental verification are identified in Fig. 2 on the dimensionless relative wave height-relative water depth dissection given by Dean (3).

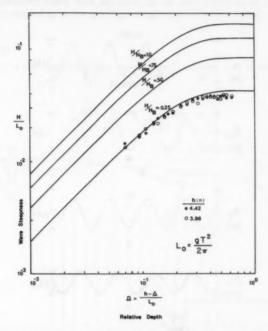


FIG. 2.—Relative Wave Height-Relative Water Depth Dissection Plane Used to Determine Theoretical 25% Breaking Wave Heights for Experimental Verification in OSU-WRF [from Dean (3)]

Experimental verification of the linear theory wavemaker design curves in the OSU-WRF consisted of verifying the following wavemaker variables: (1) The dimensionless gain function, S/H; (2) the magnitude of the total dimensionless hydrodynamic pressure moment on the wavemaker, M', and the relative phase angle between the hydrodynamic pressure moment and the displacement of the wavemaker, $\beta_{M'}$; or equivalently (3) the propagating, M'_{ρ} , and evanescent, M'_{σ} , components of the total dimensionless hydrodynamic pressure moment. The dimensionless hydrodynamic pressure moment was selected for verification

instead of the dimensionless hydrodynamic pressure force because verification of the hydrodynamic pressure moment avoids having to estimate the moment arm of the total hydrodynamic pressure force theoretically [compare Gilbert, et. al (4)].

EXPERIMENTAL DATA RECORDING

An example of a visual analog record of the measured data recorded in the OSU-WRF water depth at the wavemaker of h = 3.96 m is reproduced in

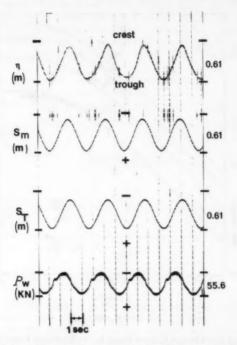


FIG. 3.—Sample Visual Analog Data Record ($H=0.55~\mathrm{m},~T=3.45~\mathrm{sec},~\mathrm{and}~h=4.42~\mathrm{m}$)

Fig. 3. The dimensionless wavemaker gain function was computed from a ratio of the measured wavemaker stroke, S_m , to the measured wave height, H. The measured wavemaker stroke was recorded through an LVDT mounted just above the wavemaker hinge in the dry well behind the wavemaker (vide, Fig. 1). This LVDT signal was calibrated by rotating the wavemaker through a discrete set of arcs measured at the height of the wavemaker piston and correlating the LVDT signal with those measured rotations. The wave heights were computed from a measurement of the instantaneous water surface elevation in the test

section of the wave flume by a Sonic System Model 86 sonic wave profiler. The sonic wave profiler was calibrated by displacing the sonic transducer through a discrete sequence of vertical distances measured above the still water level in the absence of waves and correlating the sonic transducer signal with these measured displacements.

All of the experimental amplitudes and relative phase angles were computed from FFT coefficients which were computed from the digitized analog signals using the integer FFT algorithm contained in the SPARTA subroutine of the Lab Peripheral System written by DEC for the PDP 11 E10. Exactly four periods of each measured signal were analyzed by the FFT algorithm at a sampling interval determined from the specified design wave period according to

in which T = the specified design wave period. The data used in the analyses

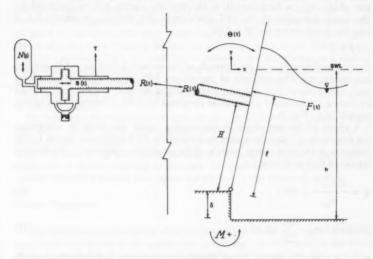


FIG. 4.—Schematic Representation of Hinged Wavemaker Piston and Flap System in OSU-WRF

were recorded just after steady-state conditions were observed to be established on the visual analog records but before any major reflections could propagate back from the terminating beach. The measured data were, therefore, not corrected for reflections from the terminating beach.

The measured analog signals shown in Fig. 3 were Fourier analyzed by FFT algorithm in order to more accurately estimate their magnitude and phase [compare to Clough and Penzien (2)]. For a complex-valued discrete time sequence $\{U_n\}$, the discrete FFT pair is given by

$$U_n = W^{-1} \sum_{m=0}^{W-1} X_m \exp i\left(\frac{2\pi nm}{W}\right); \quad n = 0, 1, 2, ..., W-1 \dots (2a)$$

$$X_{m} = \sum_{n=0}^{W-1} U_{n} \exp -i \left(\frac{2\pi nm}{W} \right); \quad m = 0, 1, 2, ..., W-1 \dots (2b)$$

in which the real and imaginary components of the complex-valued FFT coefficients are identified by

Only the real part of the discrete complex-valued time sequence $\{U_n\}$ represents the physical process synthesized from Eq. 2a for an unstacked FFT algorithm. In order for the inverse transform to be exact, we must also require that

Since exactly four periods of measured data were digitized, the amplitude and phase for the fundamental of the periodic signals will be displayed by the fourth harmonic of the FFT coefficients. To illustrate, substitute Eq. 1 into Eq. 4 and obtain for W = 4,096

Fourier analyzing exactly four periods of the measured data served to average the amplitudes. The accuracy of the integer FFT algorithm which partitions each analog signal into unsigned integer values between 0-4,095 was verified by manual computations using values computed from the calibrated visual analog records (e.g., Fig. 3).

A check of the periodicity in each analog signal was made by comparing the magnitude of twice the square modulus of the FFT coefficient for the fourth harmonic to the total energy content of the amplitude spectrum for the discrete measured time sequence; i.e.:

in which
$$m_0 = \sum_{m=0}^{W-1} |X_m|^2$$
....(7)

and j = subscript symbol which identifies a particular measured data signal. The closer the value of the ratio computed from Eq. 6 is to 100%, the more linear or sinusoidal the process. The lower the value of γ_j , the less the variance of the Fourier analyzed signal may be explained by the fourth harmonic.

One way in which the theoretical total pressure force on a wavemaker could be verified experimentally would be by measuring with pressure transducers the hydrodynamic pressure at discrete vertical elevations along the hinged wavemaker face and then integrating these pressures numerically. On the other hand, it is the total force required to drive the wavemaker that is of interest in the design of wavemakers; and it was the moment induced by this force which was measured to verify the linear wavemaker theory in the OSU-WRF.

A differential pressure transducer was installed in the MTS 406 Controller

System which activates the hinged wavemaker in order to measure the time varying pressure signal of the hydraulic oil piston pressure which oscillates the wavemaker piston and which is used in the feedback control system (vide, Fig. 4). The voltage output from this differential pressure transducer was calibrated to provide an analog signal of the hydraulic oil piston pressure force which drives the wavemaker piston and oscillates the hinged wavemaker. This measured hydraulic oil piston pressure force could then be used with Newton's second law of motion to measure the hydrodynamic wave pressure moment on the wavemaker. Again, the hydrodynamic pressure moment was selected for verification of the design curves presented in the companion paper since the moment arm to the piston pressure force, H, could be accurately measured and we avoid having to estimate theoretically the hydrodynamic moment arm to the hydrodynamic pressure force, I.

The voltage signal from the hydraulic oil differential pressure transducer was calibrated by correlating the voltage output from the hydraulic oil pressure transducer required to maintain the wavemaker in a neutral vertical position against a static column of water of known height on one side only of the wavemaker. A calibration curve for the hydraulic oil piston pressure force was obtained by increasing the static water depths on one side of the wavemaker by flooding the wave flume at discrete increments of water depth. No hydraulic oil piston pressure force was required to maintain the wavemaker in a neutral vertical position until approx 1 m of static water pressure moment was attained in the wave flume. This provided an estimate of the static Coulomb friction force provided by the pressurized plastic seals located on the vertical sides of the wavemaker.

The measured hydrodynamic moment on the wavemaker was calculated from Newton's second law of motion using the calibrated differential hydraulic oil piston pressure transducer signal from the hydraulic servo-mechanism recorded both with water in the wave flume and with the wave flume drained. The dynamic equations of motion required to measure the hydrodynamic pressure moment on the OSU-WRF hinged wavemaker are derived in the following section.

DYNAMIC EQUATIONS

The dynamic equation for the conservation of horizontal momentum for small amplitude oscillations of the wavemaker piston section with water in the wave flume shown in Fig. 4 may be approximated by (compare to Ref. 7):

in which the dot denotes temporal differentiation of the wavemaker piston displacement, S(t); m = mass of the piston; $\mu = viscous$ resistance of the piston [Timoshenko and Young (10)]; $P_w(t) = hydraulic$ oil pressure force of the piston with water in the wave flume; and N(t) and R(t) = h dynamic nitrogen and connecting rod reaction forces, respectively. The dynamic equation for the conservation of angular momentum for small amplitude motions of the hinged wavemaker section with water in the wave flume shown in Fig. 4 may be approximated by

in which I= moment of inertia of the hinged wavemaker about the hinge; $\nu=$ viscous resistance of wavemaker flap; M(t)= the hydrodynamic wave pressure moment on the hinged wavemaker; and H= moment arm of the connecting rod reaction force. For small amplitude motions of the piston, the angular displacement of the wavemaker may be approximated by

in which a positive horizontal displacement of the piston induces a negative angular rotation of the hinged wavemaker in the right-handed Cartesian coordinate

TABLE 1.—Summary of FFT Coefficient Ratios, γ_j , and Measured Phase Angles for Depth at Wavemaker, $h=3.96~\mathrm{m}$

Ω (1)	γs, stroke (water) (2)	pressure (water) (3)	γs stroke (drained) (4)	pressure (drained) (5)	β _ρ , in degrees (6)	β_d , in degrees (7)	S _m /S _T (water) (8)	β _M , in degrees (9)
0.075	100.0	98.0	100.0	89.3	66.5	138.2	1.01	-12.4
0.094	100.0	97.9	100.0	77.2	71.9	141.0	0.99	-15.5
0.107	100.0	97.8	100.0	85.9	67.4	139.9	0.97	-15.7
0.126	99.9	97.3	100.0	84.2	69.9	137.8	0.97	-14.6
0.138	100.0	97.6	100.0	82.3	69.5	137.7	1.00	-14.8
0.157	99.9	97.6	100.0	80.3	74.7	136.0	1.02	-18.2
0.170	99.9	97.2	100.0	79.5	77.0	134.3	0.99	-20.3
0.189	99.9	97.0	100.0	78.6	77.6	133.3	0.94	-20.0
0.220	99.9	95.9	100.0	77.4	76.3	133.4	1.00	-17.8
0.251	99.9	96.4	100.0	75.1	82.9	132.7	0.98	-24.6
0.283	99.8	95.6	100.0	74.8	78.9	132.1	0.94	-19.7
0.314	99.8	95.2	100.0	74.1	86.2	130.2	1.02	-25.5
0.346	99.7	94.4	100.0	74.2	82.9	129.8	0.90	-24.3
0.377	99.7	93.8	100.0	52.7	83.5	127.0	1.03	-23.8
0.408	99.6	88.3	100.0	75.2	90.5	128.2	0.89	-29.9
0.440	99.6	88.3	99.9	73.8	86.2	127.9	0.98	-24.0
0.471	99.5	86.1	100.0	74.9	96.6	127.3	0.91	-33.2
0.503	99.4	84.8	99.9	75.3	89.3	124.6	0.96	-25.1
0.534	99.3	85.2	99.9	58.5	101.4	123.3	0.93	-36.2
0.566	99.1	87.7	99.9	61.3	92.5	124.2	0.88	-25.6
0.628	94.5	86.1	99.4	58.4	95.0	119.3	0.87	-26.5

system employed in the companion paper. For the experimental verification in the OSU-WRF, $S/2H \le 0.16$ and the approximation given by Eq. 10 will have a maximum error = 0.8%. Substituting Eq. 10 into Eq. 9 and equating connecting rod reaction forces, R(t), the coupled equations of motion with water in the wave flume reduce to

$$A\ddot{S} + B\dot{S} = P_w + N - \frac{M}{H} \qquad (11)$$

in which
$$A = m + \frac{I}{H^2}$$
 (12a)

$$B = \mu + \frac{\nu}{H^2} \qquad (12b)$$

Similarly, the coupled translational and rotational dynamic equations of motion with the wave flume drained may be expressed by

$$A\ddot{S} + B\dot{S} = P_d(t) \quad ... \quad (13)$$

in which P_d = hydraulic oil pressure of the piston with the wave flume drained.

TABLE 2.—Summary of FFT Coefficient Ratios, γ_{j} , and Measured Phase Angles for Depth at Wavemaker, $h=4.42~\mathrm{m}$

Ω (1)	γs stroke (water) (2)	Pressure (water) (3)	γs stroke (drained) (4)	γ _{Pd} pressure (drained) (5)	β _ρ , in degrees (6)	β _d , in degrees (7)	S _m /S _T (water) (8)	β _M , in degrees (9)
0.075	99.9	99.2	100.0	90.3	64.1	142.5	0.99	-10.9
0.094	100.0	98.6	100.0	88.3	70.8	140.5	1.02	-13.4
0.107	100.0	97.9	100.0	86.4	70.6	138.9	1.00	-15.6
0.126	99.9	98.9	100.0	84.2	74.5	137.4	0.97	-17.3
0.138	99.9	98.5	100.0	81.1	72.9	137.3	0.95	-16.3
0.157	99.9	98.8	100.0	80.2	72.3	135.6	0.96	-14.7
0.170	99.9	98.7	100.0	66.0	72.2	135.5	1.00	-15.2
0.189	99.9	98.6	100.0	77.5	77.4	134.2	1.02	-18.5
0.220	99.8	97.2	100.0	74.3	81.7	131.3	0.95	-21.8
0.251	99.7	98.4	100.0	72.3	75.5	131.1	0.96	-17.3
0.283	99.8	98.3	100.0	71.5	80.8	129.8	1.03	-22.5
0.314	99.3	97.8	100.0	72.1	81.2	129.1	0.90	-23.4
0.346	99.7	97.4	100.0	71.4	78.9	128.5	1.00	-20.2
0.377	99.4	89.2	100.0	69.7	86.6	127.3	0.97	-27.6
0.408	99.3	88.9	100.0	71.5	83.6	125.3	0.89	-23.3
0.440	99.4	96.4	99.9	48.2	86.5	127.1	1.02	-25.2
0.471	98.4	96.4	99.9	50.9	93.1	125.4	0.91	-29.0
0.503	99.2	95.2	100.0	72.7	87.2	123.5	0.97	-23.5
0.534	96.8	91.8	99.9	72.6	97.4	123.8	0.97	-30.8
0.566	97.8	86.1	99.8	70.0	92.8	121.2	0.88	-25.6
0.628	98.4	93.6	100.0	74.2	104.0	119.9	0.91	-33.2

Solving Eqs. 11 and 13 for the hydraulic oil pressure moment induced by the piston with water and with the wave flume drained yields

$$P_{w}(t) = \frac{M(t)}{H} - N(t) + A\ddot{S}(t) + B\dot{S}(t) \dots \dots \dots \dots \dots (14a)$$

For simple harmonic motions of the wavemaker piston, we may define the following sinusoids:

$$S(t) = \frac{S}{2} \exp i (\omega t + \alpha) \qquad (15a)$$

TABLE 3.—Relative Errors for Wavemaker Gain Function, $\epsilon_{\scriptscriptstyle G}$, for Dimensionless $h=3.96~{\rm m}$

					S/H	
Ω (1)	H/L (2)	H/H _B (3)	U (4)	Measured (5)	Theoretical (6)	ϵ_G , as a percentage (7)
0.075	0.021	0.236	6.25	1.75	1.70	-2.9
0.094	0.025	0.249	4.95	1.42	1.47	+3.4
0.107	0.027	0.253	4.24	1.25	1.35	+7.4
0.126	0.029	0.249	3.30	1.14	1.21	+5.0
0.138	0.027	0.228	2.63	1.20	1.14	-5.3
0.157	0.030	0.238	2.22	1.07	1.04	-2.9
0.170	0.031	0.238	1.94	0.99	0.98	-1.0
0.189	0.032	0.233	1.58	0.89	0.92	+3.3
0.220	0.034	0.238	1.20	0.83	0.82	-1.2
0.251	0.036	0.240	0.93	0.73	0.75	+2.7
0.283	0.036	0.237	0.70	0.66	0.69	+4.3
0.314	0.039	0.220	0.57	0.73	0.65	-12.3
0.346	0.040	0.241	0.45	0.55	0.62	+11.3
0.377	0.039	0.237	0.34	0.62	0.59	-5.1
0.408	0.038	0.231	0.27	0.52	0.57	+8.8
0.440	0.038	0.228	0.22	0.57	0.55	-3.6
0.471	0.038	0.230	0.18	0.51	0.53	+3.8
0.503	0.037	0.218	0.14	0.55	0.52	-5.8
0.534	0.040	0.234	0.13	0.49	0.51	+3.9
0.566	0.040	0.232	0.11	0.46	0.50	+8.0
0.628	0.038	0.227	0.08	0.45	0.49	+8.2

Note: $\epsilon = (\text{theoretical} - \text{measured})/\text{theoretical} \times 100\%$; and J = number of evanescent

$$P_d(t) = P_d \exp i (\omega t + \alpha_d) \quad ... \quad ... \quad ... \quad ... \quad ... \quad (15c)$$

$$N(t) = N \exp i (\omega t + \alpha_N) \qquad (15e)$$

in which only the real part of the complex phase vector is to be taken. Substituting Eq. 15c and temporal derivatives of Eq. 15a into Eq. 14b and equating real and imaginary parts, the magnitude of the coupled inertia and viscous resistance of the wavemaker system are given by the following:

$$A = -\frac{2P_d}{S\omega^2}\cos\beta_d \quad \quad (16a)$$

Hydrodynamic Moment, ϵ_{M} , and for Relative Phase Angle, ϵ_{g} , for Depth at Wavemaker,

J (14)	es	β_M , in degree		M'			
	ε _β , as a percentage (13)	Theoretical (12)	Mea- sured (11)	€ _M , as a percentage (10)	Theoretical (9)	Mea- sured (8)	
4	+0.6	86.3	85.8	-7.0	0.4077	0.4363	
4	+2.2	86.3	84.4	-2.2	0.3949	0.4036	
4	-0.5	86.4	86.8	+6.4	0.3864	0.3618	
4	-1.0	86.6	87.4	-0.9	0.3737	0.3769	
4	-1.7	86.8	88.2	+2.5	0.3653	0.3563	
5	-2.1	87.1	88.9	+0.4	0.3527	0.3513	
5	+1.6	87.4	86.0	+5.6	0.3445	0.3251	
5	+0.5	87.8	87.4	+0.2	0.3322	0.3315	
3	+1.0	88.5	87.6	+2.3	0.3123	0.3051	
3	+4.1	89.0	85.3	-0.6	0.2932	0.2949	
5	+1.9	89.2	87.6	+4.4	0.2753	0.2633	
5	+5.4	89.1	84.3	+4.6	0.2586	0.2469	
5	-1.2	88.6	89.7	+0.8	0.2434	0.2414	
5	-2.5	87.5	89.7	-1.3	0.2296	0.2327	
5	+4.4	86.0	82.2	-8.1	0.2180	0.2358	
5	-6.1	84.0	89.1	-8.1	0.2071	0.2238	
5	+7.7	81.5	75.3	-14.7	0.1978	0.2269	
5	-11.9	78.6	88.0	-15.1	0.1905	0.2193	
5	+10.4	75.4	67.6	-13.6	0.1842	0.2092	
5	-19.3	71.8	85.7	-14.5	0.1795	0.2054	
5	-27.8	64.0	81.9	-19.5	0.1746	0.2087	

required for 0.1% accuracy.

in which the drained phase angle $\beta_d = \alpha_d - \alpha$ must be a second quadrant phase angle for positive semidefinite values of the system inertia and viscous resistance [cf. Webster (12) for a review of the phase lag for a damped harmonic oscillator with negligible stiffness compared to inertia].

Substituting Eqs. 14b, 15b, 15d, and 15e into Eq. 14a and equating real and imaginary parts yields the following expressions for the magnitude of the hydrodynamic pressure moment on the hinged wavemaker:

$$M = H \{P_w^2 + P_d^2 + N^2 - 2 P_d P_w \cos(\beta_d - \beta_w) + 2 N [P_w \cos(\beta_w - \beta_N) - P_d \cos(\beta_d - \beta_N)]\}^{1/2} \dots (17a)$$

and for the relative phase angle for the hydrodynamic pressure moment:

$$\beta_{M} = \arctan \left\{ \frac{P_{w} \sin \beta_{w} - P_{d} \sin \beta_{d} + N \sin \beta_{N}}{P_{w} \cos \beta_{w} - P_{d} \cos \beta_{d} + N \cos \beta_{N}} \right\} \dots \dots \dots (17b)$$

in which $\beta_w = \alpha_w - \alpha$; and $\beta_N = \alpha_N - \alpha$.

TABLE 4.—Relative Errors for Wavemaker Gain Function, $\epsilon_{_{G}}$, for Dimensionless $h=4.42~\mathrm{m}$

					S/H	
Ω (1)	H/L (2)	H/H _B (3)	U (4)	Measured (5)	Theoretical (6)	ϵ_G , as a percentage (7)
0.075	0.023	0.257	6.76	1.44	1.50	4.0
0.094	0.024	0.244	4.85	1.35	1.35	0.0
0.107	0.025	0.233	3.91	1.29	1.24	-4.0
0.126	0.028	0.246	3.26	1.05	1.11	5.4
0.138	0.030	0.256	2.92	0.92	1.04	1.5
0.157	0.031	0.243	2.27	0.91	0.95	4.2
0.170	0.031	0.240	1.97	0.90	0.90	0.0
0.188	0.031	0.228	1.55	0.90	0.84	-7.1
0.220	0.035	0.242	1.22	0.70	0.75	6.7
0.251	0.035	0.234	0.90	0.67	0.68	1.5
0.283	0.037	0.242	0.71	0.64	0.63	-1.6
0.314	0.038	0.242	0.56	0.53	0.59	10.2
0.346	0.037	0.231	0.42	0.58	0.56	-3.6
0.377	0.038	0.234	0.34	0.53	0.53	0.0
0.408	0.040	0.242	0.28	0.45	0.51	11.8
0.440	0.039	0.231	0.22	0.52	0.50	-4.0
0.471	0.036	0.218	0.17	0.48	0.48	0.0
0.503	0.038	0.230	0.15	0.47	0.47	0.0
0.534	0.039	0.233	0.13	0.46	0.46	0.0
0.565	0.037	0.220	0.10	0.43	0.45	4.4
0.628	0.037	0.219	0.07	0.43	0.44	2.3

Note: $\epsilon = (\text{theoretical} - \text{measured})/\text{theoretical} \times 100\%$; and J = number of evanescent

In the OSU-WRF, the time varying signals from the hydraulic oil piston pressures, $P_w(t)$ and $P_d(t)$, along with the wavemaker piston displacement, S(t), were recorded and were Fourier analyzed by an FFT algorithm to compute the magnitudes and phases for these two signals which are required in Eqs. 17(a) and 17(b). The time dependent nitrogen gas pressure term, N(t), was not recorded directly but had to be estimated from the measured piston displacement as described in the following.

The nitrogen gas system in the MTS designed OSU-WRF is used to backpressure the wavemaker piston in order to compensate for the static column of fluid on the wave flume side of the hinged wavemaker (vide Fig. 4). The time varying nitrogen gas pressure is a result of the small volume changes induced by the wavemaker piston stroke. The nitrogen gas pressure on the wavemaker piston may, therefore, be approximated by a static plus a time varying component according to the real gas equation:

$$N = N_s + \tilde{N}(t) = \frac{nZRTA_N}{V_N + A_NS(t)}$$
 (18)

in which n = mass of the nitrogen gas; Z = the compressibility coefficient for a real gas; R = gas constant for nitrogen; T = temperature; V_N = static

Hydrodynamic Moment, ϵ_M , and for Relative Phase Angle, ϵ_B , for Depth at Wavemaker,

J (14)	es	β_M , in degree	110		M'	
	ε _β , as a percentage (13)	Theoretical (12)	Mea- sured (11)	€ _M , as a percentage (10)	Theoretical (9)	Mea- sured (8)
4	+2.7	86.3	84.0	-1.8	0.4116	0.4191
4	+11.3	86.3	76.6	-2.0	0.3987	0.4067
4	+6.4	86.4	80.8	-7.9	0.3902	0.4212
4	+5.9	86.6	81.5	-5.4	0.3774	0.3976
4	+4.0	86.7	83.3	+8.8	0.3690	0.3364
4	+0.1	87.1	87.0	-0.3	0.3565	0.3576
5	+2.0	87.3	85.6	+3.6	0.3482	0.3356
5 3 3	+7.2	87.7	81.4	-9.6	0.3360	0.3682
3	+10.2	88.4	79.4	+0.8	0.3162	0.3138
3	+1.0	88.9	88.0	+0.2	0.2973	0.2967
	+9.2	89.2	81.0	-0.3	0.2795	0.2804
3 5 5	+4.0	89.2	85.7	+1.3	0.2629	0.2596
5	+3.0	88.8	86.1	-1.8	0.2477	0.2522
5	+11.0	87.9	78.3	-5.0	0.2340	0.2458
5 5	+2.4	86.6	84.6	+3.9	0.2224	0.2138
5	+8.0	84.9	78.1	-3.4	0.2112	0.2183
5	+11.1	82.6	73.5	-14.3	0.2016	0.2303
5	+1.4	80.0	78.9	-1.3	0.1939	0.1965
5	+14.9	77.0	65.5	-7.2	0.1871	0.2005
5	-0.5	73.6	74.1	-7.1	0.1818	0.1947
5	+14.4	66.3	56.8	-12.9	0.1756	0.1982

terms required for 0.1% accuracy.

volume of nitrogen gas; and A_N = surface area of the terminal end of the wavemaker ram normal to the wavemaker stroke (which is not equal to the hydraulic oil piston surface area).

For the experimental verifications in the OSU-WRF, the ratio of $A_NS(t)/V_N \le 0.16$; and we may expand Eq. 18 by the binomial theorem to obtain, approximately

$$N_s + N(t) = \frac{nZRTA_N}{V_N} \left[1 - \frac{A_N S(t)}{V_N} + 0 \left(\frac{A_N S(t)}{V_N} \right)^2 \right](19)$$

in which the static component exactly balances the hydrostatic moment on the wavemaker and the dynamic component acts like a stiffness element in opposing positive displacements of the piston. The difficulty in recording the dynamic nitrogen pressure force directly may be seen from the ratio of the dynamic to static component; i.e.:

$$\frac{|N(t)|}{N_x} = \frac{A_N S}{V_N} \le 0.16 \dots (20)$$

Pressure instrumentation with adequate resolution for dynamic pressures which

are very much less than 16% of the static component are difficult to obtain economically. Consequently, the experimental verifications were analyzed by replacing the exact dynamic nitrogen gas terms in Eqs. 17(a) and 17(b) with an equivalent linear spring element approximated by

$$N(t) = -KS(t) \qquad (21)$$

in which the equivalent spring constant, K, is determined by a static moment balance between the hydrostatic pressure moment on the wavemaker and the static nitrogen gas pressure according to

$$K = nZRT \left(\frac{A_N}{V_N}\right)^2 \qquad (22a)$$

in which B = width of the hinged wavemaker. Substituting Eq. 21 into Eqs.

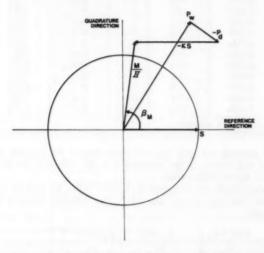


FIG. 5.—Booker (1) Phase Vector Diagram for Dynamic Oscillations of OSU-WRF Hinged Wavemaker System

17(a) and 17(b) and evaluating the equivalent nitrogen gas spring constant, K, from the static water depth in the wave flume according to Eq. 22b, the following relationships for the magnitude and phase angle, respectively, for the wavemaker hydrodynamic pressure moment are obtained:

$$M = H \left\{ P_w^2 + P_d^2 + \left(K \frac{S}{2} \right)^2 - 2 P_w P_d \cos (\beta_d - \beta_w) - KS \left[P_w \cos \beta_w \right] \right\}$$

$$-P_d \cos \beta_d \bigg]^{1/2} \qquad (23a)$$

$$\beta_{M} = \arctan \left\{ \frac{P_{w} \sin \beta_{w} - P_{d} \sin \beta_{d}}{P_{w} \cos \beta_{w} - P_{d} \cos \beta_{d} - K \frac{S}{2}} \right\}$$
 (23b)

since $\beta_N = \alpha_N - \alpha = \alpha - \alpha = 0$.

EXPERIMENTAL RESULTS

Experimental measures for the wavemaker gain function, S/H; magnitude of the dimensionless hydrodynamic pressure moment, M'; and relative phase angle, β_M , were obtained for 21 values of relative wave frequency for each

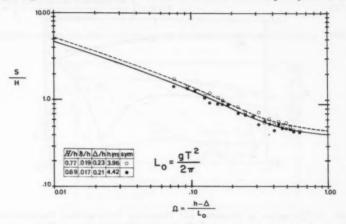


FIG. 6.—Comparison of Measured Wavemaker Gain Function, \mathbf{S}_m/H , with Theoretical Wavemaker Gain Function, \mathbf{S}_T/H , for Depths at Wavemaker, h=3.96 m and = 4.42 m

of two different water depths which cover one decade of relative water depth, $(h-\Delta)/L_o$. Tables 1 and 2 summarize the dimensionless FFT coefficient ratios, γ_f , computed from Eq. 6 for the experimental data recorded in the two water depths. These dimensionless FFT coefficient ratios indicate that the data measured for the wavemaker stroke with water (Tables 1 and 2, Cols. 2) and with the wave flume drained (Tables 1 and 2, Cols. 4) are very well represented by a single linear sinusoid with an amplitude given by the magnitude of the FFT coefficient for the fourth harmonic. The hydraulic oil piston pressure force ratio with water in the wave flume which are summarized in Tables 1 and 2, Cols. 3, are also well explained by the magnitude of the FFT coefficient for the fourth harmonic except for dimensionless relative frequencies, Ω , greater than 0.314 which are deep-water wave conditions. On the other hand, the

magnitudes for the hydraulic oil piston pressure force with the wave flume drained which are summarized in Tables 1 and 2, Cols. 5, are not as well correlated with the magnitudes of the FFT coefficients for the fourth harmonic and this lower correlation continues to decrease with increasing relative wave frequency, Ω . This explains why the relative phase angles with the wave flume drained, β_d , tabulated in Tables 1 and 2, Cols. 7, rotate toward 90° instead of 180° with increasing values of dimensionless wave frequency, Ω , as would be expected from an inertially dominated dynamic system with linear viscous resistance [compare to Timoshenko and Young (10) or Webster (12)]. The reasons for this counter rotation may be observed from the hydraulic oil piston pressure signal, P_w , shown on the sample analog trace in Fig. 3. The high frequency oscillation which may be seen superimposed on the fundamental hydraulic oil pressure signal is a result of the feedback control system and its amplitude is a greater percentage of the fundamental amplitude for, P_d , than it is for

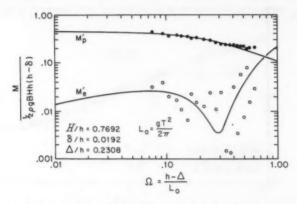


FIG. 7.—Comparison of Measured and Theoretical Dimensionless Hydrodynamic Wavemaker Amplitudes, M_{ρ}' and M_{r}' , for Depth at Wavemaker, h=3.96 m

 $P_{\rm w}$. This high frequency error in the drained piston oil pressure force precludes an accurate estimate of the system inertia and viscous resistance via Eqs. 16(a) and 16(b); however, it does permit an approximate evaluation of the hydrodynamic pressure moment on the wavemaker.

Cols. 8 and 9 of Tables 1 and 2 summarize the magnitudes of the wavemaker relative gain function, S_m/S_T , and relative phase angles, β_S , which were computed by correlating the measured wavemaker stroke from the LVDT signal, S_m , with the theoretical wavemaker stroke synthesized from the minicomputer FFT algorithm, S_T . The increase in the magnitude of the phase lag of the measured wavemaker stroke behind the theoretical wavemaker stroke and the decrease in the magnitude ratio may be observed from Tables 1 and 2, Cols. 9 and 8 to depend upon the dimensionless relative wave frequency, Ω .

Tables 3 and 4 summarize the dimensionless magnitudes and relative phase angles for the hydrodynamic pressure moments measured on the OSU-WRF

hinged wavemaker which were computed from the measured FFT coefficients by Eqs. 23(a) and (b). Relative measures of the degree of nonlinearities in the measured wave data are provided by: (1) The relative wave steepness values, H/L, tabulated in Col. 2 using the measured wave height and linear wave theory estimates for the wave length; (2) the ratio of measured wave height, H, to the theoretical breaking wave height, H_B , tabulated in Col. 3; and (3) the Ursell parameter, U [Ursell (11)], tabulated in Col. 4, which may be computed from the following ratios:

$$U = \left(\frac{H}{2L}\right) \left(\frac{L}{h}\right)^3 \qquad (24)$$

Dimensionless relative errors are tabulated for each of the three dimensionless wavemaker variables measured from

$$\epsilon_j = \left(\frac{\text{theoretical} - \text{measured}}{\text{theoretical}}\right) \times 100\% \dots (25)$$

Negative values for these relative errors indicate an underprediction by linear

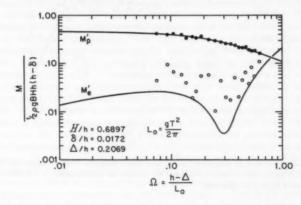


FIG. 8.—Comparison of Measured and Theoretical Dimensionless Hydrodynamic Wavemaker Amplitudes, M_{ρ}' and M_{c}' , for Depth at Wavemaker, h=4.42 m

wave theory derived in the companion paper while positive values of relative errors indicate overprediction by linear wave theory. Col. 14 lists the number of evanescent eigenmode terms required in the infinite summation in order to obtain an accuracy of 0.1%.

Fig. 5 is a schematic Booker phase vector diagram (1) for a typical set of dynamic oscillation signals recorded for the OSU-WRF hinged wavemaker system. This type of diagram is quite powerful for quickly checking the relative accuracy of approximate analytical dynamic structural models. An a priori analyses of the measured data in the OSU-WRF assumed that the ratio of the magnitude of the dynamic nitrogen gas pressure force to the magnitude of the drained

piston oil pressure force, N/P_d , would be negligible and was omitted from initial computations. A quick series of Booker phase vector diagrams using the FFT magnitude and phases for P_w and P_d quickly demonstrated that the magnitudes of the resultant hydrodynamic moment vector were consistently much larger than values estimated by linear wave theory and that the relative phase angles were consistently much smaller than values predicted by linear wave theory (vide Fig. 5 and omit the phase vector—KS). It was readily visualized as a result of the Booker phase vector diagrams that the vector addition of a dynamic phase vector which was in-phase with the inertia of the wavemaker system (i.e., in the negative reference direction in Fig. 5) would yield a resultant phase vector for the hydrodynamic pressure moment with approximate magnitude and phase values closer to those predicted by linear wave theory. The equivalent linear spring model for the dynamic nitrogen gas pressure force was then reintroduced into the analyses and a posterior check of the ratio KS/ P_d verified

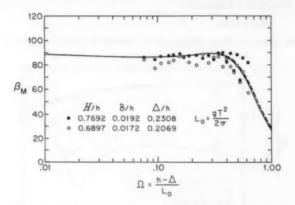


FIG. 9.—Comparison of Measured and Theoretical Relative Phase Angles for Wave-maker Hydrodynamic Pressure Moment for Depths at Wavemaker, h=3.96 m (——Solid) and 4.42 m (---- Dashed)

that the ratio could not be neglected in the analyses. The Booker phase vector diagram was quite powerful for rapidly analyzing multiple oscillatory signals and for evaluating approximate analytical dynamic structural models.

Fig. 6 compares the measured wavemaker gain function values, S_m/H , with the theoretical values computed in the companion paper. The absolute values of the maximum relative errors are less than 12.5% for the 42 data values measured. These values for the relative errors for the dimensionless wavemaker gain function are consistent with values previously reported by others for hinged wavemakers.

Figs. 7 and 8 compare measured and theoretical values for the magnitudes of the dimensionless wavemaker pressure moment for the propagating mode which were computed from

$$M_p' = M' \sin \beta_M \quad \quad (26a)$$

and for the evanescent mode which were computed from

 $M'_{\epsilon} = M' \cos \beta_M \dots (26b)$

The absolute value for the maximum relative error, ϵ_M , is approx 20% (Table 3, Col. 10). The magnitudes of the relative errors for the dimensionless hydrodynamic pressure moment on the hinged wavemaker increase with increasing relative wave frequency, Ω . These measured magnitudes of wave pressure moment on a hinged wavemaker appear to be unique.

Fig. 9 graphically compares the measured and theoretical relative phase angles, β_M , for the hydrodynamic pressure moment on the hinged wavemaker. The magnitudes of the relative errors for the hydrodynamic moment phase angle, β_M are less than 28% (Table 3, Col. 13) and, again, increase in magnitude with increasing relative wave frequency, Ω .

CONCLUSIONS

The dimensionless design curves for hinged wavemakers of variable draft for wave flumes which consist of two constant depth domains separated by a gradually sloping transition region are compared with unique experimental data recorded in the OSU-WRF in each of two water depths for 21 values of dimensionless wave frequency and relative wave heights which are approx 25% of the theoretical breaking limit. The magnitude and phase angle of the hydrodynamic pressure moment on the wavemaker were estimated from the coupled translational and rotational dynamic equations of motion by FFT coefficients which were computed from the wavemaker stroke and from the measured hydraulic oil piston pressure force with water and with the wave flume drained. The FFT coefficients for the fourth harmonic demonstrated good correlation for a linear process except for the drained wave flume condition in which a high frequency component in the piston pressure force which was induced by the feedback control system diminished the percent contribution by the fundamental periodic component to the total energy content of the amplitude spectrum. The dynamic component of the nitrogen gas pressure force was approximated by an equivalent linear spring in which the linear spring constant was evaluated from the real gas equation and a static moment balance between the nitrogen gas backpressure and the static column of fluid in the wave flume. The Booker phase vector diagram (1) proved to be quite powerful for rapidly comparing measured FFT phase vectors of oscillatory signals with approximate analytical dynamic structural models in posterior analyses.

While measured data for the dimensionless wavemaker gain function, S/H, have been previously published, the comparisons with the magnitude and phase angle of the hydrodynamic pressure moment appear to be unique.

ACKNOWLEDGMENTS

We are grateful for the financial support provided by the National Science Foundation Grant No. ENG75-10496 and by the Oregon State University Sea Grant College Program, National Oceanic and Atmospheric Administration Office of Sea Grant, Department of Commerce, under Grant No. 04-6-158-44004.

We also wish to express our appreciation to the following colleagues: J. H.

Nath, who suggested the use of the large-scale hinged wavemaker in the OSU-WRF to verify the Havelock wavemaker theory for the hydrodynamic pressure moments and who patiently reviewed several iterations of our dynamic analyses of the OSU-WRF hinged wavemaker system; C. K. Sollitt, who has developed a wealth of calibration background for the OSU-WRF through his research; and T. Dibble and D. Standley who carefully and skillfully recorded and evaluated the experimental data.

APPENDIX 1.—REFERENCES

- Booker, H. G., A Vector Approach to Oscillations, Academic Press, New York, N.Y., 1965, pp. 91-118.
- Clough, R. W., and Penzien, J., Dynamics of Structures, McGraw-Hill Book Co., New York, N.Y., 1975, pp. 113-116.
- Dean, R. G., "Evaluation and Development of Water Wave Theories for Engineering Application," Special Report No. 1, Vol. I, U.S. Army Corps of Engineers, Coastal Engineering Research Center, Fort Belvior, Va., Nov., 1974, p. 39.
- Gilbert, G., Thompson, D. M., and Brewer, A. J., "Design Curves for Regular and Random Wave Generators," *Journal of Hydraulic Research*, Vol. 9, No. 2, 1971, pp. 163-196.
- Hudspeth, R. T., and Borgman, L. E., "Efficient FFT Simulation of Digital Time Sequences," *Journal Engineering Mechanics Division*, ASCE, Vol. 105, No. EM2, Proc. Paper 14517, Apr., 1979, pp. 223-235.
- Hudspeth, R. T., and Chen, M. C., "Design Curves for Hinged Wavemaker: I— Theory," Journal of the Hydraulics Division, ASCE, Vol. 107, No. HY5, Proc. Paper 16236, May, 1981, pp. 533-552.
- Hudspeth, R. T., and Leonard, J. W., "Dynamic Covariance Equations for Hinged Wavemakers," Engineering Structures, Vol. 2, Oct., 1980, pp. 217-224.
- Hyun, J. M., "Theory for Hinged Wavemakers of Finite Draft in Water of Constant Depth," Journal of Hydronautics, Vol. 10, No. 1, Jan., 1976, pp. 2-7.
- Sollitt, C. K., and Huber, D. S., "Large Scale Model Testing of a Submerged Wave Attenuation Device," Closed Loop, Vol. 6, No. 1, Apr., 1976, pp. 13-26.
- Timoshenko, S., and Young, D. H., Advanced Dynamics, McGraw-Hill Book Co., New York, N.Y., 1948, pp. 24-61.
- Ursell, F., "The Long-Wave Paradox in Theory of Gravity Waves," Proceedings of the Cambridge Philosophical Society, Vol. 49, 1953, pp. 685-694.
- Webster, A. G., The Dynamics of Particles and of Rigid, Elastic, and Fluid Bodies, 2nd ed., Dover Publications, Inc., New York, N.Y., 1959, pp. 152-157.

APPENDIX II.—NOTATION

The following symbols are used in this paper:

- A = coupled masses of piston and wavemaker;
- $A_N = \text{surface area of nitrogen piston};$
 - B = total width of wavemaker;
 - B = coupled mechanical damping of piston and wavemaker;
 - g = gravitational constant;
 - H = deterministic wave height;
 - h = still water depth at wavemaker;
- I = moment of inertia of hinged wavemaker about hinge;
- $i = \sqrt{-1} = \text{imaginary unit};$
 - J = total number of evanescent eigenmodes required to

obtain 1% accuracy in infinite summations;

 $K = -iK_1$ = wave number for propagating eigenmode in constant depth domain, h, adjacent to wavemaker;

 K_n = wave number for evanescent eigenmodes $(n \ge 2)$;

L = linear theory wave length; $L = gT^2/2\pi = \text{deep water wave length;}$

l = moment arm to hydrodynamic pressure force;

M'(M') = time dependent (amplitude) dimensionless total hydrodynamic moment on the wavemaker;

m = mass of hydraulic piston which oscillates hinged wavemaker:

m₀ = zeroeth spectral moment (= variance of time sequence);

N(N) = time dependent (amplitude) nitrogen gas pressure force:

n = mass of nitrogen gas;

n, m = summation indices;

 P_d , (P_d) = time dependent (amplitude) hydraulic oil piston pressure force with wave flume drained;

 P_{w} , (P_{w}) = time dependent (amplitude) hydraulic oil piston pressure force with water in wave flume;

R = time dependent connecting rod reaction force;

R = gas constant;

S,(S) = time dependent (double amplitude) displacement of wavemaker stroke measured at height of wavemaker piston;

T = wave period;

T = temperature of nitrogen gas;

t = time;

U = complex-valued discrete time sequence;

 $U = (H/2L)(L/h)^3$ = Ursell parameter;

 V_N = volume of nitrogen gas required to back-pressure piston;

W =integer number of values in discrete time sequence;

X = complex-valued FFT coefficient;

x = horizontal coordinate axis with origin located at undisturbed water level at wavemaker;

y = vertical coordinate axis with origin located at still water level at wavemaker;

Z = compressibility coefficient for real gas;

 α_j = arbitrary initial phase angle for wavemaker variable, j;

 β_j = relative phase angle measured between wavemaker variable, j, and displacement of wavemaker;

γ_j = ratio of twice square modulus of FFT coefficient for fourth harmonic for wavemaker variable, j, to total energy content of amplitude spectrum;

Δ = vertical rise in depth between two constant depth wave flume domains;

- Δf = equal discrete intervals of frequency used in FFT digitizing process;
- Δt = equal discrete intervals of time used in FFT digitizing process;
 - = height of wavemaker hinge measured above bottom;

(theoreticalmeasured/

theoretical)
× 100% = dimensionless relative error;

- H = height of wavemaker piston measured vertically above wavemaker hinge:
- η = instantaneous water surface elevation measured positive upwards from undisturbed still water level;
- θ = angular rotation of wavemaker about hinge;
- K = equivalent spring stiffness for dynamic nitrogen gas force;
- $\kappa =$ wave number for propagating eigenmode in constant depth test domain, $h \Delta$;
- μ = viscous resistance of piston;
- ν = viscous resistance of wavemaker;
- ρ = fluid density;
- $\Omega = (h \Delta)/L_o$ = relative water depth; and ω = radial frequency (= $2\pi/T$).

Superscripts

- = dimensionless variables; and
 - = temporal derivative.

Subscripts

- B = theoretical breaking wave height:
- d = with wave flume drained:
- $e = \text{evanescent eigenmode } (n \ge 2);$
- G =wavemaker gain function;
- M = hydrodynamic pressure moment;
- m = measured value;
- N = nitrogen gas pressure force;
 - o = deep water wave conditions;
- p(n = 1) = propagating eigenmode;
 - S = wavemaker stroke;
 - T = theoretical wavemaker stroke (discrete time sequence synthesized by minicomputer algorithm); and
 - w = with water in wave flume.

NUMERICAL ANALYSIS OF FLOW IN SEDIMENTATION BASINS

By David R. Schamber, A. M. ASCE and Bruce E. Larock, M. ASCE

INTRODUCTION

Primary sedimentation by gravity in large basins and tanks has been an integral part of most major water and sewage treatment plants for many decades. Current understanding of the process is incomplete, however, and is impeded primarily by a lack of detailed knowledge of the velocity field in the basin. In partial response to this situation, this article describes a numerical model which predicts the velocity field in sedimentation basins. Since the flow is turbulent within these tanks, determination of the velocity field is difficult. The point velocities within the basin are determined by the finite element solution of five coupled, nonlinear partial differential equations. The structure of the turbulence is represented by an effective or "eddy" viscosity model which depends on the turbulent kinetic energy and its rate of dissipation. Once the velocity field is determined, the distribution of particle concentration throughout the basin could then be obtained by solution of a linear convection-diffusion equation.

BACKGROUND

Since primary sedimentation by gravity often precedes other unit operations, the performance of all processes could potentially be influenced by the efficiency of the settling basin. The writers view the design of basins for increased particle removal efficiency as primarily a fluid mechanics problem since the basin velocity field strongly influences the path taken by particles entering the tank. The ability to test basin performance for various tank geometries, different inlet and outlet structures, and various loading conditions and thermal regimes is essential for determining optimal design criteria. Determining flow patterns in basins is the key to evaluating this performance. Flow patterns may be generated by experimental model studies, both direct field measurement and full-scale experimental studies, or mathematical computer modeling. Experimental studies, while useful, are expensive and relatively inflexible when the goal is to examine a variety of tank geometries and various inlet and outlet structures. Direct field measure-

Asst. Prof., Civ. Engrg. Dept., Univ. of Utah, Salt Lake City, Utah 84112.

²Prof., Civ. Engrg. Dept., Univ. of California, Davis, Calif.

Note.—Discussion open until October 1, 1981. To extend the closing date one month, a written request must be filed with the Manager of Technical and Professional Publications, ASCE. Manuscript was submitted for review for possible publication on July 8, 1980. This paper is part of the Journal of the Hydraulics Division, Proceedings of the American Society of Civil Engineers, ©ASCE, Vol. 107, No. HY5, May, 1981. ISSN 0044-796X/81/0005-0575/\$01.00.

ment is useful for calibration and checking of computer models but by its very nature is not predictive. Therefore the writers direct their efforts toward numerical solutions of the equations governing the flow in settling basins as the most

productive long-term alternative.

The large scale of most tanks [typical vertical and horizontal dimensions of 10 ft (3 m) and 100 ft (30 m) respectively], together with the small kinematic viscosity of water [$\nu \simeq .00001$ sq ft/sec (.0000009 m²/s)], render the flow turbulent even though the velocities are in the range of 1 ft/min-10 ft/min (0.3 m/min-3.0 m/min). With these characteristic values the tank Reynolds number (depth × velocity/ ν) ranges from 17,000-170,000. These values agree well with values computed by Larsen (14) from experimental measurements in secondary clarifiers. Larsen also found turbulence intensities to range from 10%-20% (relative to the maximum mean value of velocities in the bottom current) throughout the basin, although even higher values were found in the inlet zone.

The general circulation pattern in rectangular and circular primary sedimentation basins, including the effects of surface wind, variable influent temperature, solar heating, and unsteady loading conditions, is time variant (unsteady) and three dimensional. The cost of a transient three-dimensional computation is currently prohibitively expensive in terms of computer execution time and storage. However, Montens (20) has shown by direct measurement on full-scale circular basins that the flow is very nearly radial in the absence of surface wind. In rectangular basins the flow remains three-dimensional due to corner and side effects; however, the flow in a vertical plane taken on the tank center line from inlet to outlet may reasonably be expected to be nearly two dimensional in the absence of wind stresses.

Thermal effects may induce density differences within the tank and cause the flow pattern to stratify. Although the inclusion of temperature effects into the computational algorithm appears relatively straightforward, it also increases by at least three the number of partial differential equations which must be solved (24). The proposed model is therefore limited in application to those operating conditions where the influent stream and fluid temperature within the tank are nearly equivalent.

The sediment concentration in the influent is assumed not to affect the fluid density because its magnitude is typically .0002 by weight (19). Presumably, this assumption would be invalid for certain basin operating conditions. The flow pattern established by an influent stream with little fluid inertia (corresponding to low loading rates) would be influenced by small concentration differences. An inlet stream with density greater than that of the fluid within the basin would plunge to the basin floor. By contrast, an inlet jet of lighter density would move as a layer over the top of the tank. Low inflow velocities would also produce weak turbulence and the high turbulence model (applicable for high loading rates) adopted for this study must then be modified appropriately (11). The proposed model is therefore restricted to those flow conditions which allow the hydrodynamic model to be uncoupled from the transport equation for particle concentration and the thermal energy equation. Primary sedimentation by gravity of a dilute suspension of discrete particles should adequately be represented by such a hydrodynamic model. However, the proper analysis of secondary clarifier performance, where density differences are significant, would

require the mathematical description of stratification caused by species concentration. Hamlin and Wahab (9) consider further the effects of temperature and concentration differences.

The scope of this paper is therefore limited to two-dimensional steady, nonstratified flow in the x-z (horizontal-vertical) or r-z (radial-vertical) plane.

MATHEMATICAL MODEL

The equations describing two-dimensional, steady, turbulent, nonstratified flow in a rectangular or circular sedimentation basin are (25):

$$\frac{\partial}{\partial r}(r^m U) + \frac{\partial}{\partial z}(r^m W) = 0 \qquad (1)$$

$$U\frac{\partial U}{\partial r} + W\frac{\partial U}{\partial z} - \frac{m}{r^m}(P + \overline{vv}) + \frac{\partial}{\partial r}(P + \overline{uu}) + \frac{\partial}{\partial z}(\overline{uw}) + \frac{1}{F_0^2}\frac{\partial h}{\partial r} = 0$$
 (2)

Equation 1 expresses conservation of mass, while Eqs. 2 and 3 express conservation of momentum in the horizontal/radial and vertical directions,

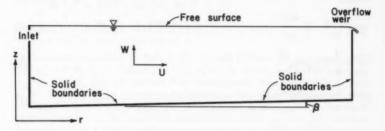


FIG. 1.—Schematic Tank Configuration

respectively. For m=1 these equations describe axisymmetric flow in the r-z plane, and for m=0 they describe planar flow in the x-z Cartesian plane. The coordinate r represents the x coordinate when m=0. Variables in Eqs. 1-3 have been nondimensionalized on a characteristic length h_0 and characteristic velocity U_0 , and $F_0^2 = U_0^2/(gh_0)$ is a representative Froude number with g=r ratio of weight to mass. The independent and dependent variables are defined with reference to Fig. 1 as follows (starred and characteristic variables are dimensional): $r^* = rh_0$ = horizontal coordinate; $z^* = zh_0$ = vertical coordinate; $U^* = UU_0$ = time-averaged mean horizontal or radial velocity; $W^* = WU_0$ = time-averaged mean vertical velocity; $u^*u^* = uu$ U_0^2 , $w^*w^* = ww$ U_0^2 , and $u^*w^* = uw$ U_0^2 are Reynolds stress terms. The overbar denotes time averaging, and u and w are instantaneous velocity fluctuations about their respective means. The nondimensional pressure $P = P^*/(\rho U_0^2)$ in which ρ = fluid density, is the deviation from the nondimensional hydrostatic pressure, i.e., the actual

pressure is given by $P + (h - z)/F_0^2$ in which $h = h^*/h_0$ is the free surface elevation. The viscous terms which normally appear in Eqs. 2 and 3 are omitted here because turbulent transport effectively swamps molecular transport. Inspection of Eqs. 1-3 reveals that the number of unknowns exceeds the number of equations—this is the familar closure problem associated with turbulent flows. Numerous closure models of varying complexity have been proposed in the literature (4,16,17). An outline of several models with finite element solutions to some one-dimensional flow examples is presented in Ref. 26.

The kinetic energy-dissipation or k- ϵ turbulence model which determines the variation of the turbulent eddy viscosity throughout the basin from the solution of two turbulence transport equations will be used to close the present mathematical model. This turbulence model has been tested and experimentally verified for a number of free-shear flows, boundary layer flows, internal flows, and flows with recirculation (15,17). More recently the model has been successfully used to model several complex recirculating flows (8,12,21). These computational results also compare favorably with available experimental data. It is therefore expected that the k- ϵ model will also perform adequately for sedimentation basin computations where several of these same flow features coexist.

By direct analogy to laminar flow, Boussinesq suggested that the turbulent stresses could be represented by expressions involving products of mean velocity gradients and the turbulent kinematic viscosity ν_i . This leads to the isotropic closure

$$\overline{uu} = \frac{2}{3} k - 2\nu_t \frac{\partial U}{\partial r} \qquad (4)$$

$$\overline{vv} = \frac{2}{3}k - 2mv_i \frac{U}{r} \qquad (5)$$

$$\overline{uw} = -\nu_t \left(\frac{\partial U}{\partial z} + \frac{\partial W}{\partial r} \right) \quad . \tag{7}$$

in which the turbulence kinetic energy $k = (1/2)(\overline{uu} + \overline{vv} + \overline{ww})$. Evidently v_i must be several orders of magnitude larger than the molecular kinematic viscosity v to conform to the observed ability of the turbulent motion to enhance momentum transport. Unlike the molecular viscosity, v_i is not a property of the fluid but varies from point to point within the flow field, reflecting the local structure of turbulence.

Computations of turbulent flow with ν_{ι} = constant (or known specified variation) have been relatively successful (13) when the magnitude of ν_{ι} is known a priori and have the practical advantage that no additional differential equations are required for this turbulence closure. Since the k- ϵ model computes the distribution of ν_{ι} from a simulated turbulent flow, one does not require a priori knowledge of the distribution of ν_{ι} . By dimensional considerations ν_{ι} is proportional to the kinetic energy of turbulence and its rate of dissipation ϵ in the following way:

Here $\epsilon = \nu(\overline{\partial u_i}/\partial x_j)(\overline{\partial u_i}/\partial x_j)$ is the isotropic dissipation rate. The variables k and ϵ are computed from transport equations (25) which have the following form in steady two-dimensional flow

$$U\frac{\partial k}{\partial r} + W\frac{\partial k}{\partial z} = \mathcal{P}_r - \epsilon + \mathcal{D}(k) \qquad (9)$$

$$U\frac{\partial \epsilon}{\partial r} + W\frac{\partial \epsilon}{\partial z} = c_{\epsilon 1} \frac{\epsilon}{k} \mathscr{P}_r - c_{\epsilon 2} \frac{\epsilon^2}{k} + \mathscr{D}(\epsilon) \qquad (10)$$

in which the production term P, is

$$\mathscr{P}_{r} = \nu_{t} \Phi$$
(11)

and
$$\Phi = 2\left(\frac{\partial U}{\partial r}\right)^2 + \left(\frac{\partial U}{\partial z} + \frac{\partial W}{\partial r}\right)^2 + 2\left(\frac{\partial W}{\partial z}\right)^2 + 2m\left(\frac{U}{r}\right)^2 \dots (12)$$

The diffusion of k and ϵ , respectively, are given by

The constants appearing in Eqs. 8, 10, 13, and 14 have the following values (17): $c_{\mu}=0.09,\ c_{\epsilon 1}=1.44,\ c_{\epsilon 2}=1.92,\ \sigma_{k}=1.0,\ \text{and}\ \sigma_{\epsilon}=1.3.$ The constants $c_{\epsilon 2},\ c_{\mu}$, and σ_{ϵ} may be inferred from experimental data (27), while $c_{\epsilon 1}$ and σ_{k} are determined by computer optimization, i.e., many calculations were performed in which the constant was systematically varied, and the value which gave the best overall agreement with experimental results was selected. Variables appearing in Eqs. 4–14 are nondimensional such that $k^*=kU_0^2$, $\epsilon^*=(\epsilon U_0^2)/(h_0)$, and $\nu_s^*=\nu_s$, U_0h_0 .

Equations 1-14 represent a closed system of five coupled, nonlinear partial differential equations. The five dependent variables are U, W, P, k, and ϵ while the independent variables are r and z. Pertinent boundary conditions are required to yield a unique solution. These conditions are described later.

FINITE ELEMENT SOLUTION OF MATHEMATICAL MODEL

Elliptic boundary value problems of the type presented herein are generally solved by finite difference or finite element techniques. Launder and Spalding (17) originally solved the k- ϵ model for a variety of flows by use of the Patankar-Spalding (22) finite difference algorithm which is basically a marching scheme applied to a parabolic equation set. More recently elliptic problems involving recirculation have also been solved with finite differences (12,21).

In the present work the equations are cast in integral form by the Galerkin method of weighted residuals and solved by the finite element method. This

approach was chosen because it allows one in principle to use a nonuniform computational mesh, to seek solutions in geometrically complex nonpolygonal domains, and to avoid difficulties in applying boundary conditions on such domain boundaries. An added advantage of this approach, as opposed to upwind or penalty function methods, is that the presence of suspicious oscillations in a solution appears to be a clear indicator that the computational mesh is locally too coarse and should be refined (7).

Expressions for the equation residuals f, written for an element e having domain Ω_e and a boundary Γ_e , are (25):

$$f_{P} = \int_{\Omega_{\epsilon}} M_{i} \left[\frac{\partial}{\partial r} (r^{m} U) + \frac{\partial}{\partial z} (r^{m} W) \right] d\Omega \qquad (15)$$

$$f_{U} = \int_{\Omega_{\epsilon}} N_{i} \left[r^{m} \left(U \frac{\partial U}{\partial r} + W \frac{\partial U}{\partial z} \right) - m(P + \overline{vv}) \right] d\Omega$$

$$- \int_{\Omega_{\epsilon}} r^{m} \left[(P + \overline{uu}) \frac{\partial N_{i}}{\partial r} + \overline{uw} \frac{\partial N_{i}}{\partial z} \right] d\Omega$$

$$+ \int_{\Gamma_{\epsilon}} r^{m} N_{i} \left[(P + \overline{uu}) I_{r} + \overline{uw} I_{z} \right] d\Gamma \qquad (16)$$

$$f_{W} = \int_{\Omega_{\epsilon}} r^{m} N_{i} \left(U \frac{\partial W}{\partial r} + W \frac{\partial W}{\partial z} \right) d\Omega - \int_{\Omega_{\epsilon}} r^{m} \left[\overline{uw} \frac{\partial N_{i}}{\partial r} \right] d\Gamma \qquad (17)$$

$$f_{k} = \int_{\Omega_{\epsilon}} r^{m} N_{i} \left(U \frac{\partial k}{\partial r} + W \frac{\partial k}{\partial z} - \mathcal{P}_{r} + \epsilon \right) d\Omega + \int_{\Omega_{\epsilon}} r^{m} \frac{v_{i}}{\sigma_{k}} \left(\frac{\partial k}{\partial r} \frac{\partial N_{i}}{\partial r} \right) d\Gamma \qquad (18)$$
and
$$f_{\epsilon} = \int_{\Omega_{\epsilon}} r^{m} N_{i} \left(U \frac{\partial \epsilon}{\partial r} + W \frac{\partial \epsilon}{\partial z} - c_{\epsilon 1} \frac{\epsilon}{k} \mathcal{P}_{r} + c_{\epsilon 2} \frac{\epsilon^{2}}{k} \right) d\Omega$$

$$+ \int_{\Omega_{\epsilon}} r^{m} \frac{v_{i}}{\sigma_{\epsilon}} \left(\frac{\partial \epsilon}{\partial r} \frac{\partial N_{i}}{\partial r} + \frac{\partial \epsilon}{\partial z} \frac{\partial N_{i}}{\partial z} \right) d\Omega \qquad (19)$$

in which the velocity correlations or Reynolds stresses are defined by Eqs. 4-7. The terms M_i and N_i are the appropriate basis functions for the dependent variables. All second derivative terms in the transport equations have been integrated once by parts so that C^0 elements may be used. The pressure term has also been integrated by parts to facilitate the application of normal-stress boundary conditions. The line integrals are evaluated only where Γ_e coincides with the global domain boundary Γ_i and I_e and I_e direction cosines of the

unit outer normal to Γ . The term $(\partial h/\partial r)$ in Eq. 2 is omitted in Eq. 16 because of use of the rigid lid approximation (mentioned with boundary conditions).

During the 1970s much attention has focused on the correct order of approximation for the primary variables appearing in the equations. Currently a linear variation M_i for pressure and a quadratic variation N_i for all other variables is assumed. While it is now becoming clear why the pressure must be approximated one order lower than the velocity components (23), the same cannot yet be said with surety for k and ϵ . Eight-node quadrilateral elements are used in this work with no known difficulties that can be traced to element choice.

NUMERICAL SOLUTION

The nonlinear equation set resulting from the finite element discretization process is solved by a variation of Newton's method. Experience with one-dimensional flow problems (26) indicates that a major difficulty in applying Newton's method is the proper initialization of the solution vector. Another difficulty is the sheer size of the equation set when the solution for all five variables (U, W, P, k, ϵ) is sought simultaneously.

To form the global equation set, one must appropriately sum the elemental contributions represented by Eqs. 15–19. The resulting set of nonlinear equations may be compactly written as

in which f = vector representing the system of equations; and x = vector of nodal unknowns for the system.

The basic Newton scheme solves the equation set by writing

in which n = iteration counter; A = Jacobian of equation matrix; and δx^n = set of incremental corrections to be made to the vector x^n . Solution of Equation 21 gives the following new estimate to the solution

$$\mathbf{x}^{n+1} = \mathbf{x}^n + \alpha \, \delta \mathbf{x}^n \quad \dots \quad \dots \quad \dots \quad \dots \quad \dots \quad \dots \quad (22)$$

in which $\alpha \leq 1 = a$ relaxation parameter.

In this work the mean flow equations (Eqs. 15-17) and the turbulence equations (Eqs. 18-19) are solved alternately rather than simultaneously. This method is easier to initialize and reduces core storage requirements substantially. However, more iterations are required to obtain a converged solution. To start, this approach requires a specified initial distribution of k and ϵ (constant values or simple linear variations of k and ϵ are generally used) which yield a reasonable distribution of ν , for the given problem. The mean flow equations are then solved by Newton's method with U, W, and P initialized with constant values. For example, P (which is the deviation from the hydrostatic pressure) may be set to zero. The U component may be assigned a value equal to the flow rate divided by the cross-sectional area, and the W component may be set to zero.

Having generated a solution to the UWP field, the algorithm now transfers to the solution of the global form of Eqs. 18 and 19. Use of a modified approach to Newton's method is required during initial iterations (25). Entries in the

Jacobian Aⁿ are appropriately formed with ν_t or the ratio ϵ/k held constant. The modified scheme and underrelaxation ($\alpha < 1$) of the solution during initial iterations are required to prevent k and ϵ from becoming negative. Computational experience shows that negative values of k and ϵ quickly destroy the iteration process and cause the solution to diverge.

A few modified iterations are required to create k and ϵ values that are partially compatible with the current UWP values. The iterations are not continued until the k and ϵ solutions fully converge, because the current UWP solution is only approximate. Control is now passed back to the mean flow equation solver with updated values of k and ϵ and therefore new values of ν_i . Several iterations are performed with $\alpha = 1$ to align the UWP values with the updated distribution of ν_i . The solution scheme continues by passing from one equation set to another, iterating within each set as required, until there is no significant change in any of the variables. After several cycles the full Newton method may be implemented for the k- ϵ equations. Element Jacobian terms for this solution process are listed in Appendix I.

BOUNDARY CONDITIONS

Figure 1 depicts a basin in which the fluid enters at the upper left corner and exits over a weir at the upper right corner. The top of the flow is bounded



FIG. 2.—Finite Element Discretization of Tank Domain

by a surface of constant (atmospheric) pressure called a free surface. The sides and bottom of the basin are bounded by solid impermeable walls. The bottom of the tank is usually inclined at some small angle β . For a circular tank, the effect of slowly moving sludge rakes is ignored. The rakes in a rectangular basin often operate intermittently, in which case the rake velocity is periodically zero.

A typical finite element discretization of a tank domain is shown in Fig. 2. Along the inlet plane AB the values of U, W, k, and ϵ are specified as essential boundary conditions. The value of W is generally specified to be zero. Values of U, k, and ϵ should be obtained or inferred from experimental measurements. If such data are not available, these quantities may be estimated from other suitable computations or experiments. For example, the flow characteristics of a plane jet may aid the analyst in selecting appropriate inlet boundary values for this particular example.

The exit region EFG is approximated in the numerical computations. Although the free surface in this region actually curves downward under the influence of gravity as the fluid moves from F to G, the effect is of only local significance. A proper model of this region would substantially increase the overall computational cost since many additional elements would be required. For this reason the exit boundary of the flow field is conveniently chosen to be FE, which is far enough upstream of the weir that the surface is nearly level. The exit flow is modeled as a point sink centered at G and of such strength as to match the inflow discharge. This approximation appears reasonable since the head on the weir in most tanks is never more than 1% or 2% of the tank depth. The velocity components along EF are therefore computed in accordance with a sink located at point G. As experimental data become available, actual measured velocities in this exit region could be used for the velocity boundary conditions. Boundary values of k and ϵ for the exit region are undoubtedly determined from upstream events and the proximity of the free surface AF and vertical boundary DE. In this case it seems best to let the program compute the exit values of k and ϵ . Normal derivatives of k and ϵ along EF are thus set to zero. This specification is not strictly correct, since the flow from EF to G is nonuniform; however, any error introduced in this region will most likely not propagate far upstream because of the high velocities encountered in this region. If and when experimental values of k become available, essential boundary conditions along EF may then be specified, and the dissipation rate may be estimated from $\epsilon \simeq k^{3/2}/l$ in which l = a typical eddy length scale of the flow in this region.

The free surface AF is modeled as a rigid lid (18). The computational boundary AF is fixed as a horizontal surface of zero slope. Pressures along this surface are computed however, and thus the effects of any small surface slopes are still accounted for, since the pressure along the free surface is allowed to vary [the term $(\partial P/\partial r)$ in the horizontal momentum equation is nonzero]. The free surface boundary is also treated as a symmetry plane so that W=0, the shear stress uw is zero so that $(\partial U/\partial z)$ and $(\partial W/\partial x)=0$, and the normal derivatives $(\partial k/\partial z)$ and $(\partial \epsilon/\partial z)$ are zero.

The boundary conditions for the near-wall region are prescribed in a manner similar to those proposed by Launder and Spalding (17). The turbulence model is only valid in a fully turbulent regime. Therefore the finite element mesh is placed a distance δ away from the solid boundaries (see Fig. 2) and beyond both the viscous sublayer and the buffer region. The velocity component normal to the wall is required to vanish. Along the vertical walls BC and DE this condition requires U=0, while along CD, W=U tan β . A "slip" boundary condition is used parallel to the walls; the tangential stress is specified as a natural boundary condition. The wall shear stress is computed from the logarithmic law of the wall

$$\frac{V}{U_{-}} = \frac{1}{\kappa} \ln \left[E y^{+} \right] \qquad (23)$$

in which V = velocity parallel to the wall; κ = von Karman constant (=0.4); U_{τ} = friction velocity; E = constant (=9 for a smooth wall); and $y^+ = yU_{\tau}R_0$. Here y = normal distance from the wall to the point in question and R_0 = $(U_0h_0)/v$. The value of y = δ is selected to lie in the inertial subrange where the flow is assumed to be fully turbulent ($y^+ \approx 30$) but sufficiently close to

the wall (y^+ < 400) so that the shear stress is nearly constant (5). The shear-stress boundary condition along Γ_e in Eqs. 16 and 17 is specified using Eq. 23 as follows:

in which $c_f = \kappa^2 [\ln (Ey^+)]^{-2}$. The coefficient c_f resembles a resistance coefficient and is a function of U_* .

In the near-wall region production nearly balances dissipation or $\mathscr{P}_r \simeq \epsilon$. Combined with Eqs. 7 and 23, this relation provides the following wall boundary conditions on k and ϵ :

A pressure datum is required to obtain a unique solution. This is accomplished by setting P = constant at any one interior node and deleting the corresponding continuity equation from the global equation set for that node. The pressure may not be specified along any inlet or exit plane node, since conservation of mass along these boundaries then cannot be enforced (6).

APPLICATION—RECTANGULAR SEDIMENTATION BASIN

The two-dimensional planar model is used here to determine the velocity field within a rectangular settling unit. The predictions are obtained for a basin of modest size; length = 40 ft (12.2 m), width = 15 ft (4.6 m), inlet depth = 10 ft (3.0 m), outlet depth = 9 ft (2.7 m). Recommended operational surface-loading rates (discharge entering basin/surface area of tank) for untreated wastewater range from 600-1,200 gal/day/sq ft (0.028-0.057 cm/s) (19, pp. 448) and may be as high as 1,600 gal/day/sq ft (0.075 cm/s), (1, pp. 323) for plants with primary settling of iron- and polymer-coagulated raw wastewater. A surface loading rate of 1,500 gal/day/sq ft (0.071 cm/s) was selected for this example. This rate should simulate conditions in an overloaded primary clarifier and may indeed represent the lower limit of clarifier performance. For this example the characteristic velocity and length scale are chosen to be $U_0 = 0.1$ ft/sec (0.0305 m/s) and $h_0 = 10$ ft (3.05 m).

The finite element grid used in the numerical simulation is presented in Fig. 2. The distribution of elements is selected to be dense in the inlet and exit regions (where velocity gradients are large) and relatively more sparse in the interior domain.

The inlet region for this problem was chosen to be the upper three elements on the left hand side of the computational grid; the inflow velocity profile was approximated as one half of a plane jet. As noted by Larsen (14) in his full-scale studies of rectangular settling units, simple inlet structures produce velocity patterns similar to free jets a short distance from the inlet. A literature search for values of U, k, and ϵ pertaining to a plane jet (2,10) aided in selecting

approximate inlet conditions. The remaining boundary conditions were described in the previous action.

A vector plot of the computed velocity field is depicted in Fig. 3. The jet expands to fill the tank approximately 2.5 tank depths downstream from the inlet. The presence of the outlet is felt thereafter as the fluid streamlines converge toward the upper right hand portion of the basin. A recirculation zone is formed below the expanding jet. The zeros plotted in the lower corners represent velocities which are too small to be plotted by the graphic routine. In fact, close inspection of the computer output revealed a small recirculating eddy in each of these corners. At this time, experimental data of detailed point velocity measurements in primary sedimentation basins are unavailable for comparison. It is encouraging to note, however, that flow patterns measured by Clements and Khattab (3)

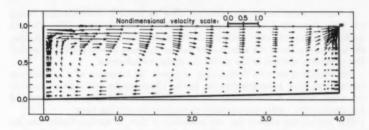


FIG. 3.—Vector Plot of Computed Velocity Field

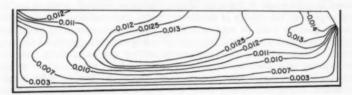


FIG. 4.—Contour Plot of Dimensionless Turbulent Kinematic Viscosity v.

on scale-model circular basins with surface inlets are qualitatively similar to the computed flow pattern depicted in Figure 3.

A contour plot of the dimensionless turbulent kinematic eddy viscosity $[\nu_t = \nu_t^* / (h_0 U_0)]$ is shown in Fig. 4. The distribution of ν_t is clearly not uniform; the most pronounced changes occur in the inlet and exit regions where velocity gradients are largest. Near the solid boundaries ν_t must decrease due to the damping effect of the wall on the turbulent fluctuations. Elsewhere the variation is less pronounced. It is quite apparent that this distribution of ν_t would be very difficult to specify a priori.

The numbers of elements and node points for this example are 135 and 454 respectively. The numbers of mean flow equations (UWP) is 995, and the number of turbulence equations $(k \in)$ is 788. The approximate numbers of nonzero entries in the Jacobian matrix A is 114,000 and 76,000, respectively, for the UWP

and $k \in$ sets of equations. This example required 6.2 min of central processor time on a CDC 7600 computer. The total number of *UWP* and $k \in$ iterations required to obtain a fully converged solution is 53.

A useful application of this solution is to use the known velocity field to solve the now-linear convection-diffusion equation describing the transport of particulate matter (25). In fact, the predicted variation of ν_i also allows one to assign known nonconstant values to the transport coefficients appearing in this equation. The settling efficiency of the basin may then easily be determined from the computed distribution of particulate concentration along the boundary of the tank.

SUMMARY AND CONCLUSIONS

A mathematical model for turbulent flow in primary sedimentation basins has been formulated and solved numerically via the Galerkin finite element method. Because the eddy viscosity is determined as part of the overall solution, the uncertainty about the selection of values for these coefficients is resolved. The predictive abilities of the model are therefore enhanced.

The computed velocity field clearly indicates the existence of a nonuniform recirculating flow pattern within the basin. These results qualitatively confirm the experimental measurements of several studies (3,14,28). The computed

distribution of v, varies considerably throughout the settling basin.

This project has shown that the modeling of flow in settling basins can be improved in several ways by additional research. First, a series of detailed experimental studies which can supply point velocity and possible Reynolds stress measurements in full-scale settling basins are needed to allow one to assess properly the validity of the current model. Once validated, the computational algorithm could be used to improve settling performance by examining the effects of tank geometry or inlet and exit configurations on predicted removal rates, or both. Second, while the present method can successfully compute the solution to a complex recirculating turbulent flow, the sensitivity of the Newton-based solution algorithm to initial values for the variables seems excessive. Additional research should endeavor to develop a solution procedure whose performance is less dependent on the initialization. Finally, the current model should be augmented to include stratified phenomena. Either temperature or species concentration variation may be the causative mechanism. However, mathematical models of turbulent stratified flow phenomena are less well developed than those for simpler flows and will undoubtedly require improvement and allied experimental confirmation before such flows are well simulated.

ACKNOWLEDGMENT

This paper is based on work supported by the National Science Foundation under Grant No. ENG 7618846.

APPENDIX I .- ELEMENT ENTRIES IN JACOBIAN MATRIX

$$\frac{\partial f_U}{\partial U_j} = \int_{\Omega_s} N_i \left[r^m \left(N_j \frac{\partial U}{\partial r} + U \frac{\partial N_j}{\partial r} + W \frac{\partial N_j}{\partial z} \right) + 2 m v_i N_j \right] d\Omega$$

$$+ \int_{\Omega_{e}} r^{m} \nu_{t} \left(2 \frac{\partial N_{i}}{\partial r} \frac{\partial N_{j}}{\partial r} + \frac{\partial N_{i}}{\partial z} \frac{\partial N_{j}}{\partial z} \right) d\Omega$$

$$+ \int_{\Gamma_{e}} r^{m} N_{i} \left(-2 \nu_{t} \frac{\partial N_{j}}{\partial r} l_{r} + \frac{\partial uw}{\partial U_{j}} l_{z} \right) d\Gamma \qquad (28)$$

$$\frac{\partial f_U}{\partial W_j} = \int_{\Omega_e} r^m N_i N_j \frac{\partial U}{\partial z} d\Omega + \int_{\Omega_e} r^m v_i \frac{\partial N_i}{\partial z} \frac{\partial N_j}{\partial r} d\Omega
- \int_{\Gamma} r^m N_i v_i \frac{\partial N_j}{\partial r} l_z d\Gamma \qquad (29)$$

$$\frac{\partial f_U}{\partial P_j} = -\int_{\Omega_s} m \, N_i M_j \, d\Omega - \int_{\Omega_s} r^m M_j \frac{\partial N_i}{\partial r} \, d\Omega$$

$$+ \int_{\Gamma_s} r^m N_i M_j l_i \, d\Gamma \, ... \qquad (30)$$

$$\frac{\partial f_{W}}{\partial U_{j}} = \int_{\Omega_{\epsilon}} r^{m} N_{i} N_{j} \frac{\partial W}{\partial r} d\Omega + \int_{\Omega_{\epsilon}} r^{m} v_{i} \frac{\partial N_{i}}{\partial r} \frac{\partial N_{j}}{\partial z} d\Omega
+ \int_{\Gamma_{\epsilon}} r^{m} N_{i} v_{i} \frac{\partial N_{j}}{\partial z} l_{r} d\Gamma \dots (31)$$

$$\frac{\partial f_{w}}{\partial W_{j}} = \int_{\Omega_{e}} r^{m} N_{i} \left(U \frac{\partial N_{j}}{\partial r} + N_{j} \frac{\partial W}{\partial z} + W \frac{\partial N_{j}}{\partial z} \right) d\Omega + \int_{\Omega_{e}} r^{m} v_{i} \left(\frac{\partial N_{i}}{\partial r} \frac{\partial N_{j}}{\partial r} + 2 \frac{\partial N_{i}}{\partial z} \frac{\partial N_{j}}{\partial z} \right) d\Omega - \int_{\Gamma_{e}} r^{m} N_{i} \left(\frac{\partial uw}{\partial W_{j}} I_{r} + 2 v_{i} \frac{\partial N_{j}}{\partial z} I_{z} \right) d\Gamma \dots (32)$$

$$\frac{\partial f_{w}}{\partial P_{j}} = -\int_{\Omega_{\sigma}} r^{m} M_{j} \frac{\partial N_{i}}{\partial z} d\Omega + \int_{\Gamma_{\sigma}} r^{m} N_{i} M_{j} I_{z} d\Gamma \dots (33)$$

$$\frac{\partial f_P}{\partial U_j} = \int_{\Omega_d} M_i \frac{\partial}{\partial r} (r^m N_j) d\Omega \qquad (34)$$

$$\frac{\partial f_P}{\partial W_I} = \int_{\Omega_*} M_I \frac{\partial}{\partial z} (r^m N_J) d\Omega \qquad (35)$$

$$\frac{\partial f_{k}}{\partial k_{j}} = \int_{\Omega_{\epsilon}} r^{m} N_{i} \left(U \frac{\partial N_{j}}{\partial r} + W \frac{\partial N_{j}}{\partial z} - 2c_{\mu} \frac{k}{\epsilon} N_{j} \Phi \right) d\Omega
+ \int_{\Omega_{\epsilon}} r^{m} \frac{v_{i}}{\sigma_{k}} \left(\frac{\partial N_{j}}{\partial r} \frac{\partial N_{i}}{\partial r} + \frac{\partial N_{j}}{\partial z} \frac{\partial N_{i}}{\partial z} \right) d\Omega
+ \int_{\Omega_{\epsilon}} 2r^{m} \frac{c_{\mu}}{\sigma_{k}} \frac{k}{\epsilon} N_{j} \left(\frac{\partial k}{\partial r} \frac{\partial N_{i}}{\partial r} + \frac{\partial k}{\partial z} \frac{\partial N_{i}}{\partial z} \right) d\Omega$$
(36)

$$\frac{\partial f_{k}}{\partial \epsilon_{j}} = \int_{\Omega_{\epsilon}} r^{m} N_{i} N_{j} \left(-c_{\mu} \frac{k^{2}}{\epsilon^{2}} \Phi + 1 \right) d\Omega$$

$$- \int_{\Omega_{\epsilon}} r^{m} \frac{c_{\mu}}{\sigma_{k}} \frac{k^{2}}{\epsilon^{2}} N_{j} \left(\frac{\partial k}{\partial r} \frac{\partial N_{i}}{\partial r} + \frac{\partial k}{\partial z} \frac{\partial N_{i}}{\partial z} \right) d\Omega \qquad (37)$$

$$\frac{\partial f_{\epsilon}}{\partial k_{j}} = - \int_{\Omega_{\epsilon}} r^{m} N_{i} N_{j} \left(c_{\epsilon_{1}} c_{\mu} \Phi + c_{\epsilon_{2}} \frac{\epsilon^{2}}{k^{2}} \right) d\Omega$$

$$+ \int_{\Omega_{\epsilon}} 2r^{m} \frac{c_{\mu}}{\sigma_{\epsilon}} \frac{k}{\epsilon} N_{j} \left(\frac{\partial \epsilon}{\partial r} \frac{\partial N_{i}}{\partial r} + \frac{\partial \epsilon}{\partial z} \frac{\partial N_{i}}{\partial z} \right) d\Omega \qquad (38)$$

$$\frac{\partial f_{\epsilon}}{\partial \epsilon_{j}} = \int_{\Omega_{\epsilon}} r^{m} N_{i} \left(U \frac{\partial N_{j}}{\partial r} + W \frac{\partial N_{j}}{\partial z} + c_{\epsilon_{2}} \frac{2\epsilon}{k} N_{j} \right) d\Omega$$

$$+ \int_{\Omega_{\epsilon}} r^{m} \frac{v_{i}}{\sigma_{\epsilon}} \left(\frac{\partial N_{j}}{\partial r} \frac{\partial N_{i}}{\partial r} + \frac{\partial N_{j}}{\partial z} \frac{\partial N_{i}}{\partial z} \right) d\Omega$$

$$- \int_{\Omega_{\epsilon}} r^{m} \frac{c_{\mu}}{\sigma_{\epsilon}} \frac{k^{2}}{\epsilon^{2}} N_{j} \left(\frac{\partial \epsilon}{\partial r} \frac{\partial N_{i}}{\partial r} + \frac{\partial \epsilon}{\partial z} \frac{\partial N_{i}}{\partial z} \right) d\Omega$$

$$\int_{\Gamma_{\epsilon}} r^{m} N_{i} \frac{\partial uw}{\partial U_{j}} l_{\epsilon} d\Gamma = - \int_{\Gamma_{\epsilon}} 2r^{m} N_{i} N_{j} c_{j} |U| l_{\epsilon} d\Gamma \qquad (40)$$

$$\int_{\Gamma_{\epsilon}} r^{m} N_{i} \frac{\partial uw}{\partial W_{i}} l_{\epsilon} d\Gamma = - \int_{\Gamma_{\epsilon}} 2r^{m} N_{i} N_{j} c_{j} |W| l_{\epsilon} d\Gamma \qquad (41)$$

APPENDIX II.—REFERENCES

- Wastewater Treatment Plant Design, Manual No. 36, by a Joint Committee of the American Society of Civil Engineers and the Water Pollution Control Federation, ASCE, 1977.
- Bradbury, L. J. S., "The Structure of a Self-Preserving Turbulent Plane Jet," Journal
 of Fluid Mechanics, London, England, Vol. 23, 1965, pp. 31-64.
- Clements, M. S., and Khattab, A. F. M., "Research into Time Ratio in Radial Flow Sedimentation Tanks," Proceedings of the Institution of Civil Engineers, Vol. 40, Aug., 1968, pp. 471-494.
- Gibson, M. M., and Launder, B. E., "On the Calculation of Horizontal, Turbulent, Free Shear Flows Under Gravitational Influence," Journal of Heat Transfer, American Society of Mechanical Engineers, Feb., 1976, pp. 81-87.
- Gosman, A. D., and Ideriah, F. J. K., "Teach-T: A General Computer Program for Two-Dimensional, Turbulent, Recirculating Flows," Report of the Department of Mechanical Engineering, Imperial College, London, England, 1976.
- Gresho, P. M., Lee, R. L., Sani, R. L., and Stullich, T. W., "On the Time-Dependent FEM Solution of the Incompressible Navier-Stokes Equations in Two- and Three-Dimensions," UCRL-81323, Lawrence Livermore Laboratory, July, 1978.
- Gresho, P. M., and Lee, R. L., "Don't Suppress the Wiggles—They're Telling You Something!" Proceedings of the Winter Annual American Society of Mechanical Engineers Meeting, Dec., 1979.
- Ha Minh, H., and Chassaing, P., "Some Numerical Predictions of Incompressible Turbulent Flow," Numerical Methods in Laminar and Turbulent Flows, C. Taylor, et al., eds., Pentech Press, London, England, 1978, pp. 287-300.

- Hamlin, M. J., and Wahab, A. H. A., "Settling Characteristics of Sewage in Density Currents," Water Research, Vol. 4, 1970, pp. 609-626.
- Hanjalic, K., and Launder, B. E., "A Reynolds Stress Model of Turbulence and its Application to Thin Shear Flows," *Journal of Fluid Mechanics*, London, England, Vol. 52, 1972, pp. 609-638.
- Hanjalic, K., and Launder, B. E., "Contribution towards a Reynolds-Stress Closure for Low-Reynolds-Number Turbulence," *Journal of Fluid Mechanics*, London, England, Vol. 74, 1976, pp. 593-610.
- Ideriah, F. J. K., "On Turbulent Forced Convection in a Square Cavity," Numerical Methods in Laminar and Turbulent Flow, C. Taylor, et al., eds., Pentech Press, London, England, 1978, pp. 257-269.
- King, I. P., Norton, W. R., and Iceman, K. R., "A Finite Element Model for Two-Dimensional Flow," Finite Element Methods in Flow Problems, J. T. Oden, et al., eds., UAH Press, 1974, pp. 133-137.
- Larsen, P., "On the Hydraulics of Rectangular Settling Basins Experimental and Theoretical Studies," Report No. 1001, Department of Water Resources Engineering Lund Institute of Technology, University of Lund, Lund, Sweden, 1977.
- Launder, B. E., Morse, A., Rodi, W., and Spalding, D. B., "Prediction of Free Shear Flows—A Comparison of the Performance of Six Turbulence Models," Proceedings of the Conference on Free Turbulent Shear Flows, NASA Langley Research Center, Vol. 1, July, 1972, pp. 361-422.
- Launder, B. E., Reece, G. J., and Rodi, W., "Progress in the Development of a Reynolds-Stress Turbulence Closure," *Journal of Fluid Mechanics*, London, England, Vol. 68, 1975, pp. 537-566.
- Launder, B. E., and Spalding, D. B., "The Numerical Computation of Turbulent Flows," Computer Methods in Applied Mechanics and Engineering, Vol. 3, 1974, pp. 269-289.
- McGuirk, J., and Rodi, W., "A Depth-Averaged Mathematical Model for the Near Field of Side Discharges into Open-Channel Flow," Journal of Fluid Mechanics, London, England, Vol. 86, 1978, pp. 761-781.
- Wastewater Engineering: Collection Treatment, Disposal, Metcalf and Eddy, Inc., McGraw-Hill Book Co., Inc., New York, N.Y., 1972.
- Montens, A., "The Use of Radioactive Isotopes for Water Flow and Velocity Measurement," Radioisotope Conference 1954, J. E. Johnston, ed., Butterworths, London, England, pp. 169-180.
- Oliver, A. J., "A Finite Difference Solution for Turbulent Flow and Heat Transfer Over a Backward Facing Step in an Annular Duct," Numerical Methods in Laminar and Turbulent Flow, C. Taylor, et al., eds., Pentech Press, London, England, 1978, pp. 467-478.
- Patankar, S. V., and Spalding, D. B., Heat and Mass Transfer in Boundary Layers, 2nd ed., Intertext, 1970.
- Sani, R. L., Gresho, P. M., and Lee, R. L., "On the Spurious Pressures Generated by Certain GFEM Solutions of the Incompressible Navier-Stokes Equations," Third International Conference on Finite Elements in Flow Problems, June, 1980.
- Schamber, D. R., and Larock, B. E., "A Finite Element Model of Turbulent Flow in Primary Sedimentation Basins," Proceedings of the Second International Conference on Finite Elements in Water Resources, C. A. Brebbia, et al., eds., Pentech Press, London, England, 1978, pp. 3.3-3.21.
- Schamber, D. R., "Finite Element Analysis of Flow in Sedimentation Basins," thesis
 presented to the University of California at Davis, in 1979, in partial fulfillment of
 the requirements for the degree of Doctor of Philosophy.
- Schamber, D. R., and Larock, B. E., "Computational Aspects of Modeling Turbulent Flows by Finite Elements," Computer Method in Fluids, C. Taylor, et al., eds., Pentech Press, London, England, 1980, pp. 339-361.
- Schamber, D. R., and Larock, B. E., "Constant and Variable Turbulent Eddy Viscosity
 Flow Simulations in Rectangular Settling Tanks," Presented at the Aug. 6-8, 1980,
 ASCE Hydraulics Division Specialty Conference, held at Chicago, Ill.
- Wills, R. F., and Davis, C., "Flow Patterns in a Rectangular Sewage Sedimentation Tank," Presented at the 1962, International Conference on Water Pollution Research, held at London, England, pp. 335-385.

APPENDIX III.-NOTATION

The following symbols are used in this paper:

A = Jacobian of equation matrix;

c = resistance coefficient:

 $c_{\mu}, c_{*1}, c_{*2} = \text{constants in turbulence model};$

D() = turbulent diffusion of quantity in parenthesis;

E = constant in law of wall relation;

F₀ = Froude number;

f =equation residuals;

f = system of nonlinear equations;

g = ratio of weight to mass;

h = elevation of free surface;

 $h_0 = \text{reference length};$

k = turbulence kinetic energy;

l = typical eddy length scale;

 $l_{r}, l_{s} =$ direction cosines;

 M_i, N_i = basis functions for interpolating polynomials;

m = constant defining planar or axisymmetric flow;

m = iteration counter:

P = mean pressure;

P, = production term;

 $R_0 = (U_0 h_0) / \nu$ (Reynolds number);

r = radial/horizontal coordinate;

U = mean radial/horizontal velocity component;

 U_0 = reference velocity; U_r = friction velocity;

u = radial/horizontal turbulent velocity fluctuation;

V = velocity parallel to solid boundary;

 V_R = rake velocity;

v = circumferential turbulent velocity fluctuation;

W = mean vertical velocity component;

w = vertical turbulent velocity fluctuation;

x = horizontal coordinate;

x =solution vector to f; $\delta x =$ corrections applied to x;

y = dimensionless normal distance from wall boundary of

 $y^+ = y U_a R_a;$

 $\alpha = \text{relaxation parameter};$

 β = angle of inclination of basin floor with horizontal;

 Γ = fluid domain boundary;

 Γ_e = element boundary;

 δ = distance from basin wall to computational grid;

 ϵ = rate of dissipation of turbulence kinetic energy;

k = von Karman constant;

ν = molecular kinematic viscosity;

 v_i = turbulent kinematic viscosity;

ρ = fluid density:

ρυυ, ρνν, ρωω, ρυω = turbulent Reynolds stresses;

 $\sigma_k, \sigma_k = \text{constants in turbulence model};$

 Φ = velocity gradient contribution to production term:

2 = fluid domain; and

 Ω_{\cdot} = element domain.

UNCERTAINTIES RESULTING FROM CHANGES IN RIVER FORM

By Durl E. Burkham¹

INTRODUCTION

Two recent laws enacted by the United States Congress have focused attention on the need for more information on the processes of sedimentation and on the hydraulics of flood flow in alluvial channels. The two laws are the Federal Water Pollution Control Act Amendments of 1972 (Public Law 92-500) (10) and the Flood Disaster Protection Act of 1973 (Public Law 93-234) (11). Public Law 92-500 requires, among other things, that an environmental impact statement for the affected area be made before actions are taken to manage the products of a drainage basin—water and debris—and to manage flood plains in the basin. Public Law 93-234 requires, among other things, that flood-prone areas be delineated. These requirements, which place man in the context of nature, demand that the reasons for changes in the landscape and the side effects of the changes be fully understood.

Major channel-form changes in a drainage basin can affect all components—the channel, surface-water yields and movement, sediment yields and movement, ground-water supply and movement—of the drainage system and the interrelation of the components. As will be analyzed in more detail subsequently, a specific river-form change in a large drainage basin may originally be local; however the effects of a local change usually propagate along alluvium-filled valleys to other parts of the basin.

This paper is concerned primarily with hydrologic implications and uncertainties that are created by temporal changes in alluvial-channel form in relatively large watersheds. Historical evidence of river-form changes is presented first. In sequential sections, brief examinations are presented about hydrologic implications and uncertainties relative to channel-form changes and land use, flood characteristics of alluvial streams, and hydrology and sediment yields for basins in the Southwest. Changes in river form are produced by processes involving long-term geologic influences, annual and seasonal fluctuations in the water and sediment runoff, and artificial influences exerted on the river by man's activities. This paper is particularly concerned with the aforementioned short-term processes.

¹Hydro., United States Geological Survey, 2800 Cottage Way, Sacramento, Calif. 95825. Note.—Discussion open until October 1, 1981. To extend the closing date one month, a written request must be filed with the Manager of Technical and Professional Publications, ASCE. Manuscript was submitted for review for possible publication on December 19, 1978. This paper is part of the Journal of the Hydraulics Division, Proceedings of the American Society of Civil Engineers, ©ASCE, Vol. 107, No. HY5, May, 1981. ISSN 0044-796X/81/0005-0593/801.00.

The term "uncertain," as used in this paper, means not definite, ascertainable, or fixed, as in time of occurrence, number, quantity, or place. Uncertainty—unpredictability, indeterminacy, or indefiniteness—is manifested as errors in data and in predictions.

River-channel form (river form) is the plan-view pattern and vertical cross-sectional shape of the river channel between river banks. Alluvial river form is described qualitatively as meandering, straight, or braided, and narrow and deep, or wide and shallow. Changes in river form cause changes in the flood plain. The flood plain is defined as nearly level land that occupies the bottom of the valley of a present stream and is subject to flooding unless protected artificially (1). A flood, as used in this report, is defined as the occurrence of water in excess of channel capacity; overbank flow occurs which inundates parts or all of the flood plain (15). For this paper, anything that occurs naturally on a flood plain—e.g., alluvial fans at the mouths of tributaries or vegetation—is considered part of the flood plain.

River-channel form, although a small part of the total landscape, is of special interest to man because development traditionally has been along the fertile, level land of the flood plains of rivers. Changes in the river-channel form, therefore, affect the quality of life and the value of property for these human

intruders on the flood plain.

Short-term processes effect changes in river form in alluvial channels in all regions of the United States. For most rivers, especially those in nonmountainous humid climates, the changes are usually minor, and the hydrologic consequences of the changes are insignificant. The changes in many rivers, especially some of those in the semiarid Southwest, however, have created highly significant consequences. Evidence of significant river-form changes for a few rivers in different locations in the United States are given in this paper. The factors and mechanisms involved in causing these changes are examined only in a general way.

HISTORICAL EVIDENCE OF RIVER-FORM CHANGE

The Rio Salado in central New Mexico is one of many streams in the Southwest where changes have occurred. The Rio Salado, a tributary of the Rio Grande, rises on the north side of the Datil Mountains and has a general eastward course north of that range to a junction with the Rio Grande at the village of San Acacia. According to Bryan (7), when Lorenzo Padilla, an early settler, saw the valley along the Rio Salado in 1880, the channel near Santa Rita, N.M., was not large and the broad, flat valley seemed a propitious place for farming. Daniel Curry, while surveying near Santa Rita in 1882, recorded the width of the stream bed as ranging from about 12 ft-49 ft (4 m-15 m) along a number of section lines (7).

Another surveyor in 1918, according to Bryan (7):

. . . found the course of the river radically different from that shown in Curry's survey of 1882, his measurements ranging from 330 to 550 ft in the same stretch of stream channel where Curry found widths of 11.88 to 48.84 ft.

Bryan (7) further states that:

. . . unlike many similar streams in New Mexico, which have not only widened their channels but deepened them in the same period, the Rio Salado, at least in the vicinity of Santa Rita, has even yet banks that are only 3 to 10 ft high and average about 5 ft high. It is obvious, however, that the whole regimen of the stream is much different from that which existed in 1880.

Smith (18) reported that the Republican River, in the northwestern corner of Kansas, was, prior to 1935, a narrow stream with a practically perennial flow of clear water, and with well-wooded banks. The Republican River in 1940, however, had a broad, shallow, sandy channel with intermittent flow; the trees had been destroyed, much valuable farmland on the valley bottom was sanded over, and the channel had been filled several feet. Smith associated the river-form change with the occurrence of a major flood in 1935.

Schumm and Lichty (16) reconstructed the river history of the Cimarron River in southwestern Kansas for the period 1874–1960. They reported that, in 1874, the river averaged 50 ft (15 m) in width in six counties. In the period 1914–1942, however, the Cimarron River widened to about 1,200 ft (366 m). After 1942, reconstruction of the Flood plain was in progress. By 1954, the channel averaged about 550 ft (168 m) in width.

Hack and Goodlett (12) reported that a violent cloudburst flood of June 1949 caused severe erosion in the Little River Valley in the mountain region in the Central Appalachians of Virginia. They state:

The runoff produced dozens of debris avalanches on the upper mountain slopes, enlarged most of the channel ways, and reworked the debris on the botton lands of many larger valleys and in places removed the forest cover on the entire valley floor.

A rare flood in December 1964 caused river-form changes in several valleys in northern California. Stewart and LaMarche (19) wrote:

The December 1964 flood on Coffee Creek (a small high-gradient mountain stream in Trinity County, California) was of rare frequency and unprecedented in historic time. Erosion and deposition during the flood were catastrophic and significantly changed the character of the valley. Some of this erosion and deposition was similar to that described by Hack and Goodlett (12) for northern Virginia. Within the valley, the preflood channel was commonly filled, and new channels formed at entirely different locations.

Storms in 1969 caused dramatic changes along small valleys in urban southern California. According to Scott (17):

A unique combination of substantial channel change and documentation of the changes by high-order photogrammetry was studied in Tujunga Wash in southern California. Extensive scour and fill occurred during

the record breaking 1969 floods in this 3-mile long, partly urbanized fanhead valley. Maxima of 20 ± 2 ft of net scour and 35 ± 2 ft of net fill were measured. . . . Net elevation change of the channel thalweg varied from as much as 14 ± 2 ft of scour to as much as 16 ± 2 ft of fill.

The writer (4) studied changes in river form in the Gila River in Safford Valley in southeastern Arizona for the period 1846–1970. The changes can be grouped into three periods—1846–1904, 1905–1917, and 1918–1970. From 1846–1904, the stream channel was narrow and meandered through a flood plain covered with willow, cottonwood, and mesquite. Only moderate changes occurred in the width and sinussity of the stream channel in this period; the average width of the stream channel was less than 150 ft (46 m) in 1875 and less than 300 ft (91 m) in 1903.

The average width of the stream channel of the Gila River increased during 1905-1917 to about 2,000 ft (610 m), mainly as a result of large winter floods that carried relatively small sediment loads (4). The meander pattern of the stream and the vegetation in the flood plain were destroyed completely by the floods.

The stream channel of the Gila River narrowed during 1918–1970 and the average width was less than 200 ft (61 m) in 1964 (4). The stream channel developed a meander pattern, and the flood plain became densely covered with vegetation. Minor widening of the stream channel occurred in 1965 and in 1967, and the average width of the channel was about 400 ft (122 m) in 1968. The reconstruction of the flood plain in 1918–1970 was accomplished almost entirely by the accretion of sediment.

The most important factors influencing the deposition of sediment in the Gila River during 1918–1970 were the wide flood channel and the small floods that carried relatively large sediment loads (4). The large sediment loads resulted mainly from rapid erosion of the alluvial deposits in the drainage basins tributary to the Gila River.

HYDROLOGIC IMPLICATIONS AND UNCERTAINTIES DUE TO CHANGES IN RIVER FORM

Introduction.—Major floods apparently were a primary cause of the river-form change for each of the samples cited in the preceding section. Large flood flows exert great force on the channel banks and on objects in the main flow path. During a major flood, the main flow path often is straight down valley. While the meander pattern is intact, part of the flow is directed along the meandering stream channel and a large amount of turbulence develops along the streambanks. As a result of the stresses produced by the turbulent forces along the streambanks and around other stationary objects, channel changes eventually take place—banks erode, trees are uprooted and flushed downstream, grass is removed, and alluvial fans at the mouths of tributaries are destroyed. These changes result in a wider and cleaner stream channel that is more conducive to rapid movement of flood waves and transport of the basin's debris during floods.

Reconstruction of a flood plain, typically during periods of relatively low flood peaks, is accomplished naturally by accretion of sediment; accretion results because the river, in absence of major floods, does not have the hydraulic

competence to move the inflow of sediment farther downstream. Flood plains may be built by sediment accretion in five general ways: (1) By the development of islands in the stream channel and their subsequent attachment to one bank by channel abandonment; (2) by direct deposition on the flood plains; (3) by deposition in the stream channel along the banks; (4) by formation of natural levees; and (5) by deposition on alluvial fans at the mouths of tributary streams. Rapid reconstruction of a flood plain depends on rapid erosion of surfaces or channels in the upstream drainage basin.

To generalize, much is known about the natural erosion and sedimentation processes involved when river-form changes occur. Most textbooks dealing with sediment transport and geomorphology present adequate general descriptions of the factors and processes involved. Based on present knowledge, many general questions concerned with the movement of water and sediment can be resolved. Public Laws 92-500 and 93-234, however, encompass specific problems pertinent to the movement of water and erosional debris that often require precise answers to specific questions. Often, exact determinations of the effects of man's activity are sought. Precise answers to specific questions, however, are not always obtainable, especially when the results of recent channel-form changes caused by nature are involved. For example, according to Wolman (20)

. . ruling on a controversy over logging in a redwood forest in California, Judge R. H. Kroninger wrote the following: "While numerous expert witnesses in the field of geology, forestry, engineering, and biology were presented, their conclusions and the opinions they derived from them are hopelessly irreconcilable in such critical questions as how much and how far solid particles will be moved by any given flow of surface water. They were able to agree only that sediment will not be transported upstream" [State of California, Marin County versus E. Richetti, and others, 1969].

As will be examined subsequently, the controversy over logging involves channel changes caused by floods.

Related reasons why flood-induced channel changes cause uncertainties pertinent to the aims of Public Laws 92-500 (10) and 93-234 (11) are as follows:

1. The capability to adequately determine whether a river is susceptible to a river-form change has not been established.

2. The capability to predict when a river-form change will occur does not exist because of the preceding reason and because of an inability to predict when a channel-changing major flood will occur.

3. A specific river-form change in a large drainage basin may originally be local; however the effects of a local change usually propagate along alluvium-filled valleys to other parts of the basin (4,9). The propagation process is not understood except in a general way (20); the rate of propagation through specific parts of a basin is varied and the rate cannot be adequately predicted.

4. The capability to predict the rate of reconstruction of a flood plain does not exist because, among other things, the rate depends on the sequence of floods, on flow rates, and on the sequence and rates of sediment inflow.

5. An adequate accounting of the timing and discontinuities of processes involved in sedimentation presently is not possible because the physical laws

of sediment transport are incompletely known, especially for the complex problem of transportation of the wide range of sediment sizes that are carried by natural streams, and sedimentation in natural streams involves many interrelated variables, most of which cannot be assigned meaningful numerical values.

6. For the first four reasons, drainage basin changes resulting from man's activities cannot be determined adequately because a basis for identifying flood-induced modification of a basin—river-form changes and subsequent adjustments—has not been established.

Because of the six aforementioned reasons, many problems pertinent to the management of water and debris, the management of flood plains, and the effects of man's activities in a drainage basin cannot be resolved except in a probabilistic or general way. The analysis in subsequent sections relates uncertainties caused by flood-induced channel changes to specific hydrologic problems and to specific procedures used in hydrologic studies.

Land-Use Problems.—Public Laws 92-500 (10) and 93-234 (11), as previously implied, require that the effects of man's use of drainage basins be fully understood. The controversies and uncertainties involving logging in the redwood forest in California and overgrazing in the Southwest are examples of those that involve uses of basins where flood-induced channel changes have occurred.

Logging in Redwood Forest in California.—The controversy in the redwood forest in California involves the effects of logging in causing changes in the forested landscape of the downslope Redwood National Park. The harvesting of the native timber probably influences changes in water discharge and sediment load, as well as adjustments in width, depth, sinuosity, gradient, and location of stream channels in the forest. Concurrently, natural flood-flow modification unrelated to the timber harvesting, if any, is likely to have been, or will be, of the same type, although not necessarily in the same direction. Janda (14) states:

Considerable geologic and geobotanical evidence is accruing to indicate that devastating floods (that is, large floods that bring about major change in stream channel and hill slope configuration) like those that occurred in 1955, 1964, and 1972 are naturally occurring phenomena in this area. . . The impact of these floods on stream sediment load is both immediate and of long duration. . . .

A long-term result of the large floods is to increase the amount of readily erodible sediment in and immediately adjacent to the stream channel.

Another probable long-term consequence of large floods in the redwood forest that must be accounted for in resolving the controversies over logging involves the translation of the effects of river-form changes to other parts of the drainage system. As stated by Gilbert in Chorley, Dunn, and Beckinsale (9):

Of the main conditions which determine the rate of erosion, namely; quantity of running water, vegetation, texture of rock, and declivity, only the last is reciprocally determined by rate of erosion. . . . Wherever by reason of change in any of the conditions the erosive agents come to have locally exceptional power, that power is steadily diminished by the reaction of

rate of erosion upon declivity. Every slope is a member of a series, receiving the water and the waste of the slope above it, and discharging its own water and waste upon the slope below. If one member of the series is eroded with exceptional rapidity, two things immediately result: first, the member above has its level of discharge lowered, and its rate of erosion is thereby increased; and second, the member below, being clogged by an exceptional load of detritus, has its rate of erosion diminished. The acceleration above and the retardation below, diminish the declivity of the member in which the disturbance originated; and as the declivity is reduced the rate of erosion is likewise reduced.

Precise answers such as those sought by the presiding judge (in the controversy over logging) presently are not obtainable because of the reasons previously given. Wolman (20) states:

Judge R. H. Kroninger's pique was probably directed at the fact that he had to choose a single number as the proper criteria for legal action (in the controversy over logging) and no good scientist would or could give him a single number.

Overgrazing in Southwest.—The controversy concerning the influence of extensive grazing on erosion in the Southwest in the latter part of the nineteenth century centers around the relative effects of land use as compared to natural flood-flow modification. Conservationists, for many years, have promoted the theory that overgrazing was a primary cause of the rapid erosion that occurred in alluvial valleys in the Southwest during the period 1880–1930. The period when rapid erosion gutted valleys followed closely years when large numbers of livestock were brought into the area and the amounts of precipitation were small. Logically, the combination of little precipitation and extensive grazing should cause a deterioration in the vegetation of the valleys, which would have made the alluvium more susceptible to erosion. Considering only these factors, the theory that overgrazing was a primary cause of deterioration of alluvium-filled valleys is easily accepted. Considerable evidence, however, is now available to indicate that overgrazing, in fact, may have been only a minor factor.

The beginning of severe erosion in southwestern valleys apparently correlates exceptionally well with the incidence of channel-changing major floods. Major floods, therefore, may have been a primary factor in causing the severe erosion in most of the southwestern valleys.

Bryan (7) stated:

Valid conclusions as to the merits of these theories [theories concerned with the causes of severe erosion in the Southwest] cannot be reached until historical data on the time at which erosion began have been accumulated. Knowledge of the date of the beginning and progress of this spectacular change in the regimen of streams is particularly necessary in arriving at a decision as to the effects on erosion processes of the introduction of cattle and sheep and the overgrazing that in most localities ensued.

He associated the beginning of severe erosion along the Rio Salado with an exceptional rain and flood in 1883. The Rio Salado drains a basin where extensive grazing occurred in the latter part of the nineteenth century. Bryan (7) stated:

. . . the progress of erosion [in the Rio Salado] begun near Santa Rita in 1883 has been, as measured in years, fairly slow and has not yet, 43 years later, affected all the minor tributaries.

The writer's observations during a visit to the site in 1969 indicate that head-cut erosion is still progressing upstream in minor tributaries; this probably indicates that the cycle of erosion that began with the flood in 1883 is continuing. In 1969, the depth and width of the Rio Salado near Santa Rita apparently were not significantly different than those recorded in 1918.

The results of a study by Schumm and Lichty (16) seem to indicate that overgrazing was an insignificant factor, and floods may have been a primary factor in causing the channel changes along the Cimarron River in southwestern

Kansas. They wrote:

The period of channel widening was initiated by the maximum flood of record, which was followed by a long period of deficient precipitation, and was terminated by the major flood of 1942. The period of flood-plain construction was characterized by above-average annual precipitation and floods of low to moderate peak discharge. . . McLaughlin . . . concluded that, because there was no major change in number of livestock, grazing was not an important factor determining channel changes. . . Livestock density was greatest during the period of channel narrowing 1942–48. The activities of man and animals in the Cimarron River basin undoubtedly had their effects on the regime of the river, but any relation between cultivation, grazing, and channel change is obscure.

Studies of channel changes along the Gila River in southeastern Arizona apparently also support a premise that floods were the major factor in causing channel changes in the Southwest and that overgrazing probably was a minor factor (4). The widening of the Gila River in 1891, 1905–1917, 1941, and 1965–1967 was coincident with major floods. Most of the floods originated in the mountainous part of the headwater area as a result of large storms. The floods originated in areas where there was no significant grazing. Grazing apparently did not have a significant influence in causing the major floods and probably had only a minor influence in causing the widening of the stream channel of the Gila River. Large-scale grazing began in about 1872 in parts of the Gila River below the shaded mountain forest and below the area that produced most of the flood flow; grass was the dominant vegetation in these areas. If grass had been the dominant vegetation in the flood-producing areas, then the floods probably would have been slightly more severe.

The high flows in the Gila River drainage during the period 1905-1917 lowered the local base level and accelerated erosion in the tributaries of the Gila River by increasing the gradient of most of the tributaries at their confluence with the Gila River. High flows in the tributary streams provided the motive power necessary to start erosion (4). Generally, severe erosion occurred rapidly in

the steep streams that drain the mountainous terrain near the Gila River; however the areal extent of the channel erosion was small because of the small areal extent of the easily erodible alluvium that underlies these streams. Overgrazing was not a factor in causing erosion in the mountainous terrain because grazing was insignificant. Overgrazing could have been a contributing factor in causing erosion in alluvial valleys drained by gently sloping streams because they were grazed extensively, and erosion in some of the valleys was severe.

The San Simon River, tributary to the Gila River in Safford Valley, is an example of a gently sloping stream that has undergone severe channel erosion since 1905 (4). The San Simon River drains an area of about 2,200 sq mile (5,698 km²), and its valley covers most of the drainage basin. The San Simon River was an insignificant and poorly-defined watercourse in 1903. Debris from side tributaries apparently had been collecting in the alluvium-filled valley for centuries, and in 1905 it was poorly drained and relatively unstable. When severe erosion began, probably during the major floods of 1905, deep channels were cut and eventually became large; erosion then spread to the side tributaries according to Gilbert's theory (9). Around 1919, a deep eroded channel had extended upstream for about 60 mile (97 km). By 1960, there were more than 100 mile (161 km) of gullied channel from 10 ft-40 ft (3 m-12 m) deep, and from 20 ft-500 ft (6 m-152 m) wide. The gullied channels captured runoff that, prior to the erosion, would have spread over the valley and replenished soil moisture necessary for plant growth. As the water flowed into the deep channels, additional erosion occurred; however the eroded sediment, generally of small particle size, was easily moved downstream because the flow was confined. A ditch dug at the mouth of the San Simon River may have influenced channel erosion in the stream. The ditch was dug by settlers prior to 1900 to divert floods in the San Simon River away from the cultivated land. Because severe erosion took place at the same time in other gently sloping streams, the erosion in the San Simon River basin probably would have occurred even if the ditch had not been dug. Because severe erosion occurred in steep channels that drain the mountainous terrain near the Gila River where grazing was not a factor, the erosion in the San Simon River basin probably would have occurred even if extensive grazing had not taken place.

To summarize, major floods that caused changes in channel form probably were a primary factor influencing severe erosion in alluvial valleys in the Southwest during 1880–1930. Extensive grazing during the latter part of the nineteenth century, however, probably was a contributing factor. Even after an elapsed time of about 100 yr and the collection of data during many studies, precise determinations of the effects of extensive grazing on erosion in relative large drainage basins in the Southwest have not been made primarily because of the reasons previously described.

Flood Characteristics of Alluvial Streams

Introduction.—Major channel-form changes can significantly affect the flood characteristics of streams—timing, transformation of floods in travel, magnitude and frequency of floods, and the bankfull capacity of streams. As will be indicated in the following, studies—such as those of flood routing, frequency of flooding and channel capacity, and in-regime flow—that deal with flood characteristics of streams, must consider the effects of channel-form changes in order to minimize errors and bias.

Flood Routing.—Flood routing is the process of determining progressively the timing and magnitude of a flood wave at successive points along a river. The prediction of the timing and magnitude of a flood wave in a reach of interest is usually based on a flood-routing model. The principal types of flood-wave movement are classified as uniformly progressive and reservoir action (8). Uniformly-progressive flood-wave movement is the downstream movement of a flood wave that does not change in shape; such movement occurs under ideal conditions in a prismatic channel in which the variation in resistance along the channel is small. Reservoir action refers to the transformation of a flood

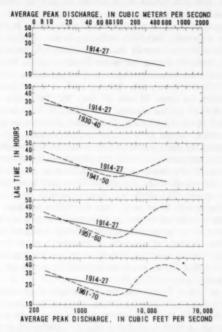


Fig. 1.—Relations between Average Peak Discharge and Lag Time of Center of Mass of Flood Waves Moving Through a 55-mile (88-km) Reach of Gila River in Safford Valley, Ariz., for Indicated Water Years (after (5))

wave caused by reservoir pondage which results when the channel is irregular and the variation in resistance along the channel is large. Both types of flood-wave movement can occur at different times in the same reach; the type that will occur apparently is dependent largely on the river form.

More than 250 inflow and outflow hydrographs for flood waves in 1914-1970 for a 55-mile (88-km) reach along the Gila River in southeastern Arizona were reviewed to determine temporal adjustments in flood-wave transformation caused by changes in the river form (5). As previously noted, the channel was relatively

wide—about 2,000 ft (610 m)—in 1905-1917. During 1918-1940; the channel changed; the stream channel became narrow, stream channel meander increased, natural levees developed along the stream channel, flood plain vegetation spread and became dense, and large alluvial fans developed at the mouths of tributaries (4). After the changes, the Gila River consisted of a stream channel in which flow below bankfull discharge—3,000 cu ft/sec-5,000 cu ft/sec (85 m³/s-142 m³/s) after 1930—moved relatively fast, and a congested flood plain in which flood flow moved slowly. Floods having average peak discharges of 10,000 cu ft/sec-20,000 cu ft/sec (283 m³/s-566 m³/s) (mean of peak rates at the ends of the reach) moved through the 55-mile (88-km) reach in about 14 h in 1914-1927; however it took them more than 40 h to move through the reach in 1961-1970 (see Fig. 1).

Flood waves during 1914-1927 generally retained their inflow shape (hydrograph shape at the upstream end of the study reach) as they moved through the study reach on the Gila River (see Fig. 2), and the flood-wave movement

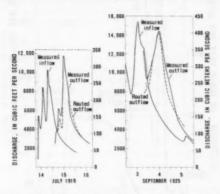


FIG. 2.—Measured and Synthesized Flood Flow, July 14–16, 1919, and September 3–5, 1925, at End of 55-mile (88-km) Reach of Gila River in Safford Valley, Ariz. [after (5)]

approximated a uniformly progressive one (5). The uniformly-progressive flood-wave movement, however, applies only to floods that were not reduced significantly by infiltration. Infiltration during many floods in the 1914–1927 period significantly reduced the size of the floods, and in many instances, the inflow shapes were altered.

Floods were transformed greatly from about 1935-1970 as they moved through the study reach on the Gila River, probably as a result of reservoir action caused by the meandering stream channel and flood plain vegetation (see Figs. 3 and 4) (5). Infiltration also may have been a cause for the change in inflow shape. Significant temporal changes in the attenuation of peak rates moving through the study reach accompanied changes in wave shape. Peak rates of less than about 13,000 cu ft/sec (368 m³/s) were reduced to bankfull discharge, between 3,000 cu ft/sec and 5,000 cu ft/sec (85 m³/s and 142 m³/s), for most floods that occurred in 1955-1965, and the average reduction in peak

rates ranged from about 7,000 cu ft/sec (198 m³/s) for floods having inflow peaks of 14,000 cu ft/sec (396 m³/s) to about 4,000 cu ft/sec (113 m³/s) for floods having inflow peaks of 44,000 cu ft/sec (1,250 m³/s) during the same period. The increased attenuation of peak flow from 1914–1927 to 1944–1965 probably resulted from temporal increases in reservoir action and infiltration. Decreases in the amount of streamflow contributed by tributary watersheds

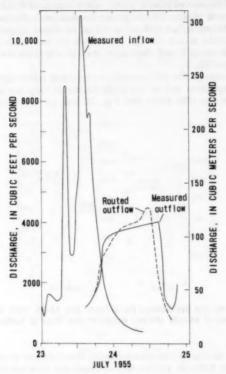


FIG. 3.—Measured and Synthesized Flood Flow, July 23–25, 1955, at End of a 55-mile (88-km) Reach of Gila River in Safford Valley, Ariz. [after (5)]

along the study reach may also have caused some difference in peak outflow. Tributary streamflow ponded behind natural levees during 1944–1965 (5); the natural levees were not present during 1914–1927.

Conclusions resulting from the study on the 55-mile (88-km) reach on the Gila River that may be pertinent to flood routing in other rivers subject to river-form changes are:

1. The size and meander pattern of the stream channel of the Gila River are determined by past dominant flows. The stream channel is wide and straight

at the end of a period in which high flows were dominant, and is narrow and has a meander pattern at the end of a period in which low flows were dominant.

2. The stream channel and flood plain system, when fully developed for a dominant flow, has a persistent effect on floods. A low-flow system—developed by and for low flows—attenuates flood peaks passing through the reach; the peak flows of flashy floods may be reduced to bankfull discharge. A high-flow system—developed by and for high flows—does not increase flood rates; however streamflow from side tributaries along the study reach may contribute more significantly to peak rates in the Gila River when a high-flow rather than a low-flow system exists.

3. The downstream velocity of the center of mass of flood waves that had peak discharges of between 10,000 cu ft/sec and 20,000 cu ft/sec (283 m³/s-566 m³/s) during 1914-1927 may have been as much as three times that for the same rates during 1943-1970.

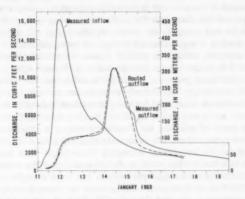


FIG. 4.—Measured and Synthesized Flood Flow, January 11-19, 1960, at End of a 55-mile (88-km) Reach of Gila River in Safford Valley, Ariz. [After (5)]

4. A low-flow system may change rapidly to a high-flow system when a series of major floods occurs; however several years of low flow are required before a high-flow system changes to a low-flow system. It took about 50 yr for the 1970 low-flow system in the Gila River to develop.

5. Annual peak flows measured at the downstream end of the study reach reflect, among other things, the persistent effect of the upstream system, and therefore they are not as random in time as are flows at the upstream end. Because of changes in the system, the data of peak flows collected at the downstream end of the study reach during 1914–1927 are from a different population than the data of peak flows for the period 1943–1970.

6. A flood-routing model used to predict the timing and transformation of a flood wave must have the capability to account for the effects of river-form changes; this accounting is difficult to accomplish for many streams because of reasons previously given. Frequency of Flooding and Channel Capacity.—The frequency of flooding in a reach of river clearly depends on both the flow rate and the bankfull capacity of the stream channel. River-form changes along a river, therefore, can affect the frequency of flooding in two ways—by changing the peak flow rate and by changing the bankfull capacity of the river. This causes uncertainties in the delineation of flood-prone areas.

The method of delineating flood-prone areas—flood mapping—for flood-insurance studies pertinent to Public Law 93-234 usually consists of two parts: (1) Peak discharge-frequency analysis; and (2) hydraulic analysis. A peak discharge-frequency curve is a product of the frequency analysis. This curve is based mainly on historical peak discharge rates; however precipitation data are used in conjunction with annual peak flows for some analyses. These rates reflect, among other things, the persistent effects of the upstream drainage system and the effects of river-form changes in the system. As previously mentioned, the data for a given site for a flood occurring during a period when a stream channel is narrow and meandering through a valley are often from a different population than data for a flood occurring in a period when the channel is wide and straight. As shown by the writer (5), the reduction in peak flow caused by a major channel change can be significant.

Hydraulic analyses needed to predict T-year water-surface elevations (the elevation that will occur, on an average, once in T-years—10 yr, 50 yr, 100 yr) for flood-insurance purposes generally assume that the present channel boundary will not change significantly prior to the occurrence of the T-year flood. This assumption is not valid for many streams embedded in unconsolidated alluvial deposits, and it may lead to significant bias in predicting T-year elevations. The standard error of estimate for T-year elevations is relatively large even for rigid boundary conditions; the nationwide standard error of estimate is about 5.0 ft (0.9 m) (6). If the channel boundary is not rigid, then major changes in river form can result when extreme floods occur, and the accuracy for the predicted water-surface elevation probably is low even though the magnitude of discharge for a given frequency of occurrence is assumed to be predictable. For example, river-form changes along the Gila River that have been previously described probably resulted in a 6 ft-8 ft (1.8 m-2.4 m) difference in the water surface for a 25-yr flood.

In-Regime Concepts.—Many engineering approaches to solving hydraulic problems in alluvial channels use the in-regime concepts introduced by Blench (2). Blench's definition of "in-regime" is:

. . . that average values of the quantities we appreciate as constituting regime do not show a definite trend over some interval—usually of the order of a score or two of years . . . [rivers in regime] demonstrate themselves to us in the form of varying discharges, breadths, depths, velocities, meander patterns, sediment contents, and so forth, but their average behavior does not usually change greatly over small periods of historic time.

The in-regime approach to solving hydraulic problems has been to describe the hydraulic characteristics of a river in terms of time-average quantities. The hydraulic geometry equations developed by Leopold and Maddock (15) are examples of this approach. The in-regime concept is valid for streams where the channel boundary can withstand stresses to such an extent channel form is not significantly changed during temporary periods of high flow. Even though the boundary of a stream embedded in unconsolidated alluvium may be in a constant state of change when flow occurs, the in-regime concept may be valid if major channel-form changes do not occur.

The major channel-form changes for alluvial valleys described previously in this paper have occurred mainly because of temporal changes in the dominant flow rate. Small (relative to a channel that could contain a major flood) channels that have a meander pattern and a vegetation-covered flood plain are closely associated with dominantly low-flow rates. The in-regime concept probably applies to these relatively small channels and low-flow conditions (relative to rates during a major flood). The in-regime concept also probably applies to relatively large straight channel and high-flow conditions. Considering a long period of time and a large region where channel-form changes occur, most channels are small because of the temporal and spatial dominance of low-flow rates. For the period and region, the in-regime concept probably is valid for most channels. A few channels in the large region, however, may be in a state of flux between a high-flow channel and a low-flow channel; the in-regime concept is not valid for this condition and these channels. Of the channels in a state of flux, some stay relatively large for a long period of time even though low-flow conditions prevail. The Rio Salado in New Mexico is an example. Of the channels in a state of flux, some have changed in the last 100 vr from a low-flow type to a high-flow type and back to a low-flow type; the Gila River in Safford Valley is an example.

In-regime concepts are used as a basis for estimating average runoff from drainage basins in arid and semi-arid regions (13). In the procedure, measured average annual flow is regressed against selected dimensions of channel geometry—usually width and depth at bankfull stage; or width and depth of a cross section between bars and berms. The degree of correlation usually is reasonably good because, on an average, most channels reflect the temporal dominance of low-flow rates in a region and the average annual discharge adequately represents the low-flow rate. The regression equation is used to estimate runoff from basins drained by ungaged streams. The procedure usually gives adequate results if data for channels that are in a state of flux between a high-flow channel and a low-flow channel do not significantly affect results.

Hydrology and Sediment Yields for Basins in Southwest.—Major river-form changes can cause significant differences in the surface runoff, in recharge to aquifers, and in sediment yields in affected basins, especially in arid and semi-arid regions of the United States. Most of the natural recharge to aquifers in arid and semi-arid regions occurs as a result of infiltration during intermittent flow in channels embedded in alluvium deposits. Infiltration depletes runoff and replenishes ground water. Infiltration in an alluvial channel is dependent on many factors (3): (1) Surface area and depth of water in the region; (2) permeability, moisture distribution, and temperature of the subsurface alluvium; (3) physical quality of the water and length of time the water is available at the land surface; (4) chemical quality of the surface and subsurface water; and (5) structural stability of the porous media. Many of the dominant forces and parameters affecting infiltration are related directly to the width, depth,

and velocity of streamflow. As previously shown, these parameters are significantly altered by major changes in channel form. A significant change in the infiltration rate would cause a significant change in the runoff and the ground-water recharge.

The rate of sediment movement at a site in a stream depends on two factors—hydraulic conditions at the site and the supply of sediment readily available for movement. Major channel-form changes significantly alter both factors. The water-discharge to sediment-discharge relationship for a site, therefore, often is significantly transformed when a major channel-form change occurs; the annual sediment yield from the affected basin also usually is significantly altered.

SUMMARY AND CONCLUSIONS

The uncertainties resulting from major changes in river form in many large drainage basins are of such magnitude that the objectives of Public Laws 92-500 and 93-234 relative to the management of water and debris, the management of flood plains, and the effects of man's activities presently cannot be met except in a probabilistic or general way. Rivers in arid and semi-arid regions are more susceptible to major changes in river form than those in more humid regions.

Channel-form changes caused by natural processes create uncertainties for the following related reasons:

1. The capability to adequately determine whether a river is susceptible to a river-form change has not been established.

2. The capability to predict when a river-form change will occur does not exist because of the preceding reason, and because of an inability to predict when a channel-changing major flood will occur.

3. A specific river-form change in a large basin may originally be local; however the effects of a local change usually propagate along alluvium-filled valleys to other parts of the basin. The propagation process is not understood except in a general way, and the rate of propagation through specific parts of a basin is varied and cannot be adequately predicted.

4. The capability to predict the rate of reconstruction of a flood plain does not exist. Among other things, rate depends on the sequence of floods, on

flow rates, and on the sequence and rates of sediment inflow.

5. An adequate accounting of the timing and discontinuities of processes that are involved in sedimentation presently is not possible because the physical laws of sediment transport are incompletely known, especially for the complex problem of transporting the wide range of sediment sizes that are carried by natural streams, and sedimentation in natural streams involves many interrelated variables, most of which cannot be assigned meaningful values.

6. For the first four reasons, water basin changes resulting from man's activities cannot be determined adequately because a basis for identifying changes in a drainage system resulting from natural flood-flow modifications has not been

established.

Examples of controversies and perplexing situations that involve channel-form changes are:

- 1. Logging in the uplands of the redwood forest in California: The controversy involves the role of logging in causing changes in the forested landscape of the downslope Redwood National Park. The harvesting of the native timber probably influences changes in the rates of erosion and deposition in the forested land and influences changes in width, depth, sinuosity, gradient, and location of stream channels in the forest. Concurrently, natural flood-flow modification unrelated to timber harvesting is likely to have been, or will be, of the same type, although not necessarily in the same direction. Because of reasons outlined in the preceding, changes in the basin caused by man's activity cannot be precisely established.
- 2. Overgrazing in the Southwest: Conservationists, for many years, have promoted the theory that overgrazing was a primary cause of the rapid erosion in alluvium-filled valleys that occurred in the Southwest during the period 1880–1930. Considerable evidence is now available to indicate that overgrazing, in fact, may have been only a minor factor. The rapid erosion apparently was a naturally-occurring phenomenon brought about largely by major floods.
- 3. Flood routing: Prediction of the timing and transformation of a flood wave based on a flood-routing model can have significant error if an accounting of the effects of river-form changes has not been properly considered.
- 4. Frequency of flooding and hydraulics of floods: The frequency of flooding in a reach of river depends on both the flow rate and the bankfull capacity of the stream channel. River-form changes affect the frequency of flooding in two ways—by changing the peak flow rates and by changing the bankfull capacity of the stream channel. Flood-insurance studies pertinent to Public Law 93-234 are made using the assumption that the present bounding conditions existing in a channel will not change significantly prior to the occurrence of a T-year flood. This assumption can lead to significant error and bias for channels where major channel-form changes have occurred.
- 5. In-regime concepts: The in-regime concept is valid for streams where the channel boundary can withstand stresses to such an extent that channel form is not significantly changed during high flows. Even though the boundary of a stream embedded in unconsolidated alluvium may be in a constant state of change during a variation of flow rates, the in-regime concept is valid if major channel-form changes do not occur. Many channel-form changes result because of temporal changes in the dominant flow rate. Relatively small channels correlate with relatively low flow rates; relatively large channels correlate with relatively high flow rates. Many channels in a large region may be in a state of flux between a high-flow channel and a low-flow channel; the in-regime concept is not valid for these channels.
- 6. Surface runoff, ground-water recharge, and sediment yields: Major river changes can cause significant differences in the surface runoff, recharge to aquifers, and sediment yields in the affected basins.

APPENDIX.—REFERENCES

- "Nomenclature for Hydraulics," Manuals and Reports on Engineering Practices, No. 43, ASCE, New York, N.Y., Feb., 1962, p. 165.
- Blench, T., "Regime Behavior of Canals and Rivers," Butterworths Scientific Publications, London, England, 1957, pp. 2-3.

- Burkham, D. E., "A Method for Relating Infiltration Rates to Streamflow Rates in Perched Streams," *Professional Paper 700-D*, United States Geological Survey, Washington, D.C., 1970, pp. D266-D271.
- Washington, D.C., 1970, pp. D266-D271.
 Burkham, D. E., "Channel Changes of the Gila River in Safford Valley, Arizona 1846-1970," Professional Paper 655-G, United States Geological Survey, Washington, D.C., 1972.
- Burkham, D. E., "Effects of Changes in an Alluvial Channel on the Timing, Magnitude, and Transformation of Flood Waves, Southeastern Arizona," Professional Paper 655-K, United States Geological Survey, Washington, D.C., 1976.
- Burkham, D. E., "Accuracy of Flood Mapping," Journal of Research, Vol. 6, No. 4, July-August, 1978, pp. 515-527.
- Bryan, K., "Channel Erosion of the Rio Salado, Socorro County, New Mexico," Contributions to the Geography of the United States, Bulletin 790, United States Geological Survey, Washington, D.C., 1927, pp. 17-19.
- Carter, R. W., and Godfrey, R. G., "Storage and Flood Routing," Water-Supply Paper 1543-B, United States Geological Survey, Washington, D.C., 1960, pp. 81-104.
 Chorley, R. J., Dunn, A. J., and Beckinsale, R. P., The History of the Study of
- Chorley, R. J., Dunn, A. J., and Beckinsale, R. P., The History of the Study of Landform or the Development of Geomorphology—Volume 1, Geomorphology Before Davis, John Wiley and Sons, Inc., New York, N.Y., 1964.
- Federal Water Pollution Control Act Amendments of 1972, Public Law 92-500, United States Congress, Washington, D.C., 1972.
- Flood Disaster Protection Act of 1973, Public Law 93-234, United States Congress, Washington, D.C., 1973.
- Hack J. T., and Goodlett, J. C., "Geomorphology and Forest Ecology of a Mountain Region in the Central Appalachians," *Professional Paper 347*, United States Geological Survey, Washington, D.C., 1960, pp. 48-51.
- Hedman, E. R., "Mean Annual Runoff as Related to Channel Geometry of Selected Streams in California," Water-Supply Paper 1999-E, United States Geological Survey, Washington D.C., 1970.
- Janda, R. J., Testimony Concerning Stream Sediment Loads in Northern California and Southern Oregon, presented before the California Regional Water Quality Control Board, North Coast Region, Eureka, Calif., 1972.
- Leopold, L. B., and Maddock, T., Jr., "The Hydraulic Geometry of Stream Channels and Some Physiographic Implications," *Professional Paper 252*, United States Geological Survey, Washington, D. C. 1953.
- cal Survey, Washington, D.C., 1953.
 Schumm, S. A., and Lichty, R. W., "Channel Widening and Flood-Plain Construction along Cimarron River in Southwestern Kansas," *Professional Paper 352-D*, United States Geological Survey, Washington, D.C., 1963.
- Scott, K. M., "Scour and Fill in Tujunga Wash—A Fanhead Valley in Urban Southern California—1969," Professional Paper 732-B, United States Geological Survey, Washington, D.C., 1973.
- Smith, H. T. U., "Notes on Historic Changes in Stream Courses of Western Kansas, with a Plea for Additional Data," *Transactions*, Kansas Academy of Science, Vol. 43, 1940.
- Stewart, J. H., and LaMarche, V. C., Jr., "Erosion and Deposition Produced by the Flood of December 1964 on Coffee Creek, Trinity County, California," Professional Paper 422-K, United States Geological Survey, Washington, D.C., 1967.
- Wolman, M. G., "Changing Needs and Opportunities in the Sediment Field," Water Resources Research, Vol. 13, No. 1, Feb., 1977, pp. 50-54.

MAXIMUM CLEAR-WATER SCOUR AROUND CIRCULAR PIERS

HY5

By Subhash C. Jain, M. ASCE

INTRODUCTION

The safe and economical design of bridge piers requires accurate prediction of the maximum expected depths of scour of the stream bed around them. The interaction between the flow around a bridge pier and the erodible sediment bed surrounding it is very complex. In fact, the phenomenon is so involved that only very limited success has been enjoyed by the attempts to model scour computationally, and physical models remain the principal tool employed for estimating expected depths of scour. Two types of scour may be identified: (1) Clear-water scour-where material is removed from the scour hole and not replaced; and (2) scour-that occurs with general sediment transport. Following the experimental study of Chabert and Engeldinger (8) on local scour around bridge piers, most of the investigators in this area concurred on the general shape of the curve which delineates the variation of scour depth with mean flow velocity. According to this curve, scour depth increases with increase in mean velocity in the clear-water regime, reaches an absolute maximum at a velocity approximately equal to the threshold velocity (hereinafter referred to as the mean velocity for incipient sediment motion), and decreases slightly with further increase in mean velocity in the sediment-transport regime where it fluctuates nonperiodically about the equilibrium scour depth due to bed-form migration. Since the maximum scour depth is required in designing bridge piers, most of the experimental studies in the past were conducted either in the clear-water regime or with flow velocities not much higher than the threshold velocity in the sediment-transport regime.

A wide variety of empirical equations based upon a limited range of data (both laboratory and prototype) have been developed in the past to estimate the maximum scour depths around bridge piers. Unfortunately the relatively large scatter in the available data on local scour around bridge piers makes it possible to fit a wide variety of curves which diverge greatly at high Froude numbers and high relative depths of the flow. Not only that their extrapolation to higher Froude numbers and relative depths cannot be used as a sound basis

¹Research Engr., Inst. of Hydr. Research, The Univ. of Iowa, Iowa City, Iowa 52242. Note.—Discussion open until October 1, 1981. To extend the closing date one month, a written request must be filed with the Manager of Technical and Professional Publications, ASCE. Manuscript was submitted for review for possible publication on October 17, 1980. This paper is part of the Journal of the Hydraulics Division, Proceedings of the American Society of Civil Engineers, ©ASCE, Vol. 107, No. HY5, May, 1981. ISSN 0044-796X/81/0005-0611/\$01.00.

for pier design, it is also difficult to draw conclusions regarding the appropriateness of these formulas at low Froude numbers and relative depths. In this study, the potential predictors of the maximum clear-water scour are compared with the experimental data. The limitations of these predictors are considered. Another formula to predict the maximum clear-water scour is proposed.

ESTIMATION OF SCOUR DEPTH

The flow in the vicinity of the pier is so complex that a complete analytical or numerical description of the scour process is not possible at the present time. Accordingly, phenomena involving local scour around bridge piers have

TABLE 1.—Constants and Exponents in Eq. 1

Group (1)	Investigator (2)	Regime (3)	Approach (4)	A (5)	B (6)	m (7)	n (8)	P (9)	(10)
1	Breusers (6)	incipient motion	rational	1.40	0	0	0	0	0
1	Larras (16)	incipient motion	rational	1.426-1/4	0	0	0	0	0
II	Blench (5)	sediment transport	regime*	1.80	-1	3/4	0	1	0
11	Laursen (17) ^b	sediment transport	rational	1.11	0	1/2	0	0	0
11	Laursen and Toch (19)°	incipient motion	rational	1.35	0	0.3	0	0	0
11	Arunachalam (3)	sediment transport	regime*	1.95	-1	5/6	0	1	0
111	Ahmad (1)	sediment transport	regime	3.18K ^d	-1	1	2/3	1	0
III	Shen, et al. (28)	clear water	rational	11.00	0	1	2	0	0
V	Shen, et al. (28)	incipient motion	rational	3.40	0	1/3	2/3	0	0
V	Hancu (12)	incipient motion	rational	2.42	0	1/3	2/3	0	0
V	Inglis-Poona [Thomas, (29)]	incipient motion	rational	4.05	-1	3/4	1/2	1	0

[&]quot;y = regime depth.

been studied most extensively in laboratory experiments, from which several empirical formulas have been developed to estimate the maximum scour depths around bridge piers. In general, they are based upon a limited range of data and are applicable to conditions similar to those for which they were derived. It is difficult to confirm their adequacy for design purposes due to limited field measurements. Though there are some similarities among the various empirical relations, they differ widely in terms of the hydraulic variables considered to be significant. Most of the scour relations can be expressed in the form of the following general equation

^bTransformed and simplified by Melville (20).

^cTransformed and simplified by Neill (27).

d K = 1.2

in which d_s = the scour depth measured below mean bed elevation; y = the flow depth; $F = V/\sqrt{gy}$ = the Froude number; V = the flow velocity; b = the width of the pier projected on a plane normal to undisturbed flow; D

TABLE 2.—Scour Relations not Expressible in Form of Eq. 1

Group (1)	Investigator (2)	Regime (3)	Ap- proach (4)	Formula (5)	Remarks (6)
II	Breusers, et al. (7)	incipient motion	rational	$d_s/b = 2 \tanh (y/b)$	
Ш	Chitale (9)	clear water	rational	$d_s/y = (-0.51 + 6.65 F - 5.49 F^2)$	
IV	Inglis Lacey (13)	sediment trans- port	regime	$D_s = 0.946 \left(Q/f \right)^{1/3}$	D _s = scour depth below water surface Q = discharge, in cubic feet per second f = Lacey silt factor
					$= 1.76 \sqrt{D_{50}}$
	Knezvic (15)	clear water	rational	$d_{s} = 8.72 [(q - q')^{3/2}/y^{5/4}g^{3/4}]$	$q = vy$ $q' = q \text{ for } d_s = 0$
	Bata (4)	clear water	rational	$d_x/y = 10 [F^2 - 3D/y]$	
V	Maza (20)	clear water and sed- iment trans- port	rational	$d_z/b = f(F, y/b)$	graphical form
VI	Hancu (12)	clear water	rational	$d_s/b = 2.42 (2V/V_c - 1) F_c^{2/3} (y/b)^{1/3}$	$V_c = \text{threshold} \text{ velocity}$ $F_c = V_c / \sqrt{gy}$
	Garde (11)	-	rational	D_s/y = 4.0 $\eta_1 \eta_2 \eta_3 1/\alpha (F)^n$	$\alpha = (B - b)/B$ $B = \text{clear channel width}$ $\eta_1, \eta_2, \eta_3 \text{ and } n$ are functions of particle drag coefficient, Froude
	Chabert and Engel- dinger (8)	clear water and sed- iment transport	rational	$d_z = f(b, y, V, D)$	number, and pier shape graphical form

= the mean sediment size; A and B = constants; m, n, p, and r = exponents. The values of the constants A and B, and the exponents m, n, p, and r depend upon the pier shape, the angle of attack of the flow, and the sediment properties. Eq. 1 indicates that the scour depth is a function of four variables; the pier size, the flow depth, the flow velocity, and the sediment size. The values of the constants and exponents in Eq. 1 for circular piers based on the relations proposed by the various investigators are summarized in Table 1. There are

other empirical relations which could not be expressed in the form of Eq. 1; these are listed in Table 2.

The scour relations can be classified in several ways. They are grouped into six categories depending upon the number of significant hydraulic parameters in each relation. The only significant parameter is the pier size in group I; the flow depth and the pier size in group II; the flow depth and velocity in group III; the flow depth and velocity, and the sediment size in group IV; the flow depth and velocity, and the pier size in group V; all four parameters in group VI. The scour formulas are additionally classified into three groups based on the flow regimes; (1) Clear water; (2) incipient sediment motion; and (3) sediment transport regimes. The formulas for the condition of the incipient sediment motion predict the maximum clear-water scour which is assumed to occur at flow velocity approximately equal to the threshold velocity; therefore F in Eq. 1 should be replaced by the threshold Froude number, $F_c(F_c = V_c/\sqrt{gy})$, in which $V_c = 0$ the threshold velocity). The value of F in Eq. 1 for clear-water scour should be less than F_c . The empirical relations are categorized into two classes based on two different approaches; (1) Regime; and (2) rational approaches.

A comparison made by Anderson (2) of the several formulas listed in Tables 1 and 2 showed that the estimates of the relative scour depths differed widely, particularly for the higher values of Froude number and relative depth. The divergence among the curves representing the various scour formulas clearly indicated that most of these equations are applicable only for certain range of flow conditions and should not be extrapolated for flow conditions outside that range. A summary of the experimental data including the range of parameters used to develop the various scour formulas is presented elsewhere (14).

MAXIMUM CLEAR-WATER SCOUR

The dimensional analysis of the scouring parameters has been presented by several investigators including Breusers, et al. (7) and Neill (23). On the assumption that the influence of fluid viscosity on scour is negligible, the scour depth for natural sediments can be expressed as

$$\frac{d_s}{b} = f\left(\frac{y}{b}, F, \frac{D}{y}\right) \tag{2}$$

Furthermore, the relative sediment size, D/y, can be expressed as a function of threshold Froude number F_c using the logarithmic velocity distribution and the Shields' criterion for the initiation of sediment movement (see the curve in Fig. 2.46 of Ref. 30, labeled Shields), i.e.:

Eq. 2, after replacing D/y by F_c from Eq. 3, reduces to

$$\frac{d_s}{b} = f\left(\frac{y}{b}, \, F, F_c\right) \quad ... \quad (4)$$

The maximum clear-water scour occurs at $F = F_c$; Eq. 4 for $F \cong F_c$ can be simplified to

TABLE 3.—Summary of Data Used in Comparative Analysis

Flow velocity, in meters per second (1)	Pier diameter, in centi- meters (2)	Mean sediment size, in milli- meters (3)	Flow depth, in centi- meters (4)	Maximum scour depth, in centi- meters (5)	Thresh- old Froude number* (6)	Investigator (7)	
0.82	5.1	2.50	24.7	8.7	0.46	The writer and Fischer	
0.40	15.2	0.24	21.9	18.0	0.21	Shen, et al.	
0.32	15.2	0.24	11.6	13.4	0.27	Shen, et al.	
0.36	15.2	0.24	15.6	15.8	0.24	Shen, et al.	
0.38	15.2	0.24	20.6	17.1	0.22	Shen, et al.	
0.44	15.2	0.24	21.0	21.0	0.22	Shen, et al.	
0.41	15.2	0.24	26.3	18.6	0.20	Shen, et al.	
0.38	15.2	0.46	17.6	16.6	0.25	Shen, et al.	
0.50	91.4	0.46	61.0	54.9	0.15	Shen, et al.	
0.85	5.0	3.00	20.0	7.0	0.56	Chabert and Engeldinger	
0.85	10.0	3.00	20.0	12.5	0.56	Chabert and Engeldinger	
0.85	15.0	3.00	20.0	18.5	0.56	Chabert and Engeldinger	
0.76	5.0	3.00	10.0	8.7	0.71	Chabert and Engeldinger	
0.76	10.0	3.00	10.0	13.1	0.71	Chabert and Engeldinger	
0.76	15.0	3.00	10.0	17.5	0.71	Chabert and Engeldinger	
0.66	5.0	1.50	20.0	9.8	0.39	Chabert and Engeldinger	
0.66	10.0	1.50	20.0	17.0	0.39	Chabert and Engeldinger	
0.66	15.0	1.50	20.0	20.3	0.39	Chabert and Engeldinger	
0.40	5.0	0.52	19.7	9.5	0.25	Chabert and Engeldinger	
0.40	10.0	0.52	19.7	12.2	0.25	Chabert and Engeldinger	
0.40	15.0	0.52	19.7	14.9	0.25	Chabert and Engeldinger	
0.42	5.0	0.52	35.0	9.0	0.20	Chabert and Engeldinger	
0.42	10.0	0.52	35.0	12.0	0.20	Chabert and Engeldinger	
0.42	15.0	0.52	35.0	13.7	0.20	Chabert and Engeldinger	
0.37	10.0	0.52	10.0	11.5	0.32	Chabert and Engeldinge	

TABLE 3.—Continued

(1)	(2)	(3)	(4)	(5)	(6)	(7)
0.37	15.0	0.52	10.0	13.3	0.32	Chabert and Engeldinger
0.30	13.0	0.50	5.0	11.3	0.39	Hancu

*The value of F_c are based on the threshold velocity from the Shield's criterion for the critical shear stress and the logarithmic velocity distribution given by $V_c/V_{\bullet}=2.5$ In $(11.02~\rm yx/D_{50})$, when $V_{\bullet}=$ the critical shear velocity, and x= a correction factor accounting the effect of viscosity (30). A value of 0.01 cm²/s for the kinematic viscosity of water was assumed in the computation.

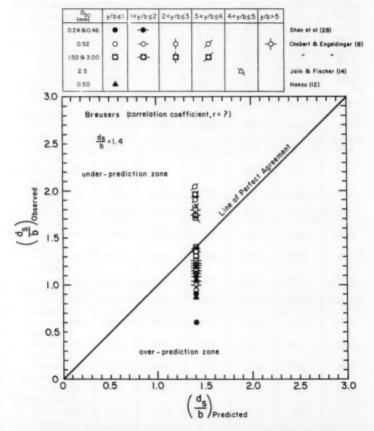


FIG. 1.—Comparison of Breusers' Formula with Available Scour Data

Only those predictors among the various formulas listed in Tables 1 and 2, which are in the form of Eq. 5, and based on rational approach, were selected for the comparative analysis.

Scour formulas based on "regime" approach used an empirical formula, derived mainly from canal data, relating the average stable channel depth of an alluvial channel to the dominant discharge and bed material. Some scour formula assumed that scour depths at structures could be expressed as some multiple of the average regime depth. These equations should be applied in cases in which

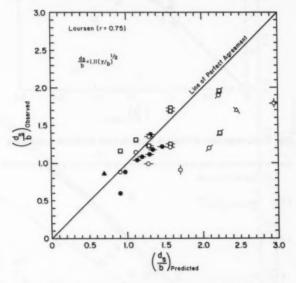


FIG. 2.—Comparison of Laursen's Formula with Available Data

the flow, sediment transport, and channel characteristics are quite similar to those from which the particular formula was derived. The equations based on "regime" approach are, therefore, not considered in the comparative analysis. Furthermore, the scour formulas which predict scour depth independent of pier size are applicable only for small values of the relative depth. These formulas, such as in groups III and IV in Tables 1 and 2, also are excluded from the comparative analysis due to their limited applications. Chabert and Engeldinger (8) did not propose any predictor for scour depth. Their experimental data are utilized in the analysis. The scour formulas of group V in Tables 1 and 2 are in the form of Eq. 5. This equation would be in accord with the scour formulas of group II if the influence of F_c on scour depth is found to be small.

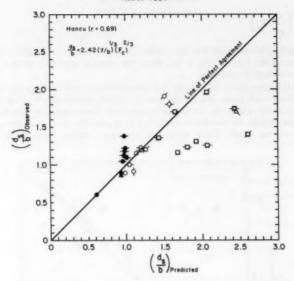


FIG. 3.—Comparison of Hancu's Formula with Available Scour Data

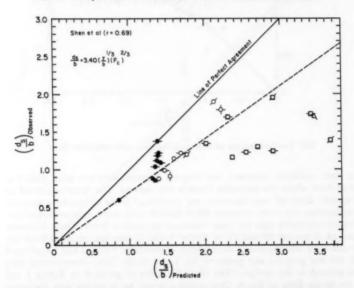


FIG. 4.—Comparison of Formula by Shen, et al. with Available Scour Data

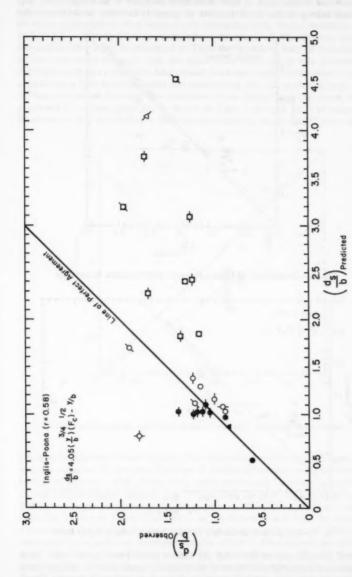


FIG. 5.—Comparison of Inglis-Poona's Formula with Available Scour Data

If the effect of the depth of flow in addition is found to be insignificant, Eq. 5 would belong to the scour formula of group I. In order to determine the

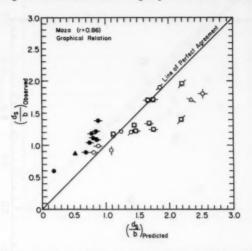


FIG. 6.—Comparison of Maza's Formula with Available Scour Data

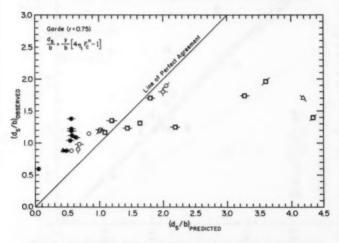


FIG. 7.—Comparison of Garde's Formula with Available Scour Data

range of flow parameters for which the various scour formulas are valid, these formulas are compared with some of the available scour data for circular piers. The experimental data of Chabert and Engeldinger (8), Shen, et al. (28), Hancu

(12), and the writer and Fischer (14) were used in the comparative analysis because all tests in these studies were conducted with circular cylinders and all basic experimental data were easily available. Only flow conditions with $0.02 < (F - F_c) < 0.1$ were included. A summary of experimental data in the comparative study is presented in Table 3. The lower limit of 0.02 instead of zero was used to insure that the equilibrium scour depth was achieved in the experiment in a reasonable long period; the scour depth in clear-water regime approaches a limit asymptotically and takes a long time to reach this limit.

The comparison between the observed scour depths and the scour depth predicted by various formulas is shown in Figs. 1 through 11. The values of linear correlation coefficient, r, between the observed and predicted scour depth

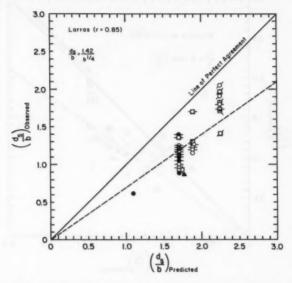


FIG. 8.—Comparison of Formula by Larras with Available Scour Data

are also included in these figures. The correlation coefficient indicates how well the equation fits the data. The lines of perfect agreement based on formulas by Larras, Breusers, et al., Shen, et al., and Laursen and Toch form an envelope for all data. Breusers' relation (Fig. 1) envelops the data for $(y/b) \le 3$ only and thus underpredicts scour depths for $(y/b) \ge 3$. The scour formula by Laursen is similar to that by Laursen and Toch as the former was derived by adjusting a constant in the solution for long constriction to agree with the latter. Laursen's relation (Fig. 2), however, underpredicts for $y/b \le 1$. The expressions by Shen, et al., and Hancu are identical except for the coefficient A (Eq. 1). Hancu's formula-(Fig. 3) with A = 2.42 seems to give the best fit for the data while Shen's formula (Fig. 4) with A = 3.40 envelops the data. Inglis-Poona's relation

(Fig. 5) is in agreement with data for fine sand ($D \lesssim 0.5$ mm) and $y/b \lesssim 4$. Maza graphical relation agrees well with the data (Fig. 6) except it does not envelop the data of Shen, et al., and Hancu for fine sand and low values of y/b. The scour formula by Garde underpredicts for fine sand and low values of y/b and overpredicts for coarse sand and high values of y/b, as shown in Fig. 7.

From design and safety considerations a predictor which envelops the experimental data is desirable. The formulas by Larras (Fig. 8), Breusers, et al. (Fig. 9), Shen, et al. (Fig. 4), and Laursen and Toch (Fig. 10) fall in this category. A regression analysis of the experimental data (14), based on the assumption

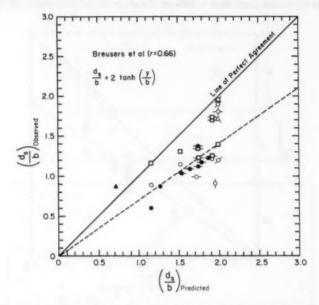


FIG. 9.—Comparison of Formula by Breusers, et al. with Available Scour Data

that the relative scour depth is a power function of the threshold Froude number and the relative depth, yielded

The coefficient 1.41 in Eq. 6 was increased by 30% to 1.84 in order to form an envelope for all data; it resulted in

$$\frac{d_s}{b} = 1.84 \left(\frac{y}{b}\right)^{0.30} (F_c)^{0.25}$$
 (7)

The comparison of Eqs. 6 and 7 with the data is presented in Fig. 11.

In order to determine the range of flow parameters for which the various formulas that envelope the experimental data, predict satisfactorily i.e., less overpredict, the following criterion was used. A formula was considered satisfactory if the difference between the predicted and observed values is less than 30% of the predicted value. The value of 30% was chosen because the constant 1.41 in Eq. 6 was increased by 30% to envelope the data. This criterion is represented by a dashed line in Figs. 4 and 8-11. This criterion is met by the formula of Breusers, et al. for coarse sand, Larras for $y/b \ge 3$, Shen, et al. for fine sand and $y/b \ge 1$, and Laursen and Toch for almost all of the data. It can, therefore, be inferred that the scour formula of Laursen and

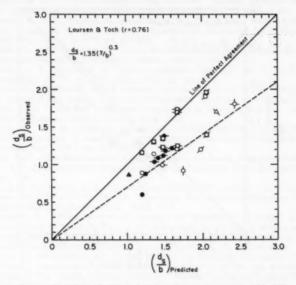


FIG. 10.—Comparison of Formula by Laursen and Toch with Available Scour Data

Toch and Eq. 7 are the best among these formulas to predict the maximum clear-water scour. The exponent of (y/b) in Eq. 7 is identical to that in the Laursen and Toch formula. These two formulas predict the same scour depth for $F_c = 0.29$. Eq. 7 for $F_c < 0.29$ predicts less scour depths than that given by Laursen and Toch formula. The following considerations show that Eq. 7 is a better predictor for the maximum clear-water scour than the Laursen and Toch formula. The laboratory experiments on local scour conducted recently by Ettema (10), Nicollet (24), and Hancu (12) indicate that the maximum clear-water scour depends upon the sediment size. Substituting for F_c from Eq. 3 in Eq. 7 shows that scour depth is a function of sediment size, while Laursen and Toch equation predicts that it is independent of sediment size.

The correlation coefficient for Eq. 7 is higher than that for Laursen and Toch relation. For most practical cases F_c is small and probably less than 0.3; Eq. 7 predicts less (therefore leading to an economical design) but safe (because it forms the envelope for all data) scour depth.

CONCLUSIONS

Several predictors for the maximum clear-water scour depth were compared with the available experimental data. The range of flow parameters for which these formulas either overpredicted or underpredicted were delineated. Predictors which enveloped all data were identified. The comparison indicated that the

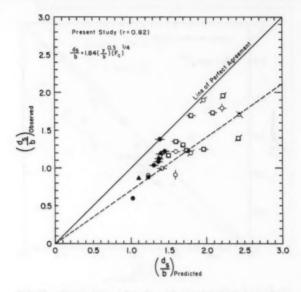


FIG. 11.—Comparison of Eqs. 6 and 7 with Available Scour Data

scour formula by Laursen and Toch (19) is the best predictor among those compared in this study, as it envelopes all data and overpredicts less than the other formulas. However, the Laursen and Toch formula predicts that the scour depth is independent of sediment size. Another formula (Eq. 7) for the maximum clear-water scour is proposed, which is very similar to that of Laursen and Toch but includes the effect of sediment size on scour depth.

ACKNOWLEDGMENT

This study was conducted for the Federal Highway Administration Office of Research Studies under the contract DOT-FH-11-7296.

APPENDIX 1.—REFERENCES

- Ahmad, M., discussion of "Scour at Bridge Crossings," by E. M. Laursen, Transactions, ASCE, Vol. 127, Part 1, 1962, pp. 198-206.
- Anderson, A. G., "Scour at Bridge Waterways—A Review," Report No. FHWA-RD-75-89, Federal Highway Administration, Washington, 1974.
- Arunachalam, K., "Scour around Bridge Piers," Journal of Indian Roads Congress, Paper No. 251, 1965.
- Bata, C., "Erozija oko novosadskog mostovskog stuba," (Serbian), (Scour around Bridge Piers), Institut za Vodoprivreder, Jaroslav Cerai Beozrod Yugoslavia, 1960; English translation by Markovic filed at Colorado State University, Ft. Collins, Colo.
- Blench, T., Mobile Bed Fluviology, University of Alberta Press, Edmonton, Alberta, Canada, 1969.
- Breusers, H. N. C., "Scour Around Drilling Platforms," Bulletin, Hydraulic Research 1965, International Association for Hydraulic Research, Vol. 19, 1965, p. 276.
- Bresuers, H. N. C., Nicollet, G., and Shen, H. W., "Local Scour Around Cylindrical Piers," *Journal of Hydraulic Research*, International Association for Hydraulic Research, Vol. 15, No. 3, 1977, pp. 211-252.
- Chabert, J., and Engeldinger, P., "Etude des affouillements autour des piles de ponts," Laboratoire National d'Hydraulique, Chatou, France, 1956.
- Chitale, S. V., discussion of "Scour at Bridge Crossings," by E. M. Laursen, Transactions, ASCE, Vol. 217, Part 1, 1962, pp. 191-196.
- Ettema, R., "Influence of Bed Material Gradation on Local Scour," Report No. 124, School of Engineering, University of Auckland, Auckland, New Zealand, 1976.
- Garde, R. J., "Local Bed Variation at Bridge Piers in Alluvial Channels," University of Roorke Research Journal, Vol. IV, India, 1961.
- Hancu, S., "Sur le Calcul des Affouillements Locaux dans la Zone des Piles du Pont," Proceedings of the 14th Congress, International Association for Hydraulic Research, Vol. 3, 1971, pp. 299-306.
- Inglis, C. C., "The Behaviour and Control of Rivers and Canals," Research Publication No. 13, pt. 2, Central Power, Irrigation and Navigation Report, Poona Research Station, India, 1949.
- Jain, S. C., and Fischer, E. E., "Scour Around Circular Piers at High Froude Numbers," Report No. FHWA-RD-79-104, U.S. Department of Transportation, Federal Highway Administration, Washington, D.C., April, 1979.
- 15. Knezevic, B., "Prilog proucavanju erozije oko mostoviskih stubova," (Serbian), (Contributions to Research Work of Erosion around Bridge Piers), Institut za Vodeprivredu Jaroslar Ceri Beograd, Yugoslavia, 1960; Translated by Markovic, filed at Colorado State University, Civil Engineering Department, Ft. Collins, Colo.
- Larras, J., "Profondeurs Maximales d'Erosion des Fonds Mobiles Autour des Piles en Rivier," Annales des Ponts et Chausses, Vol. 133, No. 4, 1963, pp. 411-424.
- Laursen, E. M., "Scour at Bridge Crossings," Bulletin No. 8, Iowa Highway Research Board, 1958.
- Laursen, E. M., "Scour at Bridge Crossings," Transactions, ASCE, Vol. 127, Part 1, 1962, pp. 166-179.
- Laursen, E. M., and Toch, A., "Scour around Bridge Piers and Abutments," Bulletin No. 4, Iowa Highway Research Board, 1956.
- Maza Alvarex, J. A., "Scour in River-Beds," Instituto de Ingenieria, Universidad Nacional Autonoma de Mexico, Ciudad Universitaria, Mexico, 1977.
- Melville, B. W., "Local Scour at Bridge Sites," Report No. 117, School of Engineering, University of Auckland, Auckland, New Zealand, 1975.
- Neill, C. R., "Local Scour around Bridge Piers," Highway and River Engineering Division, Research Council of Alberta, Canada, 1964.
- Neill, C. R., discussion on "Local Scour around Bridge Piers," by When, Scheider and Karaki, Journal of the Hydraulics Division, ASCE, Vol. 96, No. HY5, 1970.
- 24. Nicollet, G., "Deformation des Lits Alluvionnaires; Affouillements Autour des Piles de Ponts Cylindriques," Laboratoire Nacional d'Hydraulique, Chatou, France, 1971.
- Posey, C. J., "Why Bridges Fail in Floods," Civil Engineering, Vol. 19, 1949, pp. 42-90.

- Roper, A. T., Schneider, V. R., and Shen, H. W., "Analytical Approach to Local Scour," Proceedings of the XII Congress of IAHR, Vol. 3, Ft. Collins, Colo., 1967, pp. 151-167.
- pp. 151-167.
 "Scour at Bridge Waterways," Synthesis Report No. 5 of Highway Practice, National Cooperative Highway Research Program, 1970.
- 28. Shen, H. W., Scheider, V. R., and Karaka, S., "Local Scour around Bridge Piers," Journal of the Hydraulics Division, ASCE, Vol. 95, No. HY6, 1969.
- Thomas, A. R., discussion of "Scour at Bridge Crossings," by E. M. Laursen, Transactions, ASCE, Vol. 127, PE 1, 1962, pp. 196-198.
- Vanoni, V. A., Editor, Sedimentation Engineering, ASCE—Manual and Reports on Engineering Practice, No. 54, American Society of Civil Engineers, New York, N.Y., 1975.

APPENDIX II.—NOTATION

The following symbols are used in this paper:

- A.B = constants:
 - b = pier size:
 - D = mean sediment diameter:
 - $d_{\cdot} = \text{scour depth};$
 - $F = V/\sqrt{gy} = Froude number;$
 - $F_c = V_c / \sqrt{gy} =$ threshold Froude number;
- g = gravitational constant;
- m, n, p, r =exponents;
 - V = mean flow velocity;
 - V_c = threshold velocity; and
 - v = flow depth.

TECHNICAL NOTES

Note.—Discussion open until October 1, 1981. To extend the closing date one month, a written request must be filed with the Manager of Technical and Professional Publications, ASCE. This paper is part of the Journal of the Hydraulics Division, Proceedings of the American Society of Civil Engineers, ©ASCE, Vol. 107, No. HY5, May, 1981.

TECHNICAL NOTES

To provide a place within ASCE for publication of technical ideas that have not advanced, as yet, to the point where they warrant publication as a Proceedings paper in a *Journal*, the publication of Technical Notes was authorized by the Board of Direction on October 16-18, 1967, under the following guidelines:

- 1. An original manuscript and two copies are to be submitted to the Manager of Technical and Professional Publications, ASCE, 345 East 47th Street, New York, N.Y., 10017, along with a request by the author that it be considered as a Technical Note.
 - 2. The two copies will be sent to an appropriate Technical Division or Council for review.
- 3. If the Division or Council approves the contribution for publication, it shall be returned to Society Headquarters with appropriate comments.
- 4. The technical publications staff will prepare the material for use in the earliest possible issue of the *Journal*, after proper coordination with the author.
- Each Technical Note is not to exceed 4 pages in the Journal. As an approximation, each full manuscript page of text, tables, or figures is the equivalent of one-half a Journal page.
 - 6. The Technical Notes will be grouped in a special section of each Journal.
 - 7. Information retrieval abstracts and key words will be unnecessary for Technical Notes.
- 8. The final date on which a Discussion should reach the Society is given as a footnote with each Technical Note.
 - 9. Technical Notes will not be included in Transactions.
- 10. Technical Notes will be included in ASCE's annual and cumulative subject and author indexes.

The manuscripts for Technical Notes must meet the following requirements:

- 1. Titles must have a length not exceeding 50 characters and spaces.
- The author's full name, Society membership grade, and a footnote reference stating present employment must appear on the first page of the manuscript. Authors need not be Society members.
- 3. The manuscript is to be submitted as an original copy (with two duplicates) that is typed double-spaced on one side of 8-1/2-in. (220-mm) by 11-in. (280-mm) white bond paper.
- 4. All mathematics must be typewritten and special symbols must be properly identified. The letter symbols used must be defined where they first appear, in figures or text, and arranged alphabetically in an Appendix.—Notation.
- 5. Standard definitions and symbols must be used. Reference must be made to the lists published by the American National Standards Institute and to the Authors' Guide to the Publications of ASCE.
- 6. Tables must be typed double-spaced (an original ribbon copy and two duplicate copies) on one side of 8-1/2-in. (220-mm) by 11-in. (280-mm) paper. An explanation of each table must appear in the text.
- 7. Figures must be drawn in black ink on one side of 8-1/2-in. (220-mm) by 11-in. (280-mm) paper. Because figures will be reproduced with a width of between 3 in. (76 mm) to 4-1/2 in. (110 mm), the lettering must be large enough to be legible at this width. Photographs must be submitted as glossy prints. Explanations and descriptions must be made within the text for each figure.
- 8. References cited in text must be typed at the end of the Technical Note in alphabetical order in an Appendix.—References.
- 9. Dual units, i.e., U.S. Customary followed by SI (International System) units in parentheses, should be used throughout the paper.

BIOFILM GROWTH AND HYDRAULIC PERFORMANCE

By Brian Butterworth¹

Rheidol is a 56-MW hydroelectric station operated by the Central Electricity Generating Board (of England) in mid Wales; its scheme is shown in Fig. 1. Both the low-pressure NANT-Y-MQCH to DINAS and the higher-pressure DINAS to CWM RHEIDOL tunnels have suffered biofouling and its attendant loss of hydraulic performance.

The problem first manifested itself in the higher pressure tunnel, as a steady decline in the maximum power output. Twelve years after commissioning, this deficit had reached 10%, and was showing signs of a steadily increasing rate of deterioration.

Detailed performance testing of the plant showed the turbines and generators to be performing as designed, while the pipeline exhibited a frictional head loss some 44% greater than design.

Internal inspection of the pipeline revealed a layer of material some 4.5 mm thick, which was extremely hard and knobbly when wet (see Fig. 2); the material became soft and friable when dry. Analysis of the deposit showed a very high iron and manganese content, as well as organic material: SiO₂—30.9%; loss on ignition at 800° C—30.2%; Zn—0.5%; Fe—6.9%; Pb—1.2%; and Mn—19.0%. The organic material was largely fibrous vegetable matter, of which peat was the main constituent.

Subsequent cleaning of the whole tunnel, with high-pressure water jets, recovered the major proportion of the deficit (see Fig. 3). The whole of the deficit was not recovered because free carbon dioxide, present in the water during normal operation, had removed lime from the concrete lining causing residual hydrated silica particles to flake off under the action of water jetting. The resultant surface was somewhat rougher than the original "shuttered concrete" finish.

Normal generation over the next 18 months produced a still further reduction in the head loss due to friction. The two mechanisms responsible for this phenomenon are: (1) Grit, normally present in the water, acting as an abrasive

¹Research Officer, Scientific Services Dept. (North Western Region), Central Electricity Generating Board, Europa House, Bird Hall Lane, Cheadle Heath, Stockport, Cheshire SK2 OKA England.

Note.—Discussion open until October 1, 1981. To extend the closing date one month, written request must be filed with the Manager of Technical and Professional Publications, ASCE. Manuscript was submitted for review for possible publication on October 17, 1980. This paper is part of the Journal of the Hydraulics Division, Proceedings of the American Society of Civil Engineers, ©ASCE, Vol. 107, No. HY5, May, 1981. ISSN 0044-796X/81/0005-0629/\$01.00.

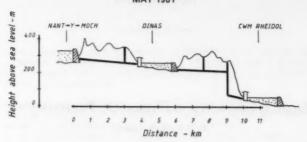


FIG. 1.—Rheidol Hydroelectric Project: Schematic

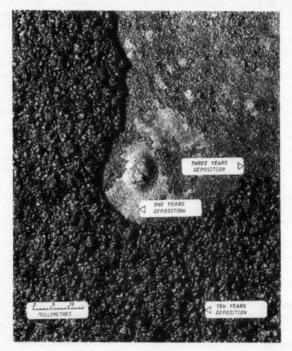


FIG. 2.—Biofilm

to smooth the concrete; and (2) the "peat" starting to reattach as a slime, "filling-in" and, thus, smoothing some of the hollows.

Annual monitoring of the reappearance of the deposit has produced data on the rate of the deposition and a correlation between deposit thickness and

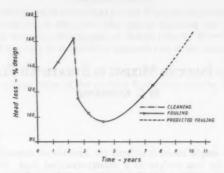


FIG. 3.—Friction Head Loss as Function of Time

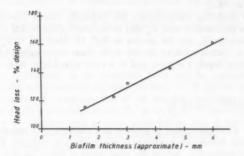


FIG. 4.—Friction Head Loss as Function of Biofilm Thickness

head loss (see Fig. 4). Additionally, we are now able to predict the optimum cleaning frequency for maximum generation, some 7 yr-8 yr.

WIND-INDUCED MIXING IN STRATIFIED FLUID

By C. Kranenburg¹

INTRODUCTION

In this note a simple model is offered for mixed-layer deepening caused by wind action at the free surface of a density-stratified fluid. Solar radiation, cooling, advection, and Coriolis effects are not considered. To include an aspect of mixing in waters of limited horizontal extent, a streamwise pressure gradient is taken into account.

On certain modeling assumptions, the turbulent energy equation yields a dimensionless entrainment rate E_{\star} that is inversely proportional to the overall Richardson number R_i, see the review in Ref. 15. Here $E_{\star} = u_{\star}^{-1} dH/dt$, R_i = B/u_{\star}^2 ; u_{\star} = friction velocity related to the shear stress exerted by the wind; H = mixed-layer depth; t = time; and B = total mixed-layer buoyancy defined by

in which g = acceleration due to gravity; $\rho =$ density; $\rho =$ reference density; and z = vertical downward coordinate (z = 0 at the free surface). The subscript ρ refers to the initial (i.e., before the wind starts to blow) density distribution. Of the foregoing modeling assumptions, the central one, namely, that the net kinetic-energy input is proportional to u_{\bullet}^3 , has been criticized (14,18).

A different assumption was put forward by Pollard, et. al (11). These authors assumed another overall Richardson number, R_{iU} , to be constant. Here R_{iU} = B/U^2 and U = mean mixed-layer velocity; A constant R_{iU} implies $E_{\bullet} \propto R_i^{-1/2}$. Price (12) re-examined the experiments of Kato and Phillips (6) (linear initial density distribution), and Kantha, et. al (5) (two-layer fluid) introducing a correction for side-wall friction. Prices' analysis of these experiments led to an almost constant R_{iU} at larger values of $R_{i\bullet}$ ($R_{iU} = 0.6$, experimental scatter in the range $0.5 < R_{iU} < 0.8$), in agreement with Ref. 14.

An explanation of these findings is given herein starting from a two-layer structure of the mixed layer: a homogeneous upper layer in which stratification effects are disregarded, and a lower transition layer where near-critical conditions

^{&#}x27;Sr. Scientific Officer, Lab. of Fluid Mechanics, Dept. of Civ. Engrg., Delft Univ. of Tech., Stevinweg 4, 2628 CN Delft, The Netherlands.

Note.—Discussion open until October 1, 1981. To extend the closing date one month, a written request must be filed with the Manager of Technical and Professional Publications, ASCE. Manuscript was submitted for review for possible publication on June 4, 1980. This paper is part of the Journal of the Hydraulics Division, Proceedings of the American Society of Civil Engineers, ©ASCE, Vol. 107, No. HY5, May, 1981. ISSN 0044-796X/81/0005-0632/501.00.

(i.e., the turbulence is nearly collapsing) prevail. Experimental evidence indicating near-critical conditions in this layer (the region including the thermocline) is provided by the revealing photographs of Woods (19), by Wyatt (21) and Price (13); also see Kundu (8). It is therefore assumed that in the transition layer

in which Ric = critical value of the gradient Richardson number R,

in which u = horizontal velocity component; and overbars indicate variables averaged for turbulence. The full-scale measurements reported in Ref. 13 strongly support the assumption of a homogeneous upper layer. Apart from the influence of the Coriolis force, possible processes contributing to the homogeneity are: shear-induced mixing (see Ref. 8 for comparison), wave-induced mixing and Langmuir circulations.

ANALYTICAL DEVELOPMENT

The density distribution in the transition layer will be assumed linear, as suggested by the measurements reported in Ref. 13. It can be shown using elementary calculus of variations that of all possible distributions, the linear one yields the smallest entrainment rate (for given depth of the transition layer). The relevance of this fact will become clear below. Eq. 3 then shows that the velocity profile in the transition layer becomes linear also.

The balance of mass reads

$$\frac{1}{2}(H+h)\Delta\rho = \int_{0}^{H} \left[\rho_{o}(H) - \rho_{o}(z)\right] dz \qquad (4)$$

in which h = depth of homogeneous layer. Adopting the Boussinesq approximation, the balance of horizontal momentum becomes

in which $\partial \bar{p}/\partial x=$ streamwise pressure gradient; and $u_h=$ additional velocity in the homogeneous layer $[\bar{u}=\Delta u+u_h]$ and $u_h(h,t)=0$]. The undisturbed layer is assumed to be deep and nonturbulent. Eqs. 1, 2, 3, and 4 yield

$$\frac{\Delta u}{u_{\pm}} = \sqrt{2 \frac{R_i}{R_{ic}} \frac{H - h}{H + h}}$$
 (6)

The positive root chosen in Eq. 6 requires the right side of Eq. 5 to be positive. Eliminating Δu between Eqs. 5 and 6 gives

$$\frac{d}{dt} \left[u_* \sqrt{R(H^2 - h^2)} + h \int_0^1 u_h(\eta) \, d\eta \right] = u_*^2 (1 - \gamma) \quad ... \quad (7)$$

in which R = 1/2 (R_i/R_{ic}); and $\eta =$ dummy variable. For simplicity it has been assumed in Eq. 7 that $u_h(z,t)$ can be written as $u_h(z/h)$. The pressure-gradient parameter γ is defined by

$$\gamma = \frac{H}{\rho_{\nu} u_{-}^{2}} \frac{\partial \bar{p}}{\partial x} \qquad (8)$$

In the case of pure setup without horizontal circulation, γ would be unity.

Although it is possible to include arbitrary time dependence of u_{\bullet} in the analysis, the friction velocity will be assumed zero for t < 0 and constant for t > 0 from now on. Integrating Eq. 7 then gives [H(0) = 0]

$$\sqrt{R(H^2-h^2)} + \alpha^{-1}h = u_{\bullet}(1-\gamma)t$$
(9)

Eq. 9 shows that α is related to the entrainment rate in the absence of stratification (R = 0, h = H)

Obviously, a may be a function of y.

Using the turbulence kinetic energy equation, it can be shown that h must go to zero for R tending to infinity. Eq. 9 then gives $H\sqrt{R} = u_* (1 - \gamma)$ t, or upon differentiation (note that in general R depends on H)

$$E_* = \frac{1 - \gamma}{\frac{d}{dH}(H\sqrt{R})}; \quad R \to \infty$$
 (12)

Eqs. 9, 11, and 12 indicate zero entrainment rates for $\gamma=1$ (the case $\gamma>1$ has already been excluded). The simple shear-flow model does not hold in this case, however, since the velocity gradient $\partial \bar{u}/\partial z$ becomes zero at some depth. Diffusion of turbulence kinetic energy should then be considered to obtain nonzero entrainment rates. Nevertheless, the very small entrainment rates observed by Wu (20), Delft Hydraulics Laboratory (2) and Kit, et al. (7) for $\gamma=1$ and by Imberger, et al. (3) for a reservoir indicate that the model presented to some extent correctly reproduces the influence of a streamwise pressure gradient.

Apart from the special cases R = 0 and $R \to \infty$, the depth, h, of the homogeneous layer has not been specified. A minimal depth, h_m , of the mixed layer can be derived from Eq. 9 by taking H as a function of h and letting $\partial H/\partial h = 0$, while keeping time t fixed. The results are (subscript m refers to the minimum)

$$H_{m} = \frac{u_{*}(1-\gamma)t}{\sqrt{\alpha^{-2}+R}}$$
 (13)

Price (13) and Kundu (8) report larger depths h than given by Eq. 14. The actual entrainment rates will therefore be larger than minimal. Eq. 13 represents an absolute minimum for the layer model elaborated, because of the linear

density profile assumed for the transition layer.

In practical situations R is a large number ($R_i > 50$, for instance). Adopting $\alpha \simeq 0.28$ (16), which may be on the large side (1), and $R_{ic} = 0.25$ (13,17) gives $\alpha^{-2}/R < 0.128$. Neglecting α^{-2} in Eq. 13 therefore causes a 6% error or less, and differentiating Eq. 13 then again yields Eq. 12. The actual entrainment rate may be expected to be less than predicted by Eq. 12, because of the restriction at zero R (according to this equation e_* would increase undefinitely for R tending to zero). Since practically the difference between Eqs. 12 and 13 is small, Eq. 12 is considered a good approximation. Note that in general the entrainment rate is not a simple function of R (or R_i). The exceptions to this result are considered in the following section.

Neglecting h with respect to H (as in Eq. 12), the overall Richardson number R_{tt} becomes proportional to R_{tc} . For the linear profiles assumed one obtains

$$R_{iU} = 2 R_{ic} (15)$$

It is noted that R_{tU} does not depend on the density structure of the undisturbed layer and on $\gamma(\gamma < 1)$. Assuming $R_{tc} \simeq 0.25$ (the theoretical value) to 0.3 (15), Eq. 15 gives $R_{tU} \simeq 0.5$ -0.6. These values are close to those indicated in Refs. 12 and 13.

Homogeneous Undisturbed Layer.—In this case B and therefore R are constant. Eq. 12 then gives

$$E_* = \frac{1 - \gamma}{\sqrt{R}} \tag{16}$$

or $E_{\star} \simeq 0.71/\sqrt{R_{i}}$ for $R_{ic} = 0.25$ and $\gamma = 0$. On examination, this result is found to agree with the experiments of Kantha, et al. (5) up to $R_{i} \simeq 200$. At larger R_{i} the observed entrainment rates drop off. As the authors report, this may be caused by molecular effects. Also see Ref. 12 for the influence of side-wall friction.

Initial Density Distribution According to Power Law .- In the case where

in which c, $\beta = \text{constants } (\beta > -1, c\beta > 0)$, Eq. 12 yields

$$E_* = \frac{2}{\beta + 3} \frac{1 - \gamma}{\sqrt{R}} \tag{18}$$

Comparing Eqs. 16 and 18, the entrainment rate in the case of a linear initial density distribution ($\beta=1$) is only half that for a homogeneous lower layer. As noted by Price (12) this result agrees, at least qualitatively, with observations. The difference has sometimes been attributed to radiation of internal waves in the linearly stratified case (4). The foregoing analysis corroborates that the density distributions alone can cause the difference. The linear density profile assumed for the transition layer may be unrealistic if $\beta=1$. Different profiles would yield only slightly different entrainment rates, however. A distribution according to a parabola with apex at z=0, for instance, would give R=1

12/25 (R₁/R_{1c}) instead of R = 1/2 (R₁/R_{1c}). A comparison between Eq. 18 ($\beta = 1$, $\gamma = 0$, R_{1c} = 0.25) and the experimental results of Katho and Phillips (6) is extrapolated by Price (12) to zero aspect (depth to width) ratio. The agreement is satisfactory, although the experimental scatter is considerable.

CONCLUDING REMARKS

The result of Eqs. 16 and 18, namely that E_{\star} is proportional to $(1-\gamma)(\mathsf{R}_{ic}/\mathsf{R}_i)^{1/2}$, can be shown to hold for more general density and velocity profiles by using an order of magnitude argument: integrating Eq. 5 gives $HU = u_{\star}^2(1-\gamma)t$; assuming in Eq. 3 that $\partial \bar{\rho}/\partial z \sim \Delta \rho/H$ and $\partial \bar{u}/\partial z \sim U/H$ gives $E_{\star} = H/(u_{\star}t) \sim (1-\gamma)(\mathsf{R}_{ic}/\mathsf{R}_i)^{1/2}$, and, as was to be expected, $\mathsf{R}_{iU} \sim \mathsf{R}_{ic}$.

Eq. 15 indicates that $R_{iU} < 1$, R_{ic} being certainly less than 0.5. The flow in the mixed layer therefore is supercritical. Entrainment rates in subcritical flows will be less than found herein, since subcritical flows seem to be essentially more stable. The experiments of Lofquist (9) and most of the experiments of Moore and Long (10), for instance, are concerned with subcritical flows.

APPENDIX. - REFERENCES

 Csanady, G. T., "A Developing Turbulent Surface Shear Layer Model, "Journal of Geophysical Research," Vol. 84, No. C8, 1979, pp. 4944-4948.

 Delft Hydraulics Laboratory, "Menging bij een Twee-Lagen-Systeem Veroorzaakt door Wind," Report No. M1235, (in Dutch), Delft, The Netherlands, 1974.

 Imberger, J., Patterson, J., Hebbert, R. H. B., Loh, I., "Dynamics of Reservoir of Medium Size," *Journal of the Hydraulics Division*, ASCE, Vol. 104, No. HY5, Proc. Paper 13773, May, 1978, pp. 725-743.

 Kantha, L. H., "Note on the Role of Internal Waves in Thermocline Erosion," Modelling and Prediction of the Upper Layers of the Ocean, E. B. Kraus, ed., Pergamon,

Oxford, England, 1977, pp. 173-177.

 Kantha, L. H., Phillips, O. M., and Azad, R. S., "On turbulent Entrainment at a Stable Density Interface," *Journal of Fluid Mechanics*, Vol. 79, No. 4, 1977, pp. 743-768.

Kato, H., and Phillips, O. M., "On the Penetration of a Turbulent Layer into Stratified Fluid," *Journal of Fluid Mechanics*, Vol. 37, No. 4, 1969, pp. 643-655.
 Kit, E., Berent, E., and Vajda, M., "Vertical Mixing Induced by Wind and a Rotating

 Kit, E., Berent, E., and Vajda, M., "Vertical Mixing Induced by Wind and a Rotating Screen in a Stratified Fluid in a Channel," *Journal of Hydraulic Research*, Vol. 18, No. 1, 1980, pp. 35-58.

 Kundu, P. K., "A Numerical Investigation of Mixed-Layer Dynamics," Journal of Physical Oceanography, Vol. 10, No. 2, 1980, pp. 220-236.

 Lofquist, K., "Flow and Stress near an Interface between Stratified Liquids," The Physics of Fluids, Vol. 3, No. 2, 1960, pp. 158-175.

- Moore, M. J., and Long, R. R., "An Experimental Investigation of Turbulent Stratified Shearing Flow," *Journal of Fluid Mechanics*, Vol. 49, No. 4, 1971, pp. 635-655.
 Pollard, R. T., Rhines, P. B., and Thompson, R. O. R. Y., "The Deepening of
- the Wind-Mixed Layer," Geophysical Fluid Dynamics, Vol. 3, 1973, pp. 381-404.

 12. Price, J. F., "On the Scaling of Stress-Driven Entrainment Experiments," Journal
- of Fluid Mechanics, Vol. 90, No. 3, 1979, pp. 509–529.

 Price, J. F., "Observations of a Rain-Formed Mixed Layer," Journal of Physical Oceanography, Vol. 9, No. 3, 1979, pp. 643-649.

 Price, J. F., Mooers, C. N. K., and Van Leer, J. C., "Observations and Simulation of Storm-Driven Mixed-Layer Deepening," *Journal of Physical Oceanography*, Vol. 8, No. 4, pp. 582-599.

 Sherman, F. S., Imberger, J., and Corcos, G. M., "Turbulence and Mixing in Stably Stratified Waters," Annual Review of Fluid Mechanics, Vol. 10, 1978, pp. 267-288.

- Tennekes, H., and Lumley, J. L., A First Course in Turbulence, MIT Press, Cambridge, Mass., 1972, p. 192.
- Turner, J. S., "Buoyancy Effects in Fluids," Cambridge University Press, Cambridge, United Kingdom, 1973, pp. 97-107.
- Dynamics of Stratification and of Stratified Flow in Large Lakes, A. E. P. Watson, ed., International Joint Commission, Great Lakes Regional Office, Windsor, Ontario, Canada, 1976.
- Woods, J. D., "Wave-Induced Shear Instability in the Summer Thermocline," Journal of Fluid Mechanics, Vol. 32, No. 4, 1968, pp. 791-800.
- Wu, J., "Wind Induced Turbulent Entrainment across a Stable Density Interface," Journal of Fluid Mechanics, Vol. 61, No. 2, 1973, pp. 275-287.
- Wyatt, L. R., "The Entrainment Interface in a Stratified Fluid," Journal of Fluid Mechanics, Vol. 86, No. 2, 1978, pp. 293-312.



DISCUSSION

Note.—This paper is part of the Journal of the Hydraulics Division, Proceedings of the American Society of Civil Engineers, @ASCE, Vol. 107, No. HY5, May, 1981. ISSN 0044-796X/81/0005-0641/\$01.00.

DISCUSSIONS

Discussions may be submitted on any Proceedings paper or technical note published in any Journal or on any paper presented at any Specialty Conference or other meeting, the Proceedings of which have been published by ASCE. Discussion of a paper/technical note is open to anyone who has significant comments or questions regarding the content of the paper/technical note. Discussions are accepted for a period of 4 months following the date of publication of a paper/technical note and they should be sent to the Manager of Technical and Professional Publications, ASCE, 345 East 47th Street, New York, N.Y. 10017. The discussion period may be extended by a written request from a discusser.

The original and three copies of the Discussion should be submitted on 8-1/2-in. (220-mm) by 11-in. (280-mm) white bond paper, typed double-spaced with wide margins. The length of a Discussion is restricted to two Journal pages (about four typewritten double-spaced pages of manuscript including figures and tables); the editors will delete matter extraneous to the subject under discussion. If a Discussion is over two pages long it will be returned for shortening. All Discussions will be reviewed by the editors and the Division's or Council's Publications Committees. In some cases, Discussions will be returned to discussers for rewriting, or they may be encouraged to submit a paper or technical note rather than a Discussion.

Standards for Discussions are the same as those for Proceedings Papers. A Discussion is subject to rejection if it contains matter readily found elsewhere, advocates special interests, is carelessly prepared, controverts established fact, is purely speculative, introduces personalities, or is foreign to the purposes of the Society. All Discussions should be written in the third person, and the discusser should use the term "the writer" when referring to himself. The author of the original paper/technical note is referred to as "the author."

Discussions have a specific format. The title of the original paper/technical note appears at the top of the first page with a superscript that corresponds to a footnote indicating the month, year, author(s), and number of the original paper/technical note. The discusser's full name should be indicated below the title (see Discussions herein as an example) together with his ASCE membership grade (if applicable).

The discusser's title, company affiliation, and business address should appear on the first page of the manuscript, along with the *Proceedings* paper number of the original paper/technical note, the date and name of the *Journal* in which it appeared, and the original author's name.

Note that the discusser's identification footnote should follow consecutively from the original paper/technical note. If the paper/technical note under discussion contained footnote numbers 1 and 2, the first Discussion would begin with footnote 3, and subsequent Discussions would continue in sequence.

Figures supplied by the discusser should be designated by letters, starting with A. This also applies separately to tables and references. In referring to a figure, table, or reference that appeared in the original paper/technical note use the same number used in the original.

It is suggested that potential discussers request a copy of the ASCE Authors' Guide to the Publications of ASCE for more detailed information on preparation and submission of manuscripts.

UNCERTAINTY IN STEP-BACKWATER PROFILES^a Closure by Asok Motayed⁵ and David R. Dawdy,⁶ Members, ASCE

The writers thank Bradley and Eriksen for setting the record straight by pointing out that the step-backwater programs analyzed were "standard step" not "direct step." This indeed eliminated the need for inclusion of an errata to this closure.

To minimize the effects of starting elevation on a study reach, extension of study reach downstream, as proposed by the discussers, is a commonly used procedure in backwater analysis and was performed by the writers in the course of this study. Water surface elevations obtained through such techniques were reasonably close to the results of the trial and error method. This is expected, since once the effect of the arbitrary starting water surface elevation is dissipated over a long reach, the only difference expected to remain between the profiles would be that due to inherent differences between the computer programs.

The writers fully agree that the bridge loss computation procedures of different programs are likely to be the most important difference between the programs. The purpose of this paper, however, was not to enumerate the differences between the three programs, per se. It was to examine the inherent uncertainties associated with other factors. Therefore, purposefully, the difference in water surface elevations caused by different bridge loss computational techniques was avoided by selecting a reach without any bridge. The major question raised in and the conclusion drawn from the study was that even when all other external factors like starting water surface elevations, bridge loss computation, etc. are eliminated, step-backwater analyses by the three well-known and commonly used computer programs contain uncertainties just because of the different computational techniques used in solving the same equation of flow.

^aMay, 1979, by Asok Motayed and David R. Dawdy (Proc. Paper 14555).

⁵Vice Pres., Sheladia Assoc., Inc., Consulting Engrs., 5711 Sarvis Ave., Riverdale, Md. 20840.

⁶Sr. Hydro., Dames and Moore, Bethesda, Md.

OPEN CHANNEL FLOW WITH VARYING BED ROUGHNESS a Closure by Donald W. Knight, and J. Alasdair Macdonald 10

The writers would like to thank the various discussers for their valuable comments. They agree with Nandana Vittal, M.S. Verma, and K. G. Ranga Raju that the division of the cross-sectional area into subareas using isovel patterns is somewhat arbitrary. What data there is for three-dimensional flow in a corner (15,23,30,31) strongly suggests that the isovel pattern is significantly affected by the presence of secondary motions. These secondary flows are of course intimately related to the distribution of Reynolds and normal stresses in the cross section. Although these secondary flows are relatively small, their influence upon the turbulence structure and isovel pattern is large. It therefore follows that theoretical models based upon the assumption of one-dimensional flow, as most current sidewall correction procedures are, must be less than satisfactory in describing a three-dimensional phenomenon. The issue is further complicated by the absence of any sound theory accounting for influences of geometry (cross-sectional shape) and varying boundary roughness (composite roughness). One of the ancillary purposes in publishing the original data was to highlight the deficiencies in one of the more popular sidewall correction procedures. Fig. 11 adequately shows this point.

Referring to the correction procedures of Einstein and Vanoni and Brooks, the data presented in Fig. 13 do not appear to support the discussers' statement that "In general, the measured shears are smaller and the difference between the measured and computed values does not show any systematic variation with B/h." The agreement is certainly poor, but particularly so for low B/h values (B/h < 5). There appears to be a systematic deviation in the results for low B/h values which arises from the three-dimensionality of the flow, and this is not surprising in the light of comments made earlier. Taking a smooth rectangular channel as an example, it may be shown that the percentage of the shear force carried by the walls, increases markedly at low B/h values. (Typically SF_W as a percentage varies from 25% at B/h = 5-70% at B/h = 1.) It is therefore at these low B/h values that the various sidewall correction procedures are best tested.

The new sidewall correction procedure proposed by Nandana Vittal, M. S. Verma, and K. G. Ranga Raju based upon the dimensionless group $\bar{u}B/\nu$ appears to offer an interesting line of enquiry. The writers are pleased to see that their resistance data, when plotted in the form of Fig. 14, appears to fit smoothly in with other data. This highlights the value of presenting data in tabular form

^{*}September, 1979, by Donald W. Knight and J. Alasdair Macdonald (Proc. Paper 14839).
*Lect., Civ. Engrg. Dept., Univ. of Birmingham, P.O. Box 363, Birmingham B15 2TT, England.

¹⁰ Asst. Engr., Soar Div., Severn Trent Water Authority, Leicester, England.

in published papers. However, as to the universality of this new approach, the writers would add a word of caution in the light of earlier comments. It is difficult to accept that f_w depends upon $\bar{u}B/\nu$ in the manner shown for all possible ratios of bed to wall roughness. Indeed some of the scatter in Fig. 14 may result from mixing the smooth wall, smooth bed results with the smooth wall, rough bed results. Because the legend does not give any details it is not possible to draw any firm conclusions. The fact that the Vanoni-Brooks method gives comparable results to the new method (Fig. 15) does not in itself constitute a rigorous validation unless it is shown that the earlier method is itself correct, particularly at low B/h values. However the writers are grateful to the discussers for having drawn their attention to this new approach, which will be examined further.

The comments by Peter R. Wormleaton, John Allen, and Panos Hadijpanas regarding the Preston tube are helpful and correct. When the flume experiments were undertaken. Preston's original calibration curve was employed, although Patel's criticisms of the original calibration were known. It was decided to check the overall shear stress values in the way described in the original paper. using both energy slope and velocity readings. The errors shown in Fig. 2(b) indicate that the agreement between the various methods was reasonable but by no means perfect. The in situ calibration of the Preston Tube was therefore accepted as being reasonable in the light of a mean τ_0/τ_e value of 0.976 for all 50 experiments, and a variation of 0.927-1.100 by series, and a variation of 0.956-1.030 by h/B sets. The fact that the discussers' results in Fig. 12 largely agree with those of the writers, indicates that no gross errors were introduced by their use of Preston's original calibration. A more detailed examination of boundary shear stress distribution is now being conducted in a wind tunnel and Patel's calibration for the Preston tube has been used in this study and will be used in subsequent studies.

The difficulty in selecting an appropriate bed datum for rippled beds is well-known, and details of the writers' method are given in their earlier paper (13). The anomaly referred to in Figs. 4 and 5 arises because of the poor results for Experiment 16. Because the hydraulic resistance of the channel did change appreciably as the roughness spacing was decreased from one series to the next, only every other depth run was carried out for odd numbered series. The even numbered series are therefore more indicative of trends. The general level of scatter in the shear stress results is not very satisfactory and further work is required. A detailed study of momentum transfer in asymmetrical sections with varying boundary roughness is currently in progress at the University of Birmingham.

APPENDIX.—REFERENCES

 Gessner, F. B., and Jones, J. B., "On some Aspects of Fully Developed Turbulent Flow in Rectangular Channels," *Journal of Fluid Mechanics*, Vol. 23, Part 4, 1965, pp. 689-713.

 Melling, A., and Whitelaw, J. H., "Turbulent flow in a Rectangular Duct," Journal of Fluid Mechanics, Vol. 78, Part 2, 1976, pp. 289-315.

Errata.—The following corrections should be made to the original paper:

Page 1168, Table 1, Col. 1, Experiment 04, Col. 7: Should read 0.198 instead of 0.178

Col. 1, Experiment 23, Col. 3: Should read 9.5 instead of 7.5

Col. 1, Experiment 32, Col. 13: Should read 131 instead of 181

Col. 1, Experiment 86, Col. 13: Should read 66.2 instead of 6.2

Col. 1, Experiment 107, Col. 11: Should read 3.83 instead of 2.83

SECONDARY FLOW AND SHEAR STRESS AT RIVER BENDS^a Closure by James C. Bathurst,⁵ Colin R. Thorne,⁶ and Richard D. Hey⁷

The writers thank Götz for his interesting comments and for the opportunity to clarify several points. However, as Götz does not elaborate on the content of the references on which his comments are based, it is uncertain how they support his conclusions. Presumably the writers' measurements and those of Götz show different flow characteristics, possibly because the writers' measurements were made in rivers while Götz's were apparently made in a laboratory flume. The writers' do not agree that this difference invalidates their conclusions regarding: (1) A relationship between some discharge-related term such as Revnolds number and shear stress uniformity and the relative strengths of the primary and secondary flows: (2) the occurrence of the greatest effect (in relative but not absolute terms) of secondary circulation at medium discharge; and (3) the dependency of shear stress peak magnitudes and positions on secondary currents. These conclusions, which are fully explained in the paper, do not seem to be refuted by any evidence in the discusser's paper and in fact are supported by data from a number of recent fluvial studies (6,14,55), most notably the full results of the work on the River South Esk in Scotland by J. S. Bridge and J. Jarvis (8, 9, and personal communication, 1980). The writers did not intend to imply that the secondary flow patterns which they measured are constant or steady. Firstly, at a given section the strength of the circulation (particularly that of the outer bank cell) fluctuates according to the surging produced by the passage of eddies. At the writers' sites this surging had a period of 5 sec-10 sec but, as measurements were made for a period of 1 min, the recorded patterns are averages for the sections. Secondly, around the bend the pattern varies with, among other factors: (1) Cross-sectional shape; (2) outer bank steepness the more likely reason for the difference between Figs. 2(b) and 2(d) noted

^aOctober, 1979, by James C. Bathurst, Colin R. Thorne, and Richard D. Hey (Proc. Paper 14906).

⁵Sr. Scientific Officer, Inst. of Hydrology, Wallingford, United Kingdom.

Sr. Research Assoc., School of Environmental Sci., Univ. of East Anglia, Norwich NR4 7TJ, United Kingdom.

⁷Lect., School of Environmental Sci., Univ. of East Anglia, Norwich NR4, 7TJ, United Kingdom.

by Götz]; and (3) position along the channel [producing the differences noted between Figs. 3(a) and 3(b)]. The considerable changes in pattern around a bend and the variations with discharge are described in greater detail elsewhere (14, 35, 55, 56 and 57). On the question of how well the results represent



FIG. 12.—Photograph of Electromagnetic Flowmeter, Wading Rod and Supporting Equipment

bend flow, the writers are uncertain what is meant by this. Natural rivers are so full of irregularities and there are so many different flow processes operating that, obviously, the precise pattern and scale of the circulation will differ from bend to bend. In general, though, the writers' measurements are consistent

with others made at river bends of moderate curvature (e.g., 8, 9, 14, 35, and J. S. Bridge and J. Jarvis, personal communication, 1980).

Concerning field techniques, it is agreed that field measurements are difficult to perform accurately but, as secondary velocities in rivers are higher than those in laboratory flumes, the measuring instrument does not need to be as sensitive. Obviously the electromagnetic flowmeter is too big to be used in flumes or close to channel boundaries because of the resulting flow distortion. However, it is negligibly small compared with a river cross section and its discoid shape (Fig. 12) is designed specifically to minimize distortion effects. Further, as it is a rugged instrument, it has a considerable advantage over the hot film anemometer. In general, agreement between the patterns measured by the electromagnetic flowmeter and the patterns indicated by the Ott C-31 current meter, movement of tracer material, lines of vortices, and areas of upwelling was very good.

For the measurements the meter was mounted on a specially constructed wading rod with a sight and steering arms (Fig. 12) so that it was about 0.3 m (0.98 ft) in front of the rod. A rope (with tape measure) was set across the section, perpendicular to the outer bank, and this was used as the reference for longstream and cross-stream directions. [Note that the primary and secondary flow directions and velocities were obtained subsequently by a mathematical technique (4,56)]. At each vertical along the rope the sight was fixed on the same point on the horizon so that the several measurements at the vertical had the same direction datum. There was little difficulty in holding the rod steady except at high flows when buffeting from eddies caused some movement. However, as secondary velocities are higher at high flows, the percentage errors in velocity measurement would not have increased in the same proportion as the absolute errors. It was not expected that the boat or operator would significantly distort the flow around the flowmeter since the meter was held well in front of the operator.

Contrary to Götz's implication the writers did not attempt to use the Ott C-31 current meter at a height of 0.01 m (0.033 ft) above the bed. The distance of 0.01 m was in fact the smallest vertical interval between successive measurements at a vertical. The point nearest to the bed at which the meter could be used was 0.08 m (0.26 ft). Velocities closer to the bed were obtained either by an Ott C-1 current meter (as near to the bed as 0.025 m or 0.082 ft) or else, as described, by extrapolation.

APPENDIX. - REFERENCES

 Bathurst, J. C., "Distribution of Boundary Shear Stress in Rivers," Adjustments of the Fluvial System, D. D. Rhodes and G. P. Williams, eds., Kendall/Hunt Publishing Co., Dubuque, Iowa, 1979, pp. 95-116.

 Thorne, C. R., Bathurst, J. C., and Hey, R. D., "Direktmessungen der Sekundärströmungen in Flussmäandern" (Direct Measurements of Secondary Currents at River

Meanders), Wasser Wirtschaft, in press.

 Thorne, C. R. and Hey, R. D., "Direct Measurements of Secondary Currents at a River Inflexion Point," Nature, Vol. 280, No. 5719, July, 1979, pp. 226-228. Page 1280, paragraph 3, line 7: Should read "within 10 mm/s (0.033 fps)" instead of "within 10 mm/s (0.33 fps)"

Page 1285, paragraph 2, line 8: Should read "i.e., $|(\bar{U}/\bar{u}_*) - (\bar{u}/\bar{u}_*)|/(\bar{U}/\bar{u}_*)$," instead of "i.e., $|(\bar{u}/\bar{u}_*) - (\bar{u}/\bar{u}_*)|/(\bar{U}/\bar{u}_*)$,"

Page 1288, Fig. 8, caption: Should read (Gaged with a Rising Stage) (1 m = 3.28 ft) instead of [Gaged with a Rising Stage (1 m = 3.28 ft)]

Page 1289, Table 2, Col. 11 heading: Should read " $\bar{U}/(gR)^{1/2}$ " instead of " $\bar{u}/(gR)^{1/2}$ "

Page 1290, paragraph 2, line 13: Should read "(Figs. 5, 6, and 7)." instead of "(Figs. 1, 5, and 7)."

Page 1294, Ref. 8: Should read "pp. 303-336." instead of "pp. 203-336."

Page 1295, Ref. 37: Should read "May, 1876," instead of "May 1976,"

Page 1295, Ref. 38: Should read "United Kingdom, in 1978," instead of "United Kingdom,"

INCEPTION OF SEDIMENT TRANSPORT^a Closure by M. Selim Yalin⁵ and Emin Karahan,⁶ Members, ASCE

The writers would like to thank Posey and Narayanan for their comments and complimentary information.

With regard to the comment of Posey, they would like to point out that the purpose of the schematical Fig. 3(b) is merely to show that the flow structure in the lower part of the viscous sublayer is the same as that of a laminar flow (having the same values of the characteristic parameters at the bed). Fig. 3(b) is not intended to throw any light on the particle-lift mechanism. On the other hand the "deliberate vagueness" of the upper boundary of the viscous sublayer in Fig. 3(b) should be sufficient to indicate that the writers do not exclude the possibility of the penetration of turbulent fluctuations into the viscous sublayer.

In the writers' view the schematical analysis presented by Narayanan is attractive and informative. The writers have some reasons to believe that with the further decrement of X_{cr} the common part of the initiation curve (on the left of Fig. 5) should tend to become parallel to the X_{cr} -axis. This belief appears to be in agreement with the analysis of Narayanan.

The writers do not think that the transition zone "is prone to scatter" due to the differences in h/D, as the available data for laminar and hydraulically smooth turbulent flows from the same pattern. The divergence between "laminar"

^a November, 1979, by M. Selim Yalin and Emin Karahan (Proc. Paper 14975).

⁵ Prof., Dept. of Civ. Engrg., Ellis Hall, Queen's Univ., Kingston K7L 3N6, Canada. ⁶ Asst. Prof., Dept. of Civ. Engrg., Technical Univ., Istanbul, Turkey; formerly, Post-Doctoral Fellow, Queen's Univ., Kingston, Ontario, Canada.

and "turbulent" initiation curves in Fig. 5 takes place due to the change in the regime of a turbulent flow (characterized by $X_{cr} \sim D \sim k_s$) and not due to the conversion of a laminar flow into a hydraulically smooth) turbulent one (characterized by $R \sim h$).

STAGED MULTIPORT DIFFUSERS*

Closure by Charles W. Almquist, A. M. ASCE, and Keith D. Stolzenbach, M. ASCE

Brocard has made a useful addition to the theory presented in the original paper; data from the Jamestown Nuclear Power Station study presented in his Fig. 11 show good agreement with his proposed extension. The writers would like to comment briefly on certain aspects of this extension, and to indicate an alternative approach which may be applicable when assumptions in the proposed extension break down.

In including the cross-flow entrainment directly into the continuity equation for the staged diffuser induced flow, two assumptions have been made; these are that the cross-flow entrainment is directly proportional to the cross-flow velocity, and that the concept of the staged diffuser as a continuous line source of momentum remains valid in the presence of a cross-flow. The former assumption has been used with success in the calculation of other jet-type flows (23), although the coefficient of proportionality must, in general, be determined experimentally and does not have a universal value. For the case of a staged diffuser, the value of $\alpha_c = 1.0$ proposed by Brocard appears to be dictated by a total flow constraint (see next paragraph) and is not always represented of a local dynamic condition as implied in Brocard's differential entrainment relationship (Eq. 29).

The analytical description of the staged diffuser as a continuous line source of momentum is justified in a quiescent ambient by the empirical observation that the individual jets of a typical design interact quite strongly, leading in fact to an inhibited rate of growth of the diffuser plume along the diffuser axis. Even for relatively large jet spacings, the interaction is strong enough that the line source assumption still holds. In the presence of a relatively weak cross-flow, and so long as the jets are not spaced too far apart, the individual jets may be expected to continue to interact quite strongly, and the momentum line source concept can be expected to remain approximately correct. In this

^aFebruary, 1980, by Charles W. Almquist and Keith D. Stolzenbach (Proc. Paper 15185). ³Grad. Research Asst., Dept. of Civ. Engrg., Coll. of Engrg., Environmental Health and Water Resources Engrg., Ernest Cockrell, Jr. Hall, 8.600, Univ. of Texas at Austin, Austin, Texas 78712.

⁴Assoc. Prof., Dept. of Civ. Engrg., Massachusetts Inst. of Tech., Cambridge, Mass.

situation, complete entrainment of that portion of the crossflow which passes directly over the diffuser would be consistent with the line source nature of the diffuser. This is equivalent to $\alpha_c=1.0$, as Brocard assumes in his proposed formulation.

However, in the presence of a stronger cross-flow, of if the jet spacing is relatively large, the individual jets may be deflected enough to prevent interaction, each individual jet then behaving much as a free jet in a cross-flow. In this case, the concept of the staged diffuser as a line source of momentum can no longer be expected to hold, and analysis of the individual jets would be more appropriate. This is essentially the approach adopted by Adams and Trowbridge (24) and Trowbridge (25) in a detailed investigation of the near-field flow of staged diffusers.

Our conclusion is that, in the presence of a cross-flow, staged diffuser performance will fall between two extremes: complete interception of the cross-flow, valid for weak cross-flows when the line source concept remains valid, and breakdown of the line source concept in the presence of a stronger cross-flow, in which case an individual jet analysis is appropriate. Which approach

is the more applicable must be determined on a case-by-case basis.

The writers would also like to point out that Adams and Trowbridge (24), and Trowbridge (25) have presented comprehensive analyses of the near-field of the staged diffuser, including analytical descriptions of the entrainment flow-field in both Eulerian and Lagrangian coordinates, and an extension of the theory to include sloping bottoms. The Lagrangian analyses form a useful basis for evaluating the impact of a staged diffuser discharge on receiving water biota; the general approach reported therein may also be applied to other types of buoyant discharges. The interested reader is referred to their reports.

APPENDIX.—REFERENCES

 Chan, D. T.-L., Lin, J.-T. and Kennedy, J. F., "Entrainment and Drag Forces of Deflected Jets," *Journal of the Hydraulics Division, ASCE*, Vol. 102, No. HY5, Proc. Paper 12141, May, 1976, pp. 615-635.

 Adams, E. E., and Trowbridge, J. H., "Near Field Performance of Staged Diffusers in Shallow Water," Energy Laboratory Report No. MIT-EL-79-015, Massachusetts

Institute of Technology, Cambridge, Mass., Apr., 1979.

25. Trowbridge, J. H., "Near Field Performance of Staged Diffusers," thesis presented to Massachusetts Institute of Technology, at Cambridge, Mass., in 1979, in partial fulfillment of the requirements for the degree of Master of Science.

TIME-DEPENDENT STOCHASTIC MODEL OF FLOODS a

The following corrections should be made to the original paper:

Page 653, Eq. 28, right side: Should read

$$\left[\prod_{i=1}^{n} \lambda_{\rho}(t_{i}) \lambda_{c}(t_{i})\right] \exp \left[-\int_{0}^{t_{f}} \lambda_{\rho}(t) dt - \sum_{i=1}^{n} \lambda_{c}(t_{i}) y_{i}\right]$$

instead of

$$\left[\prod_{i=1}^{n} \lambda_{p}(t_{i}) \lambda_{c}(t_{i})\right] \exp \left[-\int_{0}^{t_{f}} \lambda_{p}(t) dt\right] - \sum_{i=1}^{n} \lambda_{c}(t_{i}) y_{i}$$

Page 663, Ref. 5, line 3: Should read "New York, N.Y., 1972," instead of "New York, N.Y., 1072,"

Log Pearson Type 3 Distribution: Method of Mixed Moments^b

The following corrections should be made to the original paper:

Page 1000, paragraph 4, line 1: Should read "and $c \le y < + \infty$." instead of "and $c \le y > + \infty$."

Page 1016, Table 8, heading of Col. 7: Should read " $\gamma_{y(2)}$ " instead of " $\gamma_{x(2)}$ " Page 1017, paragraph 1, line 4: Should read "By virtue of" instead of "By virtue of"

Page 1018, line 1: Should read "selection of γ_x on the basis of \bar{Y} ," instead of "selection γ_x on the basis of \bar{Y} ,"

^{*}May, 1980, by Michel North (Proc. Paper 15405).

^bJune, 1980, by Donthamsetti Veerabhadra Rao (Proc. Paper 15477).

EMPIRICAL INVESTIGATION OF CURVE NUMBER TECHNIQUE a Discussion by Michael Daly, M. ASCE

The writer wishes to thank the author for a most informative presentation. The author speculates that the reason for the poor fit at the Sonoita Creek watershed is that the curve number (CN) technique is inappropriate in the arid west. The writer wishes to concur in this speculation as it has been his experience that the CN technique provides excessive runoff for large rainfall events.

An alternate technique developed by the United States Geological Survey (USGS) has been employed by the writer which has been found to provide very good data (8). This technique uses multiple-regression analysis relating flood peaks of 5-yr, 10-yr, 25-yr, and 50-yr recurrence intervals to selected physical and climatic basin characteristics. The method is based on data for 163 sites where flood records have been obtained for 8 yr or more, and on the maximum known floods at 439 sites. Using this technique, an estimate of the natural-peak flow can be obtained for any desired site within New Mexico by using the basin characteristics at the desired site. Copies of the report detailing this technique are available from the USGS at the address given in Ref. 8. The USGS final report will be available in the summer of 1981. It is being prepared by R. P. Thomas.

APPENDIX.—REFERENCE

 Scott, A. G., "Preliminary Flood-Frequency Relations and Summary of Maximum Discharges in New Mexico—A Progress Report," Open File Report, U.S. Geological Survey, Water Resources Division, Room 115, Federal Building, Santa Fe, N.M. 87501.

Discussion by Kenneth G. Renard,3 M. ASCE

The author is to be commended for his effort to present a method for illustrating how runoff frequency relationships can be developed from a frequency relationship for precipitation.

It would be interesting if the author had commented regarding whether the curve numbers he used to develop the information in Figs. 1-5 agreed with values suggested in the National Engineering Handbook of the Soil Conservation

^{*}September, 1980, by Allen T. Hjelmfelt, Jr. (Proc. Paper 15693).

²Pres., San Juan Engrg., Inc., P.O. Box 752, Farmington, N.M. 87401.

³Research Hydr. Engr., Southwest Rangeland Watershed Research Center, United States Dept. of Agric., Science and Education Administration, Agricultural Research, 442 East Seventh St., Tucson, Ariz. 85705.

Service (SCS) (3). Similarly, it would be helpful to note which of the antecedent moisture levels was used, as suggested in the handbook. Because the handbook suggests that the curve number changes with varying antecedent moisture, it seems likely that the curve number associated with the author's frequency analysis would change in response to the exceedence probability. Thus, one might expect the curve number for high probability would be lower than it would be for low probability.

That the results of the technique are poor for Sonoita Creek, near Patagonia, Ariz., is certainly not surprising to a hydrologist familiar with the hydrologic and physiographic characteristics controlling the rainfall-runoff process in the region. The spatial distribution of precipitation and the resulting partial area

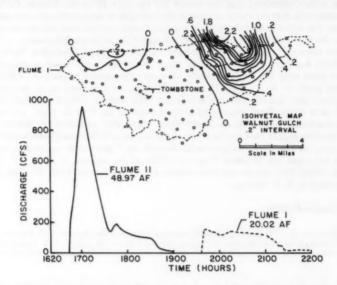


FIG. 6.—Storm near Upper End of Walnut Gulch on July 30, 1966; Each Circle Shows Location of Raingage on 57.7-sq mile area

runoff, along with the reductions in the flow volume (transmission losses) as runoff moves from the source area over the normally dry alluvial streambeds, dominate the hydrologic response of many semiarid watersheds to individual precipitation events.

To illustrate these phenomena, two runoff events on the Walnut Gulch Experimental watershed near Tombstone, Ariz. are used. The watershed is a 57.7-sq mile (150-km²) tributary of the San Pedro River about 75 mile from Sonoita Creek. Mean annual precipitation is about 14 in. (350 mm), which is slightly less than that at Sonoita Creek. The hydrologic phenomena, however, are very similar in both watersheds.

Fig. 6 represents a precipitation event concentrated in the upper portion of

the watershed. Precipitation was not recorded for this event at the raingage in Tombstone. Much of the runoff was lost by transmission losses in the channel before reaching the watershed outlet at Flume 1. Such an event shows a typical air-mass thunderstorm's limited areal extent. Runoff measured at the outlet of a small 3.18-sq mile (8.24-km²) subwatershed of Walnut Gulch was appreciable. By the time this flow had traversed nearly 11.4 mile (18.3 km) of normally dry streambed, the flow was significantly less.

Fig. 7 shows what can happen if the storm is located nearer the watershed outlet. For this storm, the opportunity for transmission losses to reduce the

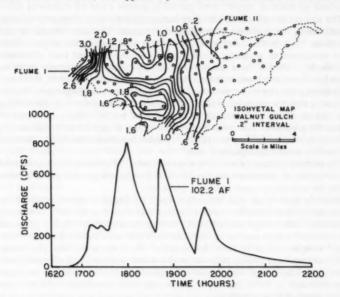


FIG. 7.—Storm of August 25, 1968 Was Concentrated in Lower Portion of Watershed; Multipeaked Hydrograph Resulted from Runoff in Various Tributaries and from Longer Duration Hyetograph with Several Periods of Precipitation Excess

streamflow are much less, and in fact, runoff from different tributaries results in a multipeaked hydrograph. If the storm timing was such that all peaks arrived at the same time, the flood peak would have been significantly larger.

In summary, it should be apparent that no single precipitation gage will provide an adequate representation of the input to the watershed for a single runoff event. Thus, the frequency relationship between individual precipitation events and corresponding runoff is nonexistent in ephemeral streams in southwestern United States. Given that the raingages at Tombstone were used for these two events, it would not have recorded the storm shown in Fig. 6, and would have seriously underestimated the precipitation producing the runoff in Fig. 7.

CALIBRATION OF BED-LOAD SAMPLERS^a Discussion by Glendon T. Stevens, Jr., M. ASCE

The authors of this article are to be commended for their display of courage in addressing the mysteries of bed-load movements. The same should be said for those who, in the past, have probed the recesses of this enigma. They have developed an intriguing assortment of samplers and bed load movement relationships. Most of these samplers and corresponding bed movement relationships have been developed with the aid of small-scale physical models. However, after having spent extended periods of time at the Waterways Experiment Station observing and discussing moveable bed models, it is the writer's understanding that due to distortion in scaling of this type of model, volume of transport cannot be predicted. This point is made, however, in light of an understanding that this type of model may be utilized to predict movement trends, i.e., location of possible scour and deposition sites.

The primary purpose of this review is two-fold: (1) To inform those concerned of the existence of voluminous quantities of prototype data; and (2) to humbly probe for answers to some resurgent questions.

Over the past 10 yr, this writer has been privileged to spend hundreds of hours on the Mississippi River collecting data and observing the flow phenomena associated with a large alluvial river. During this period this writer collected and analyzed a large number of bed samples which were collected with a "grab type" sampler. In addition, with the aid of the latest electronic positioning equipment and a recording pathometer this writer collected and observed both lateral and longitudinal bed profiles. Longitudinal profiles 1,000 ft in length were collected in 100-ft increments across the river at various locations over a wide range of flow conditions.

Analysis of this data reveals that the river bed, at least from the standpoint of bed forms, does not display the same activity throughout a lateral section. Observation reveals that the height, length, and location of bed activity changes under constant flow conditions. In other words, a set of data might reveal a segment of the section that sustains sand waves with the remainder of the section relatively smooth. One day later the segment that sustained the sand waves might be smooth with bed activity in another segment of the section. In some cases the bed forms appear laterally yet in others they appear to be longitudinal.

Grab bed samples collected twice daily at the same point in a cross section when analyzed show a marked change in D_{50} . Vertical velocity profile data collected simultaneously 5 ft apart when analyzed will produce different coeffi-

^{*}October, 1980, by Peter Engel and Y. Lam Lau (Proc. Paper 15725).

³ Assoc. Prof. of Civ. Engrg., 302 Engrg. Research Lab., Univ. of Missouri-Rolla, Rolla, Mo. 65401.

cients and exponents for a vertical velocity equation.

And thus, it is that this writer has read published materials dealing with sampling, calculating, and predicting sediment transport with highly mixed emotions which include interest, chagrin, and wonderment. It appears that each new publication sets upon a foundation of fallacies attributable to earlier authors. Then, the most recent author tries valiantly to vindicate the historical fallacies via implementation of physical model data or mathematical theory. Such procedure is highly transparent and equally shocking to the practicing engineer who strives to use "up-to-date" techniques. And each time the practicing engineer is subjected to this procedure he has a feeling of having been "bitten to death by ducks," since it seems to be a persistent approach utilized by authors today.

Questions exist on this subject, which, if answered, would clarify an otherwise nebulous perspective in regard to the collection and calculation of sediment

transport.

First of all, what is the clear-cut definition of bed load? Some authors define it as "that portion of the sediment load which moves in contact with the river bed and possesses a thickness of two-grain diameters." If we are to subscribe to this definition, then we have to be concerned about the obvious fact that the opening in the basket and sack type samplers appears to be too large!

Secondly, where does the sampler collect samples? As indicated previously, the entire cross section does not appear to be active. There should be places in the nonactive zone where bed movement is impending. The presence of a sampler in this zone would cause enough turbulence to create motion; thus, a sample would be collected which would not be representative of the true bed movement.

Next, how is a sample analyzed? Basket and sack type samplers are fashioned like sieves. Therefore, the minimum-sized particle collected is determined by the size of the openings in the sampler and the result is that the sample collected is not representative of the material transported.

Another question involves the calculation of bed load; how is this done? (Assuming the correct sample has been collected from the proper points within the given cross section.) Additionally, what happens when a large sand wave (five feet high or greater) passes over a bed load sampler? Also, it is necessary to ask whether or not bed load movement has a constant, uniform depth.

And, finally, two further questions remain unanswered which are worthy of consideration: (1) Are total bed load calculations based on the assumption that the total depth of bed load has passed through the sampler; and (b) how is suspended sediment kept from entering the sampler as it traverses through the water?

Surely these questions are pertinent. If not answerable, then they would tend to denigrate the worth of any article addressing the subject and relegate it to the category of semantic jousting.

SEDIMENTATION IN IRON GATES RESERVOIR ON THE DANUBE Discussion by Nani G. Bhowmik²

The author must be congratulated for presenting such a thorough review of the sedimentation problems associated with a large reservoir. The size of the reservoir, its drainage basin, and other characteristics make it immensely important to the well-being of the surrounding countries.

The author has systematically presented some valuable data as to the suspended sediment load, its size distribution, and the deposition of the suspended and bed loads in the reservoir.

The author has made a computation as to the rate of erosion from the catchment based on the total sediment load carried by the river. This was shown to be 3 mm from the entire catchment corresponding to the yearly sediment load of 32,200,000 tons in the river. The writer believes that the assumption of 32.2 × 10⁶ tons of sediment load carried yearly by river is the only sediment that is eroded from the catchment is in error. Some of the sediment eroded from the catchment does not necessarily reach the main stream. Research conducted at the Illinois State Water Survey by Stall and Lee (4) has shown that the range of sediment delivery ratios can be anywhere from 20%–50% for the watersheds of the State of Illinois. This means that only 20%–50% of the sediment eroded from the catchment finally reaches the stream. Therefore, the total weight of the eroded sediment from the Danube catchment must be higher than the measured sediment load of 32.2 × 10⁶ tons. It would be interesting to find out the range of probable sediment delivery ratios for the Danube.

The author has extrapolated the relationship between river discharge Q and sediment load Q_1 to estimate the sediment load Q_1 of the Danube of the 133-yr period of record. The writer is wondering about the validity of this relationship without any constraints. Research conducted at the Illinois State Water Survey by Bhowmik, et al. (3) has shown that this type of extrapolation must be done with caution. The range of values of sediment load Q_1 for the same river discharge Q can vary by few hundred percent. This is shown for the Wilmington gaging station on the Kankakee River in Illinois in Fig. 6. Data shown here are from a 12-month period. The confidence intervals of the fitted line are also shown in Fig. 6. The catchment area for the station is 1.3×10^4 km². Similar variabilities were also observed for other stations. The writer is very much interested to find out about the variabilities observed by the author in his $Q_1 = Q^{2.72}/102$ relationship.

The suspended sediment load analyses shown in Table 5 are also very interesting. It appears that most of the suspended sediment load from November-December,

^{*}October, 1980, by Vlad Focsa (Proc. Paper 15782).

² Principal Scientist, Illinois State Water Survey, P.O. Box 5050, Station A, Champaign, Ill. 61820.

1958 at Orsova consisted of silt, clay or fine sand. Data collected from the Kankakee River by Bhowmik, et al. (3) indicated that for some stations, during flood flows, 60%-80% of the suspended load was sand and the remaining portion was silt and clay. However, during low flows the river almost exclusively carried silt and clay as suspended load. The writer would like to request the author

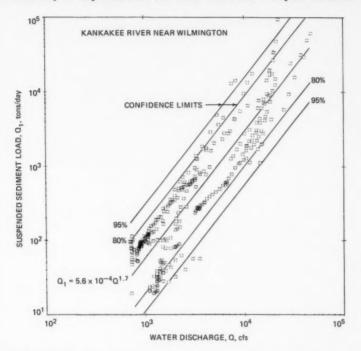


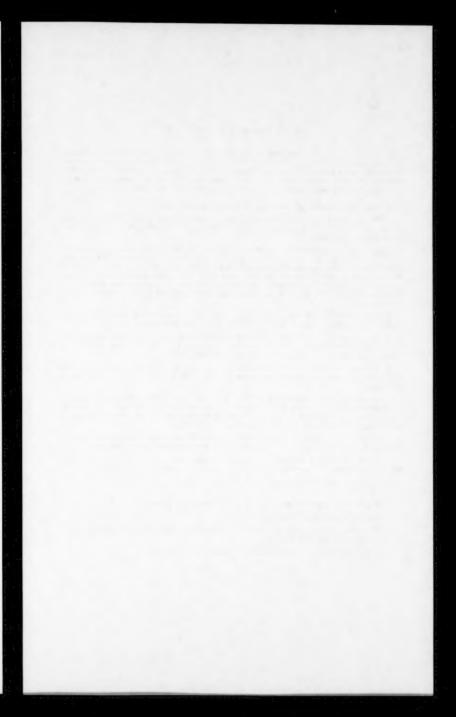
FIG. 6.—Relationship between Suspended Sediment Load and Water Discharge for Kankakee River near Wilmington

to discuss whether or not such variability was observed for the Danube at Orsova or other places.

APPENDIX.-REFERENCES

 Bhowmik, N. G., Bonini, A. P., Bogner, W. C., and Byrne, R. P., "Hydraulics of Flow and Sediment Transport in the Kankakee River in Illinois," *Illinois State Water Survey Report of Investigation 98*, Urbana, Ill., 1980.

 Stall, J. B., and Lee, M. T., "Reservoir Sedimentation and Its Causes in Illinois," Water Resources Bulletin, Vol. 16, No. 5, Oct., 1980.



TECHNICAL PAPERS

Original papers should be submitted in triplicate to the Manager of Technical and Professional Publications, ASCE, 345 East 47th Street, New York, N.Y. 10017. Authors must indicate the Technical Division or Council, Technical Committee, Subcommittee, and Task Committee (if any) to which the paper should be referred. Those who are planning to submit material will expedite the review and publication procedures by complying with the following basic requirements:

- 1. Titles must have a length not exceeding 50 characters and spaces.
- The manuscript (an original ribbon copy and two duplicate copies) should be double-spaced on one side of 8-1/2-in. (220-mm) by 11-in. (280-mm) paper. Three copies of all figures and tables must be included.
- 3. Generally, the maximum length of a paper is 10,000 word-equivalents. As an approximation, each full manuscript page of text, tables or figures is the equivalent of 300 words. If a particular subject cannot be adequately presented within the 10,000-word limit, the paper should be accompanied by a rationale for the overlength. This will permit rapid review and approval by the Division or Council Publications and Executive Committees and the Society's Committee on Publications. Valuable contributions to the Society's publications are not intended to be discouraged by this procedure.
- 4. The author's full name, Society membership grade, and a footnote stating present employment must appear on the first page of the paper. Authors need not be Society members.
- 5. All mathematics must be typewritten and special symbols must be identified properly. The letter symbols used should be defined where they first appear, in figures, tables, or text, and arranged alphabetically in an appendix at the end of the paper titled Appendix.—Notation.
- Standard definitions and symbols should be used. Reference should be made to the lists
 published by the American National Standards Institute and to the Authors' Guide to the Publications
 of ASCE.
- 7. Figures should be drawn in black ink, at a size that, with a 50% reduction, would have a published width in the Journals of from 3 in. (76 mm) to 4-1/2 in. (110 mm). The lettering must be legible at the reduced size. Photographs should be submitted as glossy prints. Explanations and descriptions must be placed in text rather than within the figure.
- 8. Tables should be typed (an original ribbon copy and two duplicates) on one side of 8-1/2-in. (220-mm) by 11-in. (280-mm) paper. An explanation of each table must appear in the text.
- 9. References cited in text should be arranged in alphabetical order in an appendix at the end of the paper, or preceding the Appendix.—Notation, as an Appendix.—References.
- 10. A list of key words and an information retrieval abstract of 175 words should be provided with each paper.
 - 11. A summary of approximately 40 words must accompany the paper.
 - 12. A set of conclusions must end the paper.
- 13. Dual units, i.e., U.S. Customary followed by SI (International System) units in parentheses, should be used throughout the paper.
 - 14. A practical applications section should be included also, if appropriate.

